

## Deconvoluting Microstructural Features in Unidirectional Composites

Gomarasca, S.

**DOI**

[10.4233/uuid:47e95062-4d68-4162-a33e-3a7083ca23d5](https://doi.org/10.4233/uuid:47e95062-4d68-4162-a33e-3a7083ca23d5)

**Publication date**

2025

**Document Version**

Final published version

**Citation (APA)**

Gomarasca, S. (2025). *Deconvoluting Microstructural Features in Unidirectional Composites*. [Dissertation (TU Delft), Delft University of Technology]. <https://doi.org/10.4233/uuid:47e95062-4d68-4162-a33e-3a7083ca23d5>

**Important note**

To cite this publication, please use the final published version (if applicable).  
Please check the document version above.

**Copyright**

Other than for strictly personal use, it is not permitted to download, forward or distribute the text or part of it, without the consent of the author(s) and/or copyright holder(s), unless the work is under an open content license such as Creative Commons.

**Takedown policy**

Please contact us and provide details if you believe this document breaches copyrights.  
We will remove access to the work immediately and investigate your claim.



Silvia Gomasasca

**Deconvoluting  
Microstructural Features in  
Unidirectional Composites**



# **DECONVOLUTING MICROSTRUCTURAL FEATURES IN UNIDIRECTIONAL COMPOSITES**



# **DECONVOLUTING MICROSTRUCTURAL FEATURES IN UNIDIRECTIONAL COMPOSITES**

## **Proefschrift**

for the purpose of attaining the degree of doctor  
at Delft University of Technology,  
by the authority of Rector Magnificus prof. dr. ir. T.H.J.J. van der Hagen,  
chair of the Board for Doctorates,  
to be defended publicly on  
Wednesday 10 September 2025 at 12:30

by

**Silvia GOMARASCA**

Master of Science in Aerospace Engineering,  
Delft University of Technology, the Netherlands,  
born in Vittorio Veneto, Italy

This dissertation has been approved by the promotor.

Composition of the doctoral committee:

Rector Magnificus	chairperson
Prof. C.A. Dransfeld	Delft University of Technology, <i>promotor</i>
Dr. ir. D.M.J. Peeters	Delft University of Technology, <i>copromotor</i>
Dr. ir. B. Atli-Veltin	Delft University of Technology, <i>copromotor</i>

Independent members:

Prof. Dr. ir. J.L. Herder	Delft University of Technology
Dr. S. Pimenta	Imperial College London
Prof. Dr. ing. P. Middendorf	University of Stuttgart
Prof. Dr. ir. R. Akkerman	University of Twente
Prof. Dr. V. Garbin	Delft University of Technology, <i>reserve member</i>



<i>Keywords:</i>	Unidirectional Composites, Prepreg Tapes, Microstructure, X-Ray Computed Tomography
<i>Printed by:</i>	Ipskamp   <a href="https://www.ipskampprinting.nl/">https://www.ipskampprinting.nl/</a>
<i>Cover by:</i>	Kamila Waszkowiak
<i>Style:</i>	TU Delft House Style, with modifications by Moritz Beller <a href="https://github.com/Inventitech/phd-thesis-template">https://github.com/Inventitech/phd-thesis-template</a>

Copyright © 2025 by Silvia Gomasasca

ISBN 978-94-6518-095-3

An electronic version of this dissertation is available at <http://repository.tudelft.nl/>.

*To my family and loved ones.*

Silvia Gomasasca



# CONTENTS

<b>Summary</b>	<b>xi</b>
<b>Samenvatting</b>	<b>xiii</b>
<b>Riepilogo</b>	<b>xvii</b>
<b>1 Introduction</b>	<b>1</b>
1.1 The role of unidirectional composites in advanced engineering. . . . .	2
1.2 Characterisation of three-dimensional variability in unidirectional composite microstructures . . . . .	3
1.3 Complex structural organization in nature . . . . .	4
1.4 Research gaps . . . . .	5
1.5 Objectives and scope . . . . .	5
1.6 Thesis outline . . . . .	6
<b>2 Characterising microstructural organisation in unidirectional composites</b>	<b>9</b>
2.1 Introduction . . . . .	10
2.2 Methodology. . . . .	12
2.2.1 Sample preparation. . . . .	12
2.2.2 Tomographic image collection . . . . .	12
2.2.3 Fibre path reconstruction. . . . .	13
2.3 Microstructural descriptors. . . . .	14
2.3.1 Differential tortuosity . . . . .	14
2.3.2 Collective motion . . . . .	15
2.3.3 Length of neighbourhood . . . . .	16
2.4 Results . . . . .	17
2.4.1 Differential tortuosity . . . . .	17
2.4.2 Collective motion . . . . .	19
2.4.3 Length of neighbourhood . . . . .	20
2.5 Discussion . . . . .	22
2.5.1 Differential tortuosity . . . . .	22
2.5.2 Collective motion . . . . .	22
2.5.3 Length of neighbourhood . . . . .	22
2.5.4 Interrelation of parameters. . . . .	24
2.6 Conclusion. . . . .	25

<b>3</b>	<b>Characterising pore networks and their interrelation with the fibre architecture in unidirectional composites</b>	<b>27</b>
3.1	Introduction . . . . .	28
3.2	Methodology. . . . .	29
3.2.1	Material . . . . .	29
3.2.2	Tomographic image collection . . . . .	29
3.2.3	Segmentation of features of interest . . . . .	29
3.2.3.1	Internal and surface porosity . . . . .	30
3.2.3.2	Fibre path reconstruction . . . . .	32
3.3	Quantification of metrics for the material description . . . . .	33
3.3.1	Description of pore features . . . . .	33
3.3.2	Fibre differential tortuosity. . . . .	33
3.3.3	Data reduction of pore regions and differential tortuosity for feature correlation . . . . .	33
3.3.4	Determination of characteristic lengthscales of differential tortuosity and pore regions . . . . .	35
3.4	Results and discussion . . . . .	35
3.4.1	Porosity . . . . .	35
3.4.1.1	Quantification of cross-sectional pore clustering . . . . .	35
3.4.1.2	Geometrical analysis of internal and surface pores . . . . .	37
3.4.1.3	Implications on tape manufacturing processes . . . . .	38
3.4.2	Differential tortuosity . . . . .	39
3.4.3	Relationship between pore distribution and fibre tortuosity . . . . .	41
3.4.3.1	Correlation of pore distribution and fibre differential tortuosity . . . . .	41
3.4.3.2	Meandering fibres in high-tortuosity regions . . . . .	43
3.4.4	Determination of the lengthscale of propagation for pore network and tortuosity . . . . .	44
3.5	Conclusion. . . . .	47
<b>4</b>	<b>Characterising the variability of unidirectional preregs at multiple observation scales</b>	<b>49</b>
4.1	Introduction . . . . .	50
4.2	Materials and methods . . . . .	51
4.2.1	Sample acquisition . . . . .	51
4.2.2	Microstructural analysis . . . . .	51
4.2.2.1	Structure tensor analysis . . . . .	53
4.2.2.2	Single fibre analysis . . . . .	55
4.3	Results and discussions. . . . .	55
4.3.1	Single fibre tracking . . . . .	55
4.3.2	Structure tensor analysis . . . . .	56
4.4	Conclusion. . . . .	60



<b>5 Conclusion and perspectives</b>	<b>63</b>
5.1 Insights from the work . . . . .	64
5.2 Discussion and short-term perspectives . . . . .	67
5.2.1 Capturing features of interest . . . . .	67
5.2.1.1 Imaging artefacts and segmentation bottlenecks . . . . .	67
5.2.1.2 Fibre path extraction . . . . .	68
5.2.2 Microstructural description and analysis . . . . .	68
5.2.2.1 Describing the fibre microstructural complexity . . . . .	68
5.2.2.2 Pore network analysis . . . . .	69
5.2.2.3 Meandering fibre analysis . . . . .	70
5.2.3 Multiscale analysis . . . . .	70
5.2.4 Process-structure-property relationships . . . . .	71
5.2.4.1 Porosity evolution and interplay with the fibre architecture	72
5.2.4.2 Edge-core effects . . . . .	72
5.2.4.3 Predictive modeling and simulation . . . . .	73
5.3 Long-term perspectives . . . . .	74
<b>A Appendix: Pore fraction across sub-volumes</b>	<b>75</b>
<b>B Appendix: Statistical analysis of internal and surface pore geometry</b>	<b>81</b>
<b>C Appendix: Tortuosity maps across sub-volumes</b>	<b>83</b>
<b>D Appendix: Segmented representation of internal and surface pores</b>	<b>85</b>
<b>E Appendix: Manually tracked meandering fibres</b>	<b>89</b>
<b>F Appendix: Determination of a threshold of high nSD similarity</b>	<b>93</b>
<b>G Appendix: Sensitivity analysis on the kernel size for max-filtering</b>	<b>95</b>
<b>H Appendix: Single-fibre misalignment for all samples</b>	<b>99</b>
<b>I Appendix: Structure-tensor-based misalignment for all samples</b>	<b>101</b>
<b>Bibliography</b>	<b>105</b>
<b>Acknowledgments</b>	<b>119</b>
<b>Curriculum Vitæ</b>	<b>123</b>
<b>List of Publications</b>	<b>125</b>



## SUMMARY

Unidirectional composite tapes are extensively used in automated manufacturing to produce high-performance composite parts with significant design flexibility. Their superior mechanical properties stem from the alignment of continuous fibres in a single direction, making them ideal for advanced engineering applications. However, the performance of these components is closely linked to their microstructure, and accurately predicting their behaviour requires a detailed understanding of their microstructural characteristics.

Theoretical models assume perfect fibre alignment along the longitudinal axis to maximise mechanical efficiency by ensuring effective load transfer. In reality, manufacturing constraints make perfect alignment unachievable. Variations such as fibre waviness, misalignments, and uneven distribution introduce microstructural variability, which affects overall performance and can undermine reliability in critical applications.

For high-performance industries such as aerospace and automotive engineering, simply accommodating manufacturing limitations is insufficient. Instead, a shift towards 'microstructures by design', where microstructural features are deliberately controlled to meet specific performance criteria, would enhance predictive accuracy and material optimisation. Achieving this requires precise microstructural characterisation to better inform manufacturing processes.

A critical step toward this goal is accurately characterising and describing the microstructure of unidirectional tapes to accurately inform manufacturing processes. Recent advancements in imaging technologies, particularly three-dimensional (3D) imaging techniques like X-ray Computed Tomography (XCT), have revolutionised our ability to examine microstructural features at unprecedented detail. XCT provides high-resolution 3D images of the internal structure of composite tapes, enabling researchers to capture essential characteristics such as fibre orientation, distribution, and defects with remarkable precision.

The challenge now lies in translating this wealth of 3D imaging data into actionable insights. To achieve this, there is the need for a comprehensive toolbox of metrics and analytical methods tailored for the microstructural analysis of unidirectional composite tapes. These tools would enable researchers and engineers to quantify the complexity of the microstructure, identify critical defects, and understand their implications on material properties and performance. Additionally, these metrics could serve as benchmarks for manufacturing quality control, guiding process improvements to minimise microstructural variability.

The scope of the thesis is to develop a methodology for the evaluation of complex microstructural features in unidirectional composite tapes at a three-dimensional level, based on information obtained via X-Ray Computed Tomography. In particular, carbon fibre-reinforced tapes with a high-performance thermoplastic matrix have been selected as case study for this work since they constitute a relevant case study for materials used in aerospace applications.

By introducing three novel descriptors inspired by nature – differential tortuosity, collective motion, and length of the neighbourhood – the study provides a comprehensive framework for analysing the complexity of fibre architectures. Differential tortuosity measures fibre path deviations from an ideal trajectory, revealing edge-core gradients where fibres near the edges show greater misalignment. Collective motion quantifies the alignment of fibre groups, showing reduced coherence in edge regions, likely caused by microstructural disruptions. Length of neighbourhood assesses fibre network interconnectivity, which allows for the distinction between regions of higher fibre association from areas of greater fibre entanglement, and to evaluate characteristic lengthscales of fibre association within the material.

The study of fibre architectures was then extended to porosity linked to both internal air regions of the tape and their external complex topology, which is a characteristic feature. The method developed allows to compare spatial distributions at a three-dimensional level, highlighting in the tape analysed a significant correspondence between regions of elevated tortuosity and increased pore fractions. Regions associated with highly tortuous meandering fibres exhibit a pronounced association with porosity located both in the bulk and at the tape surface, suggesting a strong interaction between non-collective fibre displacement and the probability of pore location. Furthermore, our study quantifies the length scale of feature propagation, shedding light on the spatial extent of microstructural pore occurrence within the composite. These findings have significant implications from a characterisation perspective to aid modelling approaches and manufacturing processes for high-performance composite prepregs tapes.

However, to define a representative microstructural fingerprint of a given tape, investigations at the required small voxel size lead to limited volumes of observation, which might not be representative. To ensure representativeness, a multiscale approach was used to extend the findings to higher scales, from microscopic (single fibre) up to mesoscopic (dimension of tape) length scale, to generate further insight into the microstructural organisation of thermoplastic prepreg tapes. By exploring the ability of XCT imaging for carbon fibre-reinforced thermoplastic composites at different voxel sizes, the work aims to identify the limitations of the use of different scales of observations to capture features of microstructures and their propagation from micro- to mesoscale level. While structure tensor analysis appeared to correctly capture misaligned regions in XCT images with small voxel size ( $1/10$  of the fibre diameter), the method proved ineffective for larger voxel size images ( $1/2$  of the fibre diameter).

Overall, this thesis advances the development of methodologies for deconvoluting complex microstructural features in unidirectional composite tapes. The findings are expected to enhance material characterisation, paving the way for improved optimisation of tape manufacturing processes. Ultimately, this work aims to support the tailoring of composite architectures to meet specific performance requirements. These advancements hold significant potential for optimising composite design and driving innovations in high-performance applications.

## SAMENVATTING

Unidirectionele composiet tapes worden veelvuldig gebruikt in geautomatiseerde productie om hoogwaardige composietonderdelen te produceren met aanzienlijke ontwerpflexibiliteit. Hun superieure mechanische eigenschappen komen voort uit de uitlijning van doorlopende vezels in eenzelfde richting, waardoor ze ideaal zijn voor geavanceerde technische toepassingen. De prestaties van deze componenten zijn echter nauw verbonden met hun microstructuur en om hun gedrag nauwkeurig te voorspellen, is een gedetailleerd begrip van hun microstructurele kenmerken vereist.

Theoretische modellen gaan uit van een perfecte vezeluitlijning langs de longitudinale as om de mechanische efficiëntie te maximaliseren door effectieve belastingsoverdracht te garanderen. In werkelijkheid maken beperkingen van het productieproces een perfecte uitlijning onhaalbaar. Variaties zoals golving van de vezels, uitlijnfouten en ongelijkmatige verdeling introduceren microstructurele variabiliteit, die de algehele prestaties beïnvloedt en de betrouwbaarheid in kritieke toepassingen kan ondermijnen.

Voor hoogwaardige industrieën zoals lucht- en ruimtevaarttechniek en autotechniek is het simpelweg tegemoetkomen aan beperkingen van het productieproces niet voldoende. In plaats daarvan zou een verschuiving naar 'microstructuren door ontwerp' - waarbij microstructurele kenmerken doelbewust worden gecontroleerd om te voldoen aan specifieke prestatie eisen - de nauwkeurigheid van de voorspellingen en materiaalsoptimalisatie verbeteren. Om dit te bereiken, is nauwkeurige microstructurele karakterisering vereist om productieprocessen beter te informeren.

Een cruciale stap in de richting van dit doel is het nauwkeurig karakteriseren en beschrijven van de microstructuur van unidirectionele tapes om productieprocessen nauwkeurig te informeren. Recente ontwikkelingen in beeldtechnologieën, met name driedimensionale (3D) beeldtechnieken zoals X-ray Computed Tomography (XCT), hebben onze mogelijkheid om microstructurele kenmerken met ongeëvenaarde scherpheid te onderzoeken, radicaal veranderd. XCT biedt 3D-beelden met hoge resolutie van de interne structuur van composiet tapes, waardoor onderzoekers essentiële kenmerken zoals vezeloriëntatie, -distributie en -defecten met opmerkelijke precisie kunnen vastleggen.

De uitdaging ligt nu in het vertalen van deze rijkdom aan 3D-beeldgegevens naar bruikbare inzichten. Om dit te bereiken, is er behoefte aan een uitgebreide toolbox met metrieken en analytische methoden die zijn afgestemd op de microstructurele analyse van unidirectionele composiet tapes. Deze tools stellen onderzoekers en ingenieurs in staat om de complexiteit van de microstructuur te kwantificeren, kritieke defecten te identificeren en hun implicaties voor materiaaleigenschappen en -prestaties te begrijpen. Bovendien kunnen deze metrieken dienen als maatstaven voor kwaliteitscontrole van de productie, en procesverbeteringen begeleiden om microstructurele variabiliteit te minimaliseren.

De omvang van het proefschrift is om een methodologie te ontwikkelen voor de evaluatie van complexe microstructurele kenmerken in unidirectionele composiet tapes op een driedimensionaal niveau, gebaseerd op informatie verkregen via X-ray Computed

Tomography. In het bijzonder zijn koolstofvezelversterkte tapes met een hoogwaardige thermoplastische matrix geselecteerd als case study voor dit werk, omdat ze een relevante case study vormen voor materialen die worden gebruikt in lucht- en ruimtevaarttoepassingen.

Door drie nieuwe beschrijvingen te introduceren die zijn geïnspireerd door de natuur — differentiële tortuositeit, collectieve beweging en lengte van de buurt — biedt de studie een uitgebreid raamwerk voor het analyseren van de complexiteit van vezelarchitecturen. Differentiële tortuositeit meet afwijkingen van het vezelpad van een ideaal traject, waardoor rand-kerngradiënten worden onthuld waar vezels in de buurt van de randen een grotere verkeerde uitlijning vertonen. Collectieve beweging kwantificeert de uitlijning van vezelgroepen, wat een verminderde coherentie in randgebieden laat zien, waarschijnlijk veroorzaakt door microstructurele verstoringen. De lengte van de buurt beoordeelt de onderlinge connectiviteit van het vezelnetwerk, wat het mogelijk maakt om onderscheid te maken tussen regio's met een hogere vezelassociatie en gebieden met een grotere vezelverstrengeling, en om karakteristieke lengteschalen van vezelassociatie binnen het materiaal te evalueren.

De studie van vezelarchitecturen werd vervolgens uitgebreid naar porositeit gekoppeld aan zowel interne luchtregio's van de tape als hun externe complexe topologie, wat een karakteristieke eigenschap is. De ontwikkelde methode maakt het mogelijk om ruimtelijke distributies op een driedimensionaal niveau te vergelijken, waarbij in de geanalyseerde tape een belangrijke overeenkomst wordt opgemerkt tussen regio's met verhoogde tortuositeit en verhoogde poriedichtheden. Regio's geassocieerd met zeer tortueuse meanderende vezels vertonen een uitgesproken associatie met porositeit die zich zowel in de bulk als op het tapeoppervlak bevindt, wat duidt op een sterke interactie tussen niet-collectieve vezelverplaatsing en de waarschijnlijkheid van porielocatie. Bovendien kwantificeert onze studie de lengteschaal van kenmerkvoortzetting, wat licht werpt op de ruimtelijke omvang van het voorkomen van microstructurele poriën binnen het composiet. Deze bevindingen hebben belangrijke implicaties vanuit een perspectief van karakterisering om modellering strategieën en productieprocessen voor hoogwaardige composieten half-fabrikate-tapes te ondersteunen.

Om echter een representatieve microstructurele vingerafdruk van een gegeven tape te definiëren, leiden onderzoeken met de vereiste kleine voxelgrootte tot beperkte hoeveelheden observaties, die mogelijk niet representatief zijn. Om representatieve resultaten te garanderen, werd een multischaal benadering gebruikt om de bevindingen uit te breiden naar hogere schalen, van microscopische (enkele vezel) tot mesoscopische (afmeting van de tape) lengteschaal, om meer inzicht te genereren in de microstructurele organisatie van thermoplastische half-fabrikate tapes. Door het vermogen van XCT-beeldvorming voor koolstofvezelversterkte thermoplastische composieten op verschillende voxelgroottes te onderzoeken, is het werk gericht op het identificeren van de beperkingen van het gebruik van verschillende schalen van observaties om kenmerken van microstructuren en hun voortplanting van micro- naar mesoschaalniveau vast te leggen. Hoewel structuurtensoranalyse verkeerd uitgelijnde regio's correct leek vast te leggen in XCT-afbeeldingen met een kleine voxelgrootte (1/10 van de vezeldiameter), bleek de methode niet effectief voor afbeeldingen met een grotere voxelgrootte (1/2 van de vezeldiameter).

Algeheel bevordert dit proefschrift de ontwikkeling van methodologieën voor het ver-

eenvoudigen van complexe microstructurele kenmerken in unidirectionele composiet tapes. Verwacht wordt dat de bevindingen de materiaalkarakterisering zullen verbeteren, wat de weg vrijmaakt voor verbeterde optimalisatie van tapeproductieprocessen. Uiteindelijk is dit werk gericht op het ondersteunen van de afstemming van composietarchitecturen om te voldoen aan specifieke prestatievereisten. Deze ontwikkelingen bieden een aanzienlijk potentieel voor het optimaliseren van composietontwerp en het aansturen van innovaties in hoogwaardige toepassingen.





## RIEPILOGO

I nastri compositi unidirezionali sono ampiamente utilizzati nella produzione automatizzata per produrre compositi ad alte prestazioni garantendo una notevole flessibilità di progettazione. Le loro superiori proprietà meccaniche derivano dall'allineamento delle fibre continue in un'unica direzione, caratteristica che li rende ideali per applicazioni ingegneristiche avanzate. Tuttavia, essendo le prestazioni di questi materiali strettamente legate alla loro microstruttura, l'accuratezza nella previsione del loro comportamento richiede una comprensione dettagliata di tali caratteristiche.

I modelli teorici presuppongono un perfetto allineamento delle fibre lungo l'asse longitudinale per massimizzare l'efficienza del trasferimento dei carichi. In realtà, vincoli di produzione rendono impossibile un allineamento perfetto. Variazioni come ondulazione delle fibre, disallineamenti e distribuzione non uniforme introducono una variabilità microstrutturale che influisce sulle prestazioni complessive e può compromettere l'affidabilità in applicazioni critiche.

Per settori che necessitano di alte prestazioni come l'ingegneria aerospaziale e automobilistica, non è sufficiente adattarsi ai limiti di produzione. Al contrario, il passaggio a "microstrutture ottimizzate per uno scopo progettuale", le cui caratteristiche sono deliberatamente controllate per soddisfare specifici criteri di prestazione, migliorerebbe l'accuratezza predittiva. Per raggiungere nel futuro tale obiettivo è necessaria a monte una caratterizzazione microstrutturale precisa per informare al meglio i processi di produzione.

I recenti progressi nelle tecnologie di caratterizzazione per immagine, in particolare le tecniche di visualizzazione tridimensionale (3D) come la tomografia computerizzata a raggi X (XCT), hanno rivoluzionato la nostra capacità di esaminare le caratteristiche microstrutturali in tre dimensioni con un dettaglio senza precedenti. La XCT fornisce immagini 3D ad alta risoluzione della struttura interna dei nastri compositi, consentendo di apprezzare caratteristiche essenziali come l'orientamento delle fibre, la loro distribuzione e difetti presenti nel materiale con elevata precisione.

La sfida consiste nel tradurre questa ricchezza di dati in tre dimensioni in informazioni utili all'ambito della ricerca. A tal fine, è necessario disporre di una serie di metriche adatte all'analisi microstrutturale dei nastri compositi unidirezionali. Questi strumenti consentirebbero a ricercatori e ingegneri di quantificare la complessità della microstruttura, identificare i difetti critici e comprendere le loro implicazioni su proprietà e prestazioni del materiale. Inoltre, queste metriche potrebbero servire come parametri di riferimento per il controllo della qualità della produzione, guidando i miglioramenti del processo per ottimizzare la variabilità microstrutturale.

Lo scopo della tesi è quello di sviluppare una metodologia per la valutazione delle complesse caratteristiche microstrutturali dei nastri compositi unidirezionali a livello tridimensionale, sulla base di informazioni ottenute mediante tomografia computerizzata a raggi X. In particolare, nastri rinforzati con fibre di carbonio e matrice termoplastica ad

alte prestazioni sono stati scelti come caso di studio per questa tesi in quanto caso rilevante ad applicazioni aerospaziali.

Introducendo tre nuove metriche ispirate alla natura - tortuosità differenziale (differential tortuosity), movimento collettivo (collective motion) e lunghezza di associazione (length of neighbourhood) - lo studio fornisce un quadro completo per analizzare la complessità dell'architettura delle fibre. La tortuosità differenziale misura le deviazioni del percorso delle fibre da una traiettoria ideale, rivelando gradienti tra i la superficie ed il centro dei nastri, con fibre vicine alla superficie che mostrano un maggiore disallineamento. Il movimento collettivo quantifica l'allineamento dei gruppi di fibre, mostrando una ridotta coerenza nelle regioni superficiali. La lunghezza di associazione valuta l'interconnettività della rete di fibre, e consente di individuare regioni di maggiore associazione di fibre e valutare le distanze caratteristiche di tali associazioni all'interno del materiale.

Lo studio delle architetture delle fibre è stato poi esteso alla porosità legata sia alle regioni d'aria interne al nastro, sia alla loro complessa topologia esterna, che ne costituisce una caratteristica rilevante. Il metodo sviluppato permette di confrontare le distribuzioni spaziali a livello tridimensionale, evidenziando nel nastro analizzato una significativa corrispondenza tra regioni di elevata tortuosità e aumento della frazione dei pori. Regioni associate in particolare a fibre altamente misallineate (meandering fibres) mostrano una marcata associazione con la porosità localizzata sia nel centro dei nastri che sulla loro superficie, suggerendo una forte interazione tra lo spostamento non collettivo delle fibre e la localizzazione dei pori. Inoltre, il nostro studio quantifica la scala di propagazione di tali caratteristiche, facendo luce sull'estensione spaziale della presenza di pori all'interno del composito. Questi risultati hanno implicazioni significative dal punto di vista della caratterizzazione per informare approcci di modellazione e processi di produzione.

Tuttavia, per definire un'impronta microstrutturale rappresentativa di un determinato nastro, indagini condotte su volumi limitati di materiale portano a informazioni che potrebbero non essere rappresentative della sua variabilità globale. Per garantire la rappresentatività, un approccio multiscale è stato utilizzato per estendere i risultati a scale di osservazioni maggiori, da quella microscopica (livello della singola fibra) a quella mesoscopica (dimensione del nastro), al fine di fornire maggiori informazioni sull'organizzazione microstrutturale dei nastri compositi termoplastici. Il lavoro mira ad identificare i limiti dell'uso di diverse scale di osservazione per catturare le caratteristiche delle microstrutture e la loro propagazione dal livello micro- a mesoscopico. Mentre l'analisi dei tensori di struttura è apparsa in grado di catturare correttamente le regioni disallineate con voxel di piccole dimensioni ( $1/10$  del diametro della fibra), il metodo si è rivelato inefficace per le immagini con voxel di dimensioni maggiori ( $1/2$  del diametro della fibra).

Complessivamente, questa tesi promuove lo sviluppo di metodologie per la deconvoluzione di caratteristiche microstrutturali complesse nei nastri compositi unidirezionali. I risultati ottenuti forniscono indicazioni valide a migliorare la caratterizzazione di tali materiali, aprendo la strada verso nuove strade per l'ottimizzazione dei processi di produzione dei nastri. Per concludere, questo lavoro mira a supportare l'ottimizzazione delle architetture composite per soddisfare specifici requisiti di prestazione. Questi progressi hanno un potenziale significativo per l'ottimizzazione della progettazione dei compositi e la promozione di innovazioni nelle applicazioni ad alte prestazioni.

# 1

## INTRODUCTION

## 1.1 THE ROLE OF UNIDIRECTIONAL COMPOSITES IN ADVANCED ENGINEERING

Unidirectional composite materials have become a cornerstone of modern engineering, offering exceptional mechanical performance for applications requiring lightweight, high-strength solutions. These composites consist of continuous fibres embedded in a matrix and are specifically designed to maximise strength and stiffness along a single direction. Their unique properties have made them indispensable in aerospace, automotive, and renewable energy industries, where achieving optimal material performance is closely tied to weight reduction and reliability. Among these materials, unidirectional composite prepreps, or tapes, play a critical role in automating the manufacturing of composite parts.

The outstanding mechanical properties of unidirectional composites—such as tensile strength, compressive stiffness, and fatigue resistance—are intrinsically linked to the precise alignment and uniform distribution of fibres within the matrix. Ideally, the fibres in these tapes are supposedly perfectly aligned along the longitudinal axis, ensuring that mechanical loads are efficiently transferred. However, close observation of the structures reveals a level disorder, which is not well understood in its microstructure, nor are the effects leading to it. Imperfections such as fibre waviness, misalignments, and uneven distribution frequently occur, introducing defects that compromise the material's mechanical reliability and consistency. As a result, the performance of components made from unidirectional tapes is closely tied to their microstructural characteristics, and understanding this relationship is crucial for optimising these materials.

In generalised terms, we know that microstructure defects govern the performance of many classes of materials, such as grain morphology and lattice defects in metals. In advanced applications of composite materials where reliability and consistency are non-negotiable, it is necessary to move beyond merely accepting manufacturing-induced imperfections. A promising paradigm shift is the concept of 'microstructures by design', where the microstructure is intentionally controlled and tailored to meet specific performance requirements. This approach would enable engineers to predict and optimise material behaviour with much greater accuracy, ensuring that composite parts meet the stringent demands of high-performance industries. Achieving this goal necessitates not only advanced manufacturing techniques but also a deeper understanding and precise characterisation of microstructural variability that moves from a traditional two-dimensional cross-sectional approach to the study of composites to a three-dimensional evolution of variability.

Recent advancements in imaging technologies, particularly three-dimensional (3D) imaging techniques like X-ray Computed Tomography (XCT), have revolutionised the study of unidirectional composite microstructures. XCT provides high-resolution 3D images of the internal structure of composite tapes, enabling researchers to capture critical microstructural features such as fibre alignment, distribution, and defects with remarkable precision. This capability has significantly enhanced our understanding of the origins and impacts of variability. However, translating this wealth of data into actionable insights remains a significant challenge.

There is a growing need for a comprehensive quantifiable descriptive vocabulary and analytical methods tailored to the 3D microstructural analysis of unidirectional composites.

Such tools would allow researchers and engineers to quantify microstructural complexity, identify critical defects, and evaluate their implications for material properties and performance. Moreover, these metrics could serve as benchmarks for manufacturing quality control, guiding process improvements to minimise variability and maximise performance.

This chapter explores the critical aspect of the characterisation of microstructural features, detailing advanced methodologies developed for variability characterisation in unidirectional composite tapes, and possible novel approaches. Based on the literature proposed, research gaps are highlighted. To conclude, the objective and scope of the thesis and its outline are presented.

## 1.2 CHARACTERISATION OF THREE-DIMENSIONAL VARIABILITY IN UNIDIRECTIONAL COMPOSITE MICROSTRUCTURES

Microstructural features are pivotal for understanding and modelling the performance of unidirectional composites (UDCs) [1]. Size effects [2], microscale variability [1, 3–6], and local fibre orientation [7–12] impact mechanical properties [13, 14] and processability [15]. Recent research has highlighted the importance of understanding the three-dimensional (3D) variability in fibre arrangements for advanced material modelling [14, 16].

A variety of methods are available to reconstruct the 3D microstructure of UDCs. Optical microscopy slicing, which involves acquiring sequential images through cyclic grinding and polishing, provides detailed insights but is labour-intensive and destructively alters specimens [17]. More recently, X-ray-based techniques such as X-ray Computed Tomography (XCT) and X-ray Synchrotron Radiation Micro-Computed Tomography (SRCT) have become prominent due to their ability to capture volumetric data in a highly automated manner. Despite lower contrast between fibres and matrix materials, especially in carbon-fibre reinforced composites, and reconstruction artefacts, XCT and SRCT have enabled successful post-processing via techniques such as individual fibre tracking [18–20], Digital Volume Correlation (DVC) [14], and structure tensor analysis [21, 22]. Single-fibre tracking offers the unique advantage of providing complete 3D reconstructions of fibre architectures, essential for accurately attributing properties to individual fibres [23].

Recent work emphasises the significance of meso- and microscopic features in fibre organisation, uncovering the potential for complex fibre movements. For instance, Fritz et al. used XCT to analyse resin-rich pockets and intralaminar sub-microvoids, revealing ‘stray fibres’ with pronounced deviations from unidirectional alignment [24]. Emerson et al. employed SRCT to observe in-situ compression behaviour, identifying micro-buckling and fibre twisting as load increased [18, 19]. Further advances have come from novel applications of clustering techniques like k-means to analyse fibre alignment [25]. Fast et al. expanded traditional metrics by introducing topological and Euclidean analyses to quantify microstructural variability and clustering in fibre arrangements [26]. Notwithstanding these efforts, the understanding of patterns in collective fibre organisation has not been well addressed in fibre composites literature. This would, however, be relevant in elucidating the mechanisms of microstructure formation, spatial organisation and evolution.

### 1.3 COMPLEX STRUCTURAL ORGANIZATION IN NATURE

Collateral fields have been developing solutions to describe complex structural organisations. Examples come, for instance, from biology, in the study of time-dependent phenomena such as bird murmuration, which show a high level of organisation [27, 28]. In the analysis of the internal microstructural architecture of silk cocoons [29], Figure 1.1a) highlights effects in the fibre packing density through the thickness of the structure captured via X-ray Computed Tomography, highlighting an edge-core effect in the parameter distribution. Input from collateral research fields can therefore aid in defining novel metrics for the three-dimensional characterisation of unidirectional composites.

For example, tortuosity, defined as the ratio of the actual fluid path to a straight line distance [30], has been used to study the architecture of collagen fibre assemblies in the corneoscleral shell of sheep eyes [31] and gas transport through carbon nanotube arrays [32]. While not yet applied to UDCs, tortuosity could provide valuable insights into local fibre alignment and microstructure formation mechanisms.

The study of collective organisation, often employed in biological systems, offers additional metrics linked to swarming at a cellular level [33], coherent directional motion in animal locomotion [34], and velocity correlation functions in pigeon flocks [35]. Analogous approaches could be adapted for UDCs to analyse fibre variability along the tape length, using axial position as a temporal analogy.

Understanding the architectural interconnectivity of fibrous materials can offer critical insights into their morphology and mechanical properties. For example, silkworm cocoons exhibit a high fibre orientation aligned with tensile directions, enhancing tensile performance [29]. Similarly, fibre intersection density has been studied in bird nests [36], with a visual representation shown in Figure 1.1b), and glass fibres [37] to understand how contact points influence material strength. Fast et al. introduced the collateral concept of fibre neighbour exchange rate to the case of ceramic UDCs and carbon fibre/epoxy UDCs, hypothesising a link between fibre entanglements and damage progression [26].

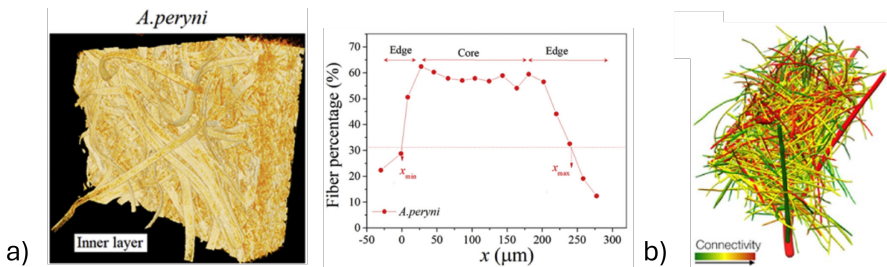


Figure 1.1: a) Left: 3D tomography of the surface of a silk cocoon; Right: through-thickness edge-core effect in the fibre percentage, reproduced from [29] b) Connectivity within the fibre network of a bird's nest, reproduced from [36].

## 1.4 RESEARCH GAPS

- **Lack of comprehensive 3D descriptors:** although tortuosity has been widely applied in other fields, such as gas transport in carbon nanotubes and collagen fibre studies, it has not yet been adapted for studying fibre organisation in UDCs [30, 31]. Investigating its application to map local variations and understand microstructure formation could provide significant insights. Descriptors from biological systems, such as vorticity, coherent directional motion, and velocity correlation functions, have not been applied to UDCs [33–35]. These could be used to improve understanding of fibre local ordering effects, bundling, and path variability along the tape length.
- **Lack of literature on 3D variability of unidirectional composite tapes:** Current attention in literature from a three-dimensional microstructural perspective is given mainly to consolidated composite laminates, but limited studies are dedicated to composite tapes. While studying the microstructure of laminates is key in linking the microstructure to the material performance, limited information is available on the original characteristics of the base material. Knowledge of tape architectures would enable us to gain insight into tape microstructure formation and the performance of the final part.
- **Interrelation of defects at pores and fibre level:** pore locations have been qualitatively linked to misaligned stray fibre effects, but a quantitative relationship remains unexplored [38]. This could reveal how microstructural defects propagate and influence composite properties. While some studies highlight the potential of designing porosity for enhanced air removal and processability [39], the implications of such strategies on mechanical performance and microstructural integrity are not well understood.
- **Need for multiscale approaches integration across scales:** High-resolution techniques like XCT and SRCT provide detailed information about individual fibres. Still, measurements that allow the resolution of individual fibres are limited in their field of view, making it impractical to analyse larger areas for quality screening and process optimisation. A scalable solution that balances resolution and area coverage is needed. The lack of robust methodologies to bridge high-resolution observations (e.g., single-fibre tracking) with macroscale variability (e.g., bulk tape analysis) limits the ability to comprehensively study microstructure formation and evolution [22]. Multiscale techniques must be developed to maintain critical information across scales. Structure tensor analysis is effective at broader resolutions, but its performance at varying voxel sizes needs further exploration to minimise information loss [21, 40].

## 1.5 OBJECTIVES AND SCOPE

The scope of the thesis is to further the understanding of complex microstructural features in unidirectional composite tapes at a three-dimensional level, based on information obtained via X-Ray Computed Tomography. In particular, carbon fibre-reinforced tapes with a high-performance thermoplastic matrix have been selected for this work since they constitute a relevant case study for materials used in aerospace applications.

Via high-resolution measurements allowing single fibre trajectories identification, the objective is to investigate various levels of complexity in fibre arrangements, by examining both individual fibres and their interactions within their surrounding neighbourhoods. In particular, the aim is to explore whether quantitative descriptors from other research fields, such as tortuosity and collective motion, could provide insights into the different levels of organisation in a hierarchical approach. Consequently, this work should also investigate the relationship between these descriptors of fibre organisation and tape pore locations to develop a methodology that connects the spatial characteristics of tapes across different constituent levels.

Furthermore, in the scope of bridging high-resolution observations with macroscale variability, this study also aims to capture fibre organisation and defects at different scales of observation. In the spirit of building a framework for multiscale composites analysis, this research seeks to develop methodologies that enable comprehensive understanding across multiple scales and assess information loss at varying voxel sizes.

The research also includes methodologies to extract characteristic material length scales of feature propagation. The outcome is expected to allow for future work-informed design of material representative volume elements (RVEs).

Since this research focuses on the development of an analytical methodology, the proposed descriptors and approaches are designed to be applicable across different fibre/resin system combinations and processing conditions. The work has the potential to be applied both on single ply tapes, as well as consolidated laminate or dry fibre mats.

## 1.6 THESIS OUTLINE

The thesis is structured around three principal chapters, each systematically addressing specific aspects of the research on the microstructural characterization of unidirectional composite tapes. While presented as a collection of manuscripts and conference papers, this format reflects the research's progression, with each chapter contributing independently to distinct but interconnected facets of the overall study. A conceptual abstract of the work is shown in Figure 1.2.

**Chapter 2** introduces three novel descriptors — differential tortuosity, collective motion, and length of neighbourhood — to quantify fibre microstructural organisation in unidirectional composites. These descriptors address increasing levels of complexity, from individual fibre deviations to group dynamics and connectivity. A key finding is the presence of edge-core gradients, where fibres near tape edges exhibit higher misalignment and reduced connectivity due to manufacturing processes. The study highlights interrelations between descriptors, providing insights into how local misalignments influence global behaviour. This methodology bridges gaps between traditional characterisation techniques and interdisciplinary approaches, offering tools to optimise composite performance and modelling.

**Chapter 3** explores the relationship between porosity and fibre alignment in unidirectional composite prepregs using advanced 3D X-ray micro-computed tomography. Findings reveal that regions with higher fibre tortuosity and misalignment correlate with increased porosity, particularly at tape edges. These areas, shaped by manufacturing-induced gradients, pose mechanical vulnerabilities such as reduced stiffness and higher fracture risks.



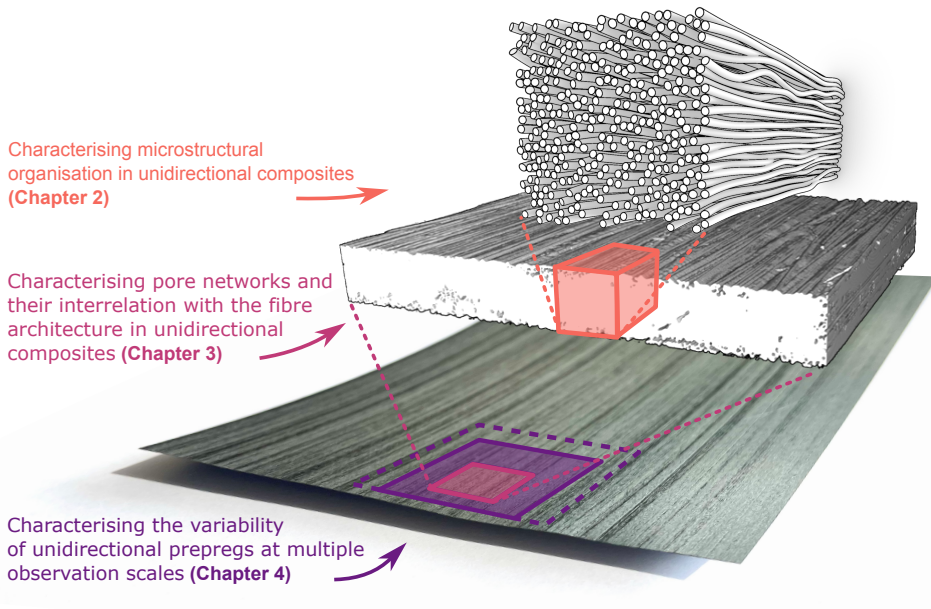


Figure 1.2: Graphical abstract of the thesis work indicating the hierarchy of the study.

The study provides valuable metrics for quantifying pore distribution and its propagation, emphasising the role of fibre architecture in influencing material properties.

**Chapter 4** develops a multiscale methodology for characterising the microstructural variability of unidirectional carbon fibre-reinforced thermoplastic prepreg tapes. By employing XCT imaging at varying voxel resolutions, the research evaluates both fine-scale (fibre-level) and mesoscale (tape-level) features, focusing on fibre misalignment and porosity distribution. Structure tensor analysis emerges as a scalable alternative to single-fibre tracking, enabling efficient detection of misalignment patterns, though its accuracy diminishes at coarser resolutions. The study provides recommendations for optimising voxel resolution, filtering techniques, and manufacturing processes to improve composite characterisation and quality.

**Chapter 5** discusses the key findings from this work, emphasising its contributions to the broader context. It also outlines recommendations for future research directions based on the outcomes of the thesis.



## 2

# CHARACTERISING MICROSTRUCTURAL ORGANISATION IN UNIDIRECTIONAL COMPOSITES

*Understanding the three-dimensional variability of unidirectional composites is relevant to the material performance and the development of advanced material modelling strategies. This work proposes a new methodology for the characterisation of unidirectional composites, showcased on carbon fibre/poly(ether-ether-ketone) tapes. Three microstructural descriptors were here introduced, each representing an increasing level of complexity in the fibre architecture: from a tortuosity-based single fibre trajectory analysis to fibre groups' behaviour, to fibre network interconnectivity. The methodology was developed and validated on real material datasets acquired via X-ray computed tomography. A facile method for image analysis was used to reconstruct the three-dimensional fibrous architecture at a single fibre path resolution. The approach bridges a gap in the traditional approach and nomenclature typical of the composite field to describe and quantify complex fibre organization in unidirectional composites, highlighting micro- and mesoscopic features, such as edge-core effects in the fibre arrangement, possibly occurring in tow spreading. The study of the parameter interdependence showed relationships, which will provide further insight for future research in the study of microstructure formation of unidirectional composites, its evolution during processing or loading, and input for advanced modelling techniques based on Representative Volume Elements.*

## 2.1 INTRODUCTION

Microstructural features are relevant for understanding and modelling unidirectional composites (UDCs) performance [1]. Size effects [2], microscale variability [1, 3–6], and local fibre orientation [7–12] do have an impact on mechanical properties [13, 14] and processability [15]. In particular, understanding the three-dimensional (3D) variability in the fibre arrangement of UDCs was highlighted for its importance in advanced material modelling [14, 16]. Different routes are available for the reconstruction of the 3D unidirectional microstructure. Optical microscopy slicing works with the acquisition of several images along the length of the UDC by performing cyclic grinding and polishing steps [17]. This method is however labour-intensive and leads to destructive alteration of the specimen. X-ray based techniques such as X-ray Computed Tomography (XCT) and Synchrotron Radiation Micro-Computed Tomography (SRCT) have been receiving increasing interest for their ability to capture volumetric data with high automation. Even though characterized by a lower contrast between fibre and matrix and by reconstruction artefacts, successful post-processing of the obtained volume was performed via individual fibre tracking [18–20], Digital Image Correlation [14, 20], and homogenisation tensor [22, 42]. Single fibre paths tracking comes with challenges related to the high resolution and contrast required to identify single fibre centres, especially in carbon fibre composites, where the fibre diameter is typically in the order of  $7\text{ }\mu\text{m}$  [23]. It has however the advantage of a full 3D reconstruction of the fibre architectural arrangement, and the possibility to correctly attribute properties to single fibres.

Recent work highlights the relevance of understanding micro- and mesoscopic features in the fibre organisation, hinting at the emergence of complex fibre movements. Fritz et al. [24] used XCT to analyse the microstructure of intralaminar tow-aligned resin rich pockets, which are intra-tow features that were theorised to be related to spreading, and on the characterization of intralaminar sub-microvoids in aerospace grade composites. ‘Stray fibres’ have been observed at the ply interface, typically showing greater deviation from the main unidirectional orientation by crossing the path of multiple fibres [24]. Zehnder et al. performed reconstruction of single fibres based on XCT data in bent unidirectional samples via particle tracking algorithms. The work highlighted challenges in tracking fibres in media with small features and low contrast between the different constituents, which is made worse by bending [23]. Mehdikhani et al. analysed SRCT data via both DIC and single fibre tracking to map local fibre misalignment, quantifying differences in the in-plane and out-of-plane direction [14]. In the work of Emerson et al., SRCT was used to evaluate the in-situ behaviour under compression loading using a single fibre tracking algorithm [18], observing the evolution of micro-buckling and kinking at different load steps [19]. They were able to qualitatively show spatial variations in the azimuthal fibre alignment with increasing load, showing a tendency to an increase in both fibre misalignment with the axial direction and global twisting of the fibre network. Wang et al. expanded this study by using XCT analysis to further studying segregation effects in the fibre alignment and local buckling by means of k-means clustering [25]. The work of Fast et al. represents one of the most comprehensive efforts to quantify microstructural variability in fibre reinforced composites following single fibre tracking [26]. The authors employed topological and euclidean metrics to characterise unidirectional composite volumes acquired via SRCT. The analysis addressed the quantification of both traditional descriptors such as local

fibre volume and orientation, as well as less explored concepts such as Voronoi fibre neighbourhood analysis, to highlight clustering in fibre neighbours association.

Even though complex fibre arrangements are observed, the parameters used to quantify these phenomena are mostly still bounded to a traditional approach and nomenclature typical of the composite field. By looking into other research domains, new approaches for investigating these features can be found.

In the context of studying the permeability of fibre bundles, tortuosity was defined as the ratio between the distance covered by the fluid during permeation and the distance as if it was a straight line [30]. Tortuosity was also used by Wojciech et al. to characterise gas transport kinetics regimes through randomly oriented carbon nanotube arrays [32]. This is a local parameter that can provide insight on differences in functional organisation. In the study of the collagen fibre architecture of the eye, the same definition was applied to map local variations for the identification of different functional regions [31]. The concept of tortuosity has however not been applied yet to study fibre organisation in unidirectional composites, but could prove useful in mapping local variations in their arrangement. This might both help characterise the mechanisms of microstructure formation, and the micromechanical effect of local variability in fibre alignment.

The understanding of patterns in collective fibre organisation has not been well addressed in fibre composites literature. This would however be relevant to gain a greater understanding of the microstructure formation, spatial organisation and evolution. In biological sciences, the study of collective organisation is conducted in relation to animal locomotion [28, 42]. Various descriptors are used to characterise collective phenomena, from vorticity in cell assembly [33] to coherent directional motion parameters [34], to velocity correlation functions for hierarchies in birds flocking motion [35]. Similar models could help to capture local order regions in materials of engineering interest. For unidirectional composites, such descriptors could be used to study both microstructural formation and local variability in the fibre arrangement in the length direction of the UDC, using in this case an analogy between time and axial position.

The study of the architectural interconnectivity of fibrous materials can further add to understanding its morphology. In silkworm cocoons, for example, greater fibre orientation with the tensile direction and higher fibre intersection densities appear to contribute to higher tensile performance [29]. Edge-core effects in the local fibre content are also observed, with a decreasing fibre volume from the centre to the edges. The fibre intersection density was also evaluated in the architecture of bird nests to characterize their network [36], by tracking the number of contacts between straws. A similar approach was used by Viguie et al. to study fibre contacts in fibrous material of diverse origins, from glass fibres to cellulosic fibres [37]. Fast et al. applied a similar concept to study of unidirectional microstructures, hypothesising an effect on the fracture toughness of composites [26].

This work takes a step forward in the 3D characterization of UDCs to elucidate their microstructural complexity. The aim is to develop new approaches for more advanced quantification of complex phenomena such as microstructure formation and evolution, and for the generation of RVEs for advanced material modelling. This is done by introducing novel descriptors which address the local fibre architecture at an increased level of complexity. Such descriptors are based respectively on the concepts of tortuosity, collectivity in the fibre motion, and length of neighbourhood to quantify the network interconnectivity.

Section 4.2 addresses the reconstruction of the 3D fibre architecture of unidirectional fibre composites. X-ray computed tomography was used for the image acquisition, and a facile method for image analysis was used for the 3D data reconstruction. Section 2.3 introduces the novel parameters used for the fibre path analysis. The results of the application of the methodology to selected UDCs, and the discussion of the identified hierarchies and parameter interdependence, can be found respectively in Section 2.4 and 2.5. Conclusions and indications for future work will be addressed in Section 2.6.

## 2.2 METHODOLOGY

The methodology developed is based on computational image analysis of real material datasets, which are available at DOI: 10.4121/16437297. The purpose of this section is to identify an analysis workflow that can be applied to similar unidirectional materials as well, such as any continuous fibre-matrix systems.

### 2.2.1 SAMPLE PREPARATION

The methodology was showcased by using two commercial aerospace-grade unidirectional tapes of carbon fibre and poly(ether-ether-ketone). The tapes have a nominal fibre volume fraction of 59% and 47% respectively, and a thickness of 150  $\mu\text{m}$  and 200  $\mu\text{m}$ , and hereby called Tape A and Tape B. Samples of 10 mm in fibre direction and 1.5 mm in width direction were harvested from a larger tape roll.

### 2.2.2 TOMOGRAPHIC IMAGE COLLECTION

The data reported was acquired via X-ray micro-computed tomography with a Zeiss Xradia 520 Versa, which is a state of the art instrument used in recent literature [10, 18, 23–25, 43]. A resolution of 0.7232  $\mu\text{m}$ , corresponding to about 10 pixels per fibre diameter, was selected to facilitate single fibre identification similarly as in previous work [18, 19, 23, 24]. A 2000x2000 pixel detector in binning mode 2 was used with a 4x magnification lens, leading to a resulting scan volume of approximately 700  $\mu\text{m}$  by 200  $\mu\text{m}$  in the tape cross-section and 723  $\mu\text{m}$  in the tape length direction. A voltage-to-power ratio of 100/9 kV/W and an exposure time of 6 s were used for the image acquisition. A representative cross-section of the two materials is shown in Figure 2.1a) and b). The measurement was repeated three times in the fibre length direction, and the volumes were stitched together to cover a total tape length of about 1800  $\mu\text{m}$ , of which about 1450  $\mu\text{m}$  have been used for the following analysis.

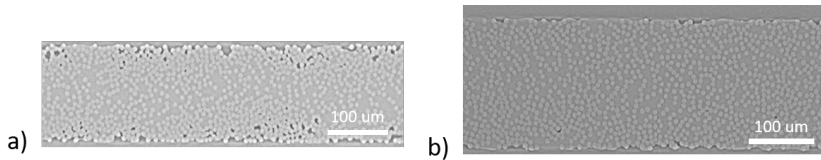


Figure 2.1: X-ray computed tomography cross-section of a) Tape A and b) Tape B.

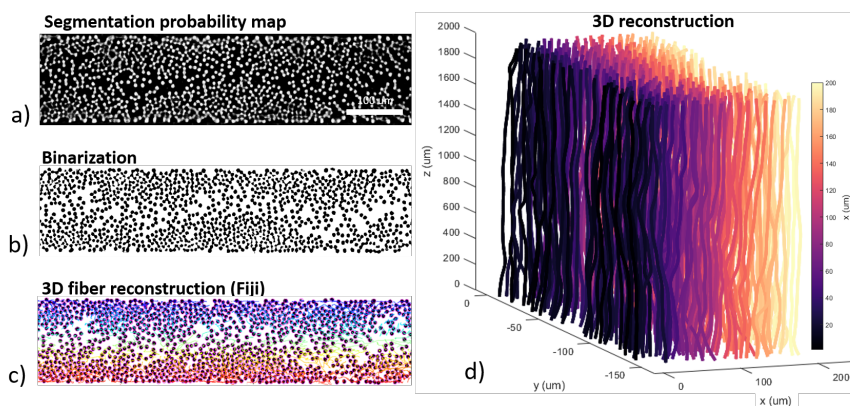


Figure 2.2: Workflow for image analysis and fibre path reconstruction, based on Tape A a) Image segmentation, conducted with Trainable Weka segmentation. The scalebar in white indicates a distance of  $100\ \mu\text{m}$  b) Image binarization via thresholding c) fibre path reconstruction using Trackmate, colour-coded according to the average through-thickness position of the fibre paths d) 3D reconstructed fibres for a portion of the tape, colour-coded along the tape width direction.

### 2.2.3 FIBRE PATH RECONSTRUCTION

The reconstructed volume was processed by Fiji software plugins [44]. Linear stack alignment with Scale Invariant Feature Transform (SIFT) [45] was used for image registration to correct for sample tilt. The workflow for fibre path reconstruction after this step is showcased for the case of Tape A in Figure 2.2. To correctly distinguish fibres from local reconstruction artefacts, fibre segmentation was performed via Trainable Weka Segmentation [46], a machine-learning-based tool that allows for image classification based on a training set provided by the user. Approaches based on automated feature recognition based on training sets was also used in recent literature [18, 19, 25]. A training set of three slices was employed with classification in two classes – fibres and not-fibres – which was then applied to the full dataset. The output of the segmentation is a probability map, which can then be further processed. An example is shown in Figure 2.2a), where the locations with a higher chance to be associated with fibres are highlighted with a lighter colour in the greyscale image. A data reduction scheme was then applied by averaging groups of 10 consecutive probability maps (equivalent to  $7.2\ \mu\text{m}$  in the fibre direction) to lower the computational cost of the following steps and to increase accuracy by further mitigating the effect of segmentation artefacts and noise.

Image thresholding was then performed, leading to a binarized result as in Figure 2.2b), followed by fibre path reconstruction via the plugin TrackMate [47]. TrackMate is a tool originally designed for cell biology to track single entities in time-resolved problems. This approach can be adjusted to track fibre centre translation between slices. Since the measurement is ‘space resolved’ rather than ‘time resolved’, the result will be later interpreted by exchanging the time coordinate with the relative axial coordinate along the tape length. The tool employs a two-steps approach for fibre track reconstruction: fibre centre identification, followed by fibre centre linking. For the first step, a Difference of



Gaussian filter was used. For the second step, a Linear Motion LAP (Linear Assignment Problem) tracker was used. This method is based on the use of a Kalman filter for the identification of the most probable position of the fibre in consecutive cross-sections. Analogous approaches have been already used for similar problems in the composite field [17, 20] and are quite established in the life sciences environment for particle tracking [42, 48].

A search radius of 10  $\mu\text{m}$  and maximum gap linking distance of 16 steps (corresponding to about 115  $\mu\text{m}$ ) were used. Consistently with the data reduction scheme used, the fibre centres determined are spaced of 7.2  $\mu\text{m}$  in the tape longitudinal direction.

A map showing the resulting analysed tracks, colour-coded according to their average thickness position, is showed in Figure 2.2c). The coordinates of fibres which could be followed entirely through a region of 1450  $\mu\text{m}$  were extracted and imported in MATLAB for further analysis. This led to detection of about 80% of the theoretical number of fibres for the given material volume. This does not consider fringe fibres at the side edges of the tape, which might not be fully imaged, and therefore were not fully reconstructed [26]. A portion of the resulting fibre distribution is shown for Tape A in Figure 2.2d).

## 2.3 MICROSTRUCTURAL DESCRIPTORS

Three parameters are introduced for the analysis of the microstructural variability of UDCs: differential tortuosity, collective motion, and length of neighbourhood. They represent respectively information on single fibre trajectory, similarities in fibre paths to identify group motion, and network interconnectivity within the material, addressing the architectural study of the material starting at a single fibre level towards an increasingly larger domain in the 3D space. The goal is to assess these parameters on the reconstructed fibre paths, understand their variability and explore interdependencies between them.

### 2.3.1 DIFFERENTIAL TORTUOSITY

In the context of studying the permeability of fibre bundles, tortuosity was used to quantify the deviation of the permeation trajectory from a straight path [30]:

$$\tau = \frac{L}{L_0} \quad (2.1)$$

where  $L$  is the distance covered by the fluid during permeation, and  $L_0$  the distance as if it was a straight line. By definition, this parameter is greater than 1, which corresponds to a perfectly straight fibre. For a unidirectional microstructure such as the ones object of study, the value of tortuosity is assumed to be close to unity [30]. The downside of this definition is that it does not allow to highlight the order of magnitude of the variation in local property.

An alternative definition is introduced in this work as differential tortuosity  $\tau^d$  as a modification of Equation 2.1. Differential tortuosity represents the difference between the tortuosity of a real fibre and the tortuosity of an ideal straight fibre aligned longitudinally with the scan volume, and starts from a value of 0. This allows for a more intuitive representation of highly aligned fibre populations via its order of magnitude, expressed in



a logarithmic scale. Differential tortuosity is defined as:

$$\tau^d = \tau - 1 = \frac{L - L_0}{L_0} \quad (2.2)$$

where in this case,  $L$  represents the total length of the fibre and  $L_0$  is the size of the scan volume.

A schematic is shown in Figure 2.3. The total fibre length was measured as polygonal conducted through the fibre centre coordinates. For the data reduction scheme used, such points occur at an interval of  $\Delta z = 7.2 \mu\text{m}$  in the fibre length direction.

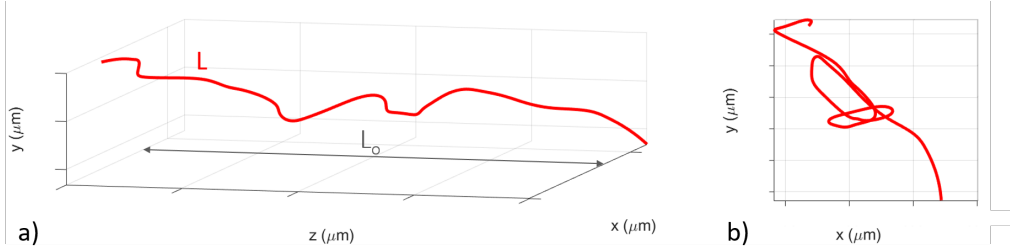


Figure 2.3: Example of a tortuous fibre trajectory. The fibre is represented with a solid red line of total length  $L$ , in a) 3D, b) 2D view, orthogonal to the tape axis. A volume of length  $L_0$  is shown.

### 2.3.2 COLLECTIVE MOTION

In the case of UDCs, collective motion equations could be used with the objective to study how the fibre architecture develops along their axial direction. Local synchronous motion patterns were characterised in biology through the collective motion parameter [34]:

$$\Phi(i, t) = \frac{1}{N_r} \sum_{j \in C_r} \frac{v_i(t) \cdot v_j(t)}{|v_i(t)| |v_j(t)|} \quad (2.3)$$

where  $C_r$  is the circle of radius  $r$  surrounding element  $i$  at time  $t$ ,  $N_r$  is the number of elements  $j$  contained in  $C_r$ , and  $v_i(t)$  and  $v_j(t)$  are local velocities, whose directions are tangent to the trajectory of the respective element. By the definition of the dot-product, Equation 2.3 averages the cosine of the relative velocity vector angle between fibres  $\cos\theta$  and is therefore sensitive to relative motion directionality. If orientation rather than the polarity of motion is relevant,  $\cos^2 \vartheta$  can be used to evaluate local order in studies of liquid crystal polymers alignment [49].

A variation from the literature parameter is introduced in this work for the analysis of UDCs in their axial direction to conduct the analysis in space along the fibre length rather than in time. The analysis is therefore not time-resolved but space-resolved. Moreover, the fibre neighbourhood is defined here according to a Voronoi tessellation [26, 50]. The immediate neighbours according to the tessellation are considered for the averaging, consisting of the neighbouring cells which share an edge with fibre  $i$ .

This parameter is calculated for each fibre based on its surroundings for each 2D slice of the processed volume. The collective motion parameter CM for fibre  $i$  at the location  $z$  along the tape axis is defined as:

2

$$CM(i, z, \Delta z) = \frac{1}{N_{V_i}} \sum_{j \in V_i} \frac{d_i(z, \Delta z) \cdot d_j(z, \Delta z)}{|d_i(z, \Delta z)| |d_j(z, \Delta z)|} = \frac{1}{N_{V_i}} \sum_{j \in V_i} \cos \vartheta_{ij}(z, \Delta z) \quad (2.4)$$

where  $z$  is the axial position,  $\Delta z$  is the axial resolution for the displacement calculation,  $V_i$  is the Voronoi neighbourhood of the reference fibre  $i$  at position  $z$ ,  $N_{V_i}$  is the number of fibres  $j$  contained in the neighbourhood  $V_i$ ,  $d_i(z, \Delta z)$  and  $d_j(z, \Delta z)$  are the in-plane displacements vectors on the cross-section considered, for the fibre  $i$  and its Voronoi neighbours, respectively,  $\vartheta_{ij}$  is the angle between the displacement directions of the two fibres. Since the displacements approximate the tangent to the fibre path, smoothing of the fibre trajectories was conducted to remove residual noise from the fibre tracking operation [43]. This was done in MATLAB via a *loess* algorithm, which employs a weighted quadratic polynomial. A smoothing factor of 0.15 was used, which corresponds for these datasets to an interpolation span of about  $220 \mu\text{m}$  (about 30 slices). This allows to filter out shorter range effects and highlight longer range collective mobility.

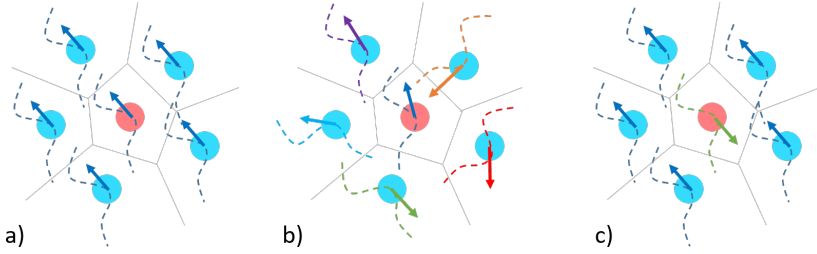


Figure 2.4: Application of the collective motion parameter to a particle in its neighbourhood, for a value of a) 1 (synchronous motion) b) 0 (random motion) c) -1 (counter-streaming). The reference fibre centre is highlighted in red, and its immediate neighbours in blue. The local in-plane displacement vector between two slices is shown by an arrow, and the trajectory by a dashed line.

The value of CM varies in  $[-1, 1]$ , where 1 represents perfectly coherent motion where all fibres move parallel and in the same direction, -1 is the case of counter-streaming (fibres moving parallel to each other but in the opposite direction), and the intermediate value 0 represents random motion. This parameter is local and can be mapped on each tape cross-section. A schematic is shown in Figure 2.4. In this case,  $\Delta z$  was set to  $7.2 \mu\text{m}$  according to the resolution of the data reduction scheme used. The median value of CM along the  $z$  axis is calculated for each fibre to highlight fibre interactions that last through the entire scan volume considered.

### 2.3.3 LENGTH OF NEIGHBOURHOOD

The fibre contacts within the volume have been analysed by looking at the level of inter-connectivity within the tape, with inspiration to the study of bird nests [36] and fibrous scaffolds [51]. The approach follows a similar reasoning as the one used by Fast et al. [26]

in analysing variations in fibre composites. The Voronoi neighbourhood of a fibre is in general not constant, but changes due to the movement of the fibres through the volume. A schematic is shown in Figure 2.5, where the evolution of a neighbourhood through space is represented by fibres approaching and leaving the vicinity of the reference fibre. The fibre network is analysed here by looking at the axial length for which two fibres remain in close contact before moving to different neighbourhoods. The median distance along the fibre path for which a contact is maintained is defined as length of neighbourhood, or LON:

$$LON(i) = \widetilde{LPN}(i, j)_{j \in V_{ci}} \quad (2.5)$$

where  $V_{ci}$  is the cumulative Voronoi neighbourhood, defined as the multitude of individual fibres that enter the vicinity of fibre  $i$  at some point in space,  $j$  is a fibre contained in  $V_{ci}$ , and  $\widetilde{LPN}(i, j)$  represents the median of the pairwise length of neighbourhood  $LPN$  between fibre  $i$  and each neighbour  $j$ . The length of neighbourhood was calculated on the same tessellation generated to determine the collective motion.

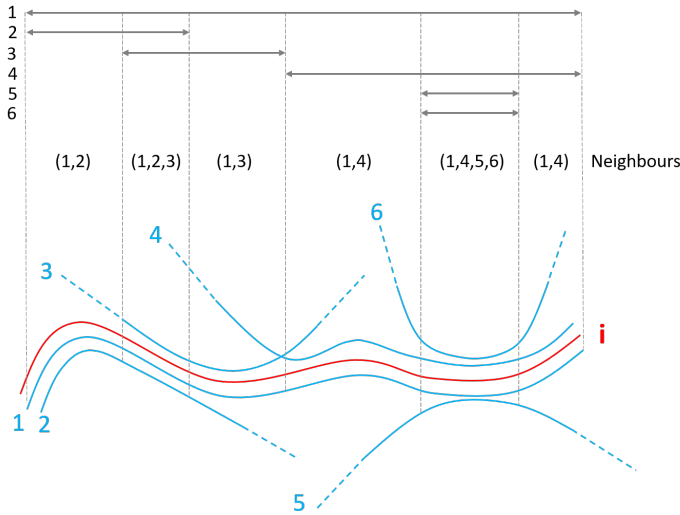


Figure 2.5: Contact tracing concept represented for a 2D case. The neighbourhood of the reference fibre  $i$  (in red) varies through space, with fibres both approaching and leaving its vicinity. The local neighbourhood is indicated in brackets, while the arrows show the length of change LC between fibre  $i$  and each neighbour.

## 2.4 RESULTS

### 2.4.1 DIFFERENTIAL TORTUOSITY

Differential tortuosity  $\tau^d$  was determined as in Equation 2.2, with its value ranging from about 0.0001 to 0.01 for both tapes, spanning across three orders of magnitude. Assuming that the order of magnitude of the parameter is more representative of differences between

fibres compared to its small variations, the logarithm of  $\tau^d$  was considered for further analysis. The parameter distribution for the two tapes is represented in Figure 2.6, highlighting higher differential tortuosity for Tape A compared to Tape B, shown by a shift to higher values. As a reference benchmark, the corresponding median value of tortuosity related to the global fibre misalignment referred to the longitudinal orientation in the registered scan is reported as a dashed line. These misalignment values are computed considering only the extreme sections of the scan volume, and therefore assuming perfectly straight fibres: their median values amounts to respectively  $0.38^\circ$  and  $0.58^\circ$  for Tape A and Tape B, corresponding to a logarithm of differential tortuosity of -4.65 and -4.29.

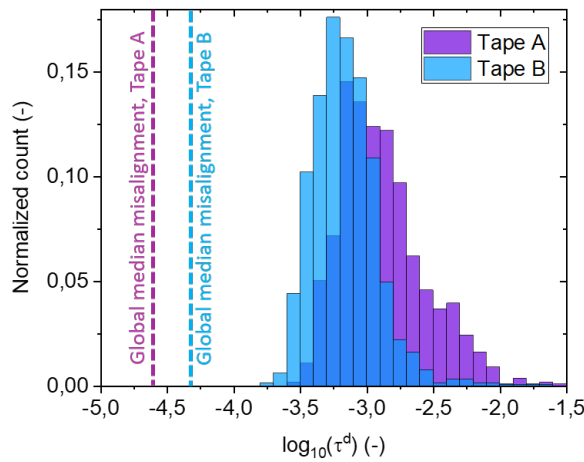


Figure 2.6: Histogram of the logarithm of differential tortuosity for the two tapes. The dashed lines represent the tortuosity related to the fibres global median misalignment.

Figures 2.7a) and 2.7b) represent the projection of all the individual fibre paths on a tape cross-section orthogonal to its axis, colour-coded according to the correspondent value of  $\tau^d$ . The parameter varies through the cross-section, with a tendency to higher values towards the tape edges. The differential tortuosity was evaluated in the thickness direction of the tape, corresponding to the  $y$  axis in Figures 2.7a) and 2.7b) to characterise this edge effect in greater detail. A bin scatter plot was used to help visualise the distribution of differential tortuosity according to the average  $y$  position of the fibres. The result is shown in Figures 2.7c) and 2.7d). The global median of the logarithm of  $\tau^d$  is shown by a vertical dashed line, while the local median for each horizontal bin is shown by a red square. The error bars represent the upper and lower quartiles. By comparison of the global median to the local median for each  $y$  value, different regions can be identified. Where the local median at a thickness value is higher (as in, more tortuous) than the global median, that region was classified as 'edge', while if lower, as 'core'. Tape A shows, in this case, a more symmetric edge effect of about  $30\ \mu\text{m}$  thickness on both sides, while Tape B shows a larger edge effect at the top (about  $80\ \mu\text{m}$ ) and a smaller edge region towards the bottom edge (15

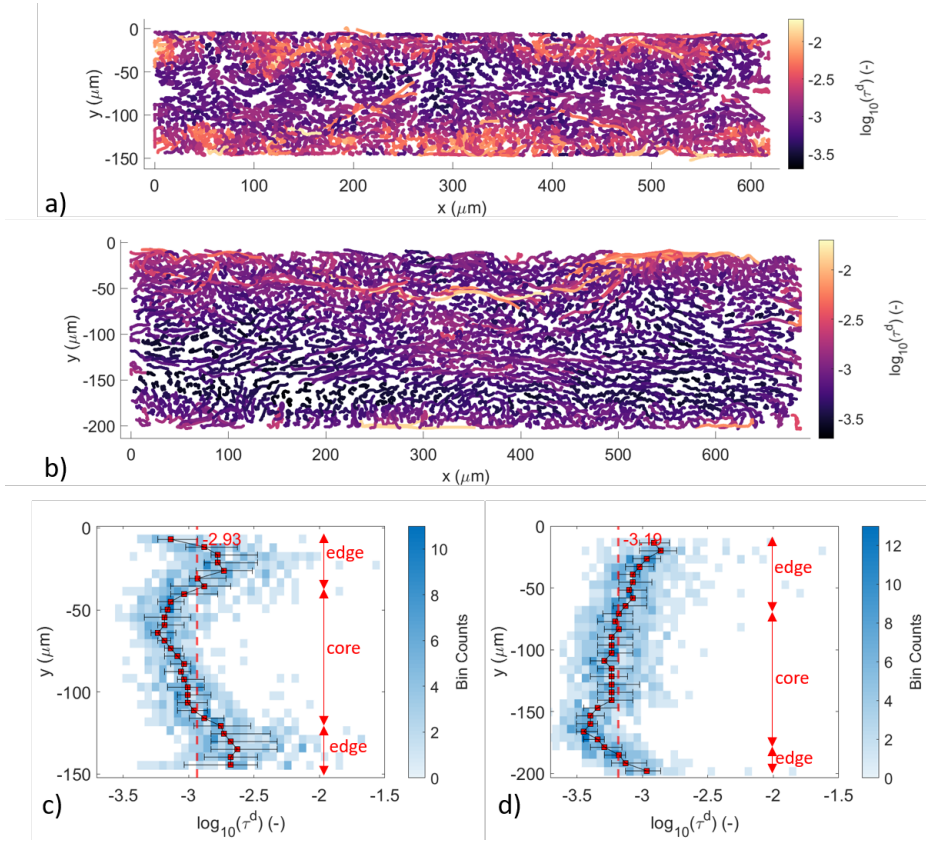


Figure 2.7: Projection of the fibre paths on a single cross-section orthogonal to the tape axis, colour - coded according to the logarithm of differential tortuosity ( $\tau^d$ ), for a) Tape A b) Tape B; bin scatter plot of the logarithm of differential tortuosity along the tape thickness for c) Tape A d) Tape B. The dashed line represents the median value of the logarithm of differential tortuosity calculated over the full cross-section, which value is noted at the top of each graph. For each horizontal bin, the local median is represented with red squares. The error bars represent the interquartile range.

$\mu\text{m}$ ).

### 2.4.2 COLLECTIVE MOTION

The contour plot of Figures 2.8a) and 2.8b) represent the median value of collective motion for each fibre, calculated fibre-by-fibre for the full length of ( $1450 \mu\text{m}$ ). The fibre configuration at the beginning of the measurement volume was used for the representation.

As explained in greater detail in Section 2.3.2, a value of 1 represents perfectly parallel motion in the same direction, 0 corresponds to random motion, and -1 to counter-streaming. The results show variations through the cross-section, with some regions displaying high levels of coherent motion above a value of  $CM = 0.8$ , depicted in a lighter colour.

The variation of CM along the tape thickness is shown in Figures 2.8c) and 2.8d). The

global median for the cross-section is shown as a dashed line, while the local median for each thickness level is shown by a red square, together with the interquartile range. Greater collective behaviour is observed at the centre of the tapes compared to the top and bottom edges, which resembles the same edge-core architecture observed for differential tortuosity in Figures 2.7c) and 2.7d). By comparison of the global and local median, a symmetric edge effect of about  $30\ \mu\text{m}$  is observed in Tape A. In Tape B, an edge effect at the top of about  $80\ \mu\text{m}$  and of about  $10\ \mu\text{m}$  at the bottom is observed.

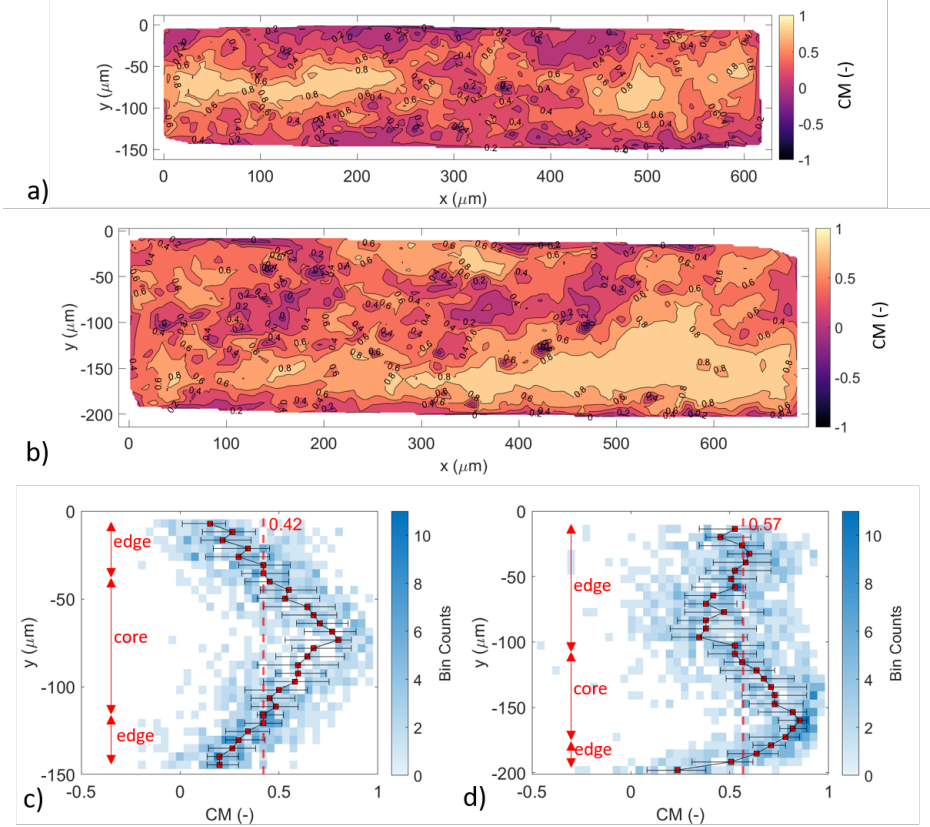


Figure 2.8: Contour plot of collective motion (CM) for a) Tape A, b) Tape B; thickness profile for c) Tape A, d) Tape B. The dashed line represents the median calculated over the full cross-section, which value is noted at the top of each graph. For each horizontal bin, the median of the distribution is represented with red squares. The error bars represent the upper and lower quartile.

### 2.4.3 LENGTH OF NEIGHBOURHOOD

The length of neighbourhood LON was defined as in Equation 2.5. The parameter corresponds to the median axial distance for which a contact is maintained.

Contour plots for showing the cross-sectional variability of LON can be found for Tape

A and Tape B, respectively in Figures 2.9a) and 2.9b). Bin scatter plots are used to represent the distribution of the parameters in relation to the tape thickness in Figures 2.9c) and 2.9d). The global median for the cross-section is shown as a dashed line, while the local median for each thickness level is shown by a red square, together with the interquartile range. A value of LON of  $1450\ \mu\text{m}$ , corresponding to the length of the full observation volume, indicates that a fibre maintains contact with the same neighbours through the entire axial length considered. The results show that LON is not constant through the cross-section, and that a variation through the tape thickness of LON is present. At the upper and lower tape edges, a lower length of neighbourhood is detected, similarly to the edge-core effect previously seen for differential tortuosity and collective motion. In this case, a symmetric edge effect of about  $25\ \mu\text{m}$  is observed in Tape A, while in Tape B, the top and bottom edges are respectively of about  $90\ \mu\text{m}$  and of about  $10\ \mu\text{m}$ .

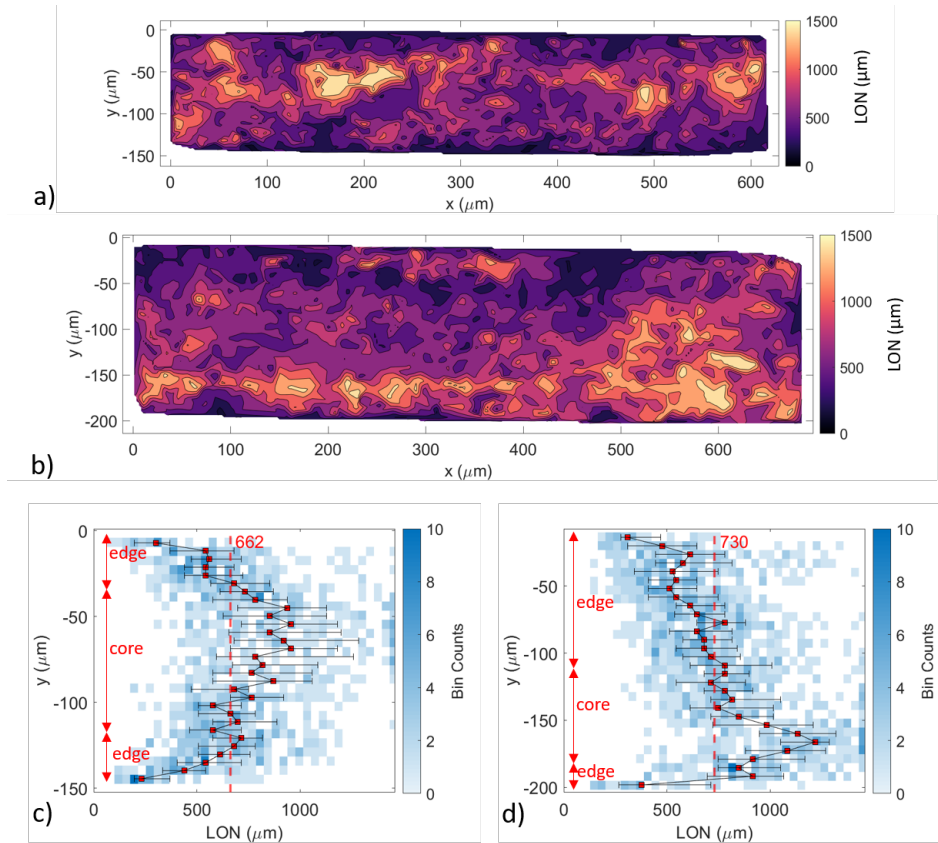


Figure 2.9: Contour plot of length of neighbourhood (LON) for a) Tape A, b) Tape B; thickness profile for c) Tape A, d) Tape B. The dashed line represents the median calculated over the full cross-section, which value is noted at the top of each graph. For each horizontal bin, the median of the distribution is represented with red squares. The error bars represent the interquartile range.



## 2.5 DISCUSSION

The results show that hierarchies in fibre organisation can be found in both samples analysed at all levels of observation. Similarly to the approach used by Song et al. in studying fibre arrangements in natural graded materials by looking at their thickness distribution [29], an edge-core effect can be observed for the three parameters. The approach might be leveraged to gain insight into the mechanisms of microstructural formation of tapes and composites.

### 2.5.1 DIFFERENTIAL TORTUOSITY

As shown in Figure 2.6, the tortuosity distribution is not related to the effect of global fibre misalignment, which is responsible for low tortuosity levels. The differences in tortuosity distribution observed in Figure 2.7 by comparing the two tapes might be related to the spreading configuration [52]. If mechanical spreader bars were used, typically both edges of the tape might encounter the spreader bars contact and friction, which is hypothesised to be the cause of the local increase of differential tortuosity  $\tau^d$ . Impregnation might also play a role in locally affecting the microstructure, with varying effects depending on the impregnation method used [53, 54].

The emergence of microstructural variability should be further investigated in relation to the control of the manufacturing parameters and to the tape geometry. By reducing the tape thickness, it is possible that the core region might gradually disappear, and the high tortuosity edge effect would prevail through the entire cross-section. This would be of particular importance in the study of thin ply composites [2].

### 2.5.2 COLLECTIVE MOTION

Values of collective motion close to 1 suggest the existence of fibre bundles areas with a degree of organisation within the tapes analysed, which was not observed before. Note that in Figure 2.8, only a few areas show counter-streaming, indicating it is not prevalent.

The collective motion CM defined here is capable to only capture synchronised displacement. It is however possible that high tortuosity fibres might undergo other types of collective motion patterns which could be related, for example, to local bundle rotation, which is here not quantified. Further studies should extend the current methodology for a greater understanding of the tape spatial organisation.

### 2.5.3 LENGTH OF NEIGHBOURHOOD

In a network composed of perfectly straight and parallel fibres, the length of neighbourhood LON should always be equal to the length of the scan volume since their neighbours will not change through space. Conversely, as shown in Figure 2.9, the global median of LON has a value of respectively 662  $\mu\text{m}$  and 731  $\mu\text{m}$  for Tape A and Tape B, which corresponds to about half of the length of observation  $L_o$ . This means that two fibres will generally remain in close contact for about 700  $\mu\text{m}$  before moving to different neighbourhoods.

In both tapes, fibres that have not yet changed neighbourhood can be identified in the bin scatter by points located at  $\text{LON} = L_o$ , in this case equal to 1450  $\mu\text{m}$ . Such fibres have been defined as 'invariant fibres' in the work of Fast et al., since their neighbourhood does not vary [26]. This is however a feature related to the size of the scan volume. Such fibres



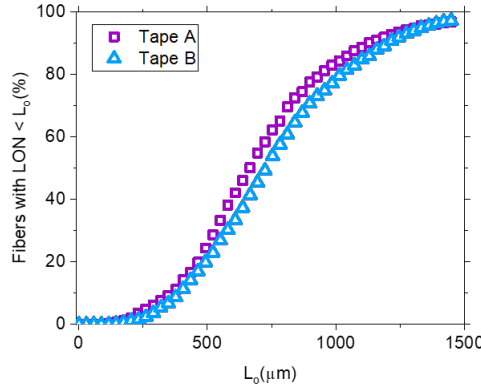


Figure 2.10: Fraction of fibres with a length of neighbourhood LON lower than the volume scan size  $L_o$ , for varying  $L_o$ .

might change neighbours later on along the tape, and a larger length of observation is required to confirm this.

This concept was further explored by artificially varying the length of the scan volume  $L_o$ , from a value of 0 to the value of the total length of observation of  $1450 \mu\text{m}$ . Figure 2.10 shows the variation in the percentage of fibres having  $\text{LON} < L_o$  which therefore have exchanged neighbours at least once in the volume, as a function of  $L_o$ . For a very small  $L_o$ , the microstructure resembles an ideal unidirectional composite, with most fibres remaining in the same neighbourhood through the entire length of observation. An increasingly long scan volume is able to start capturing the deviations from the ideal model, capturing the variability in LON within the material.

Eventually, all fibres are expected to have exchanged neighbours at least once. According to Figure 2.10, this seems to occur earlier in Tape A compared to Tape B, which can be observed by a shift of the curve towards lower  $L_o$  values. This aligns with the ordering of the global median values shown in Figure 2.9 and might reflect a greater extent of neighbourhood variation related to its overall greater differential tortuosity. For the maximum scan volume observed of  $1450 \mu\text{m}$ , both tapes reach a value of about 97% of fibres which satisfy the condition of  $\text{LON} < L_o$ , indicating that such scan length is sufficient for the given materials to extract the full LON distribution. We therefore expect that a further increase of the scan volume would not significantly change the trends shown for this parameter.

Such scan volume size might represent a characteristic length of fibre association, describing the level of interconnectivity within the material. By capturing the periodicity of the fibre association, this approach might guide future work in defining the axial dimension of representative volume elements (RVE) for more accurate modelling of unidirectional composites [55, 56].

### 2.5.4 INTERRELATION OF PARAMETERS

By further studying the parameter interrelation, more information can be gathered on the architecture of the material. Due to the similar edge-core effect and edge-core thickness observed for both differential tortuosity and collective motion, the relationship between the two parameters was further investigated.

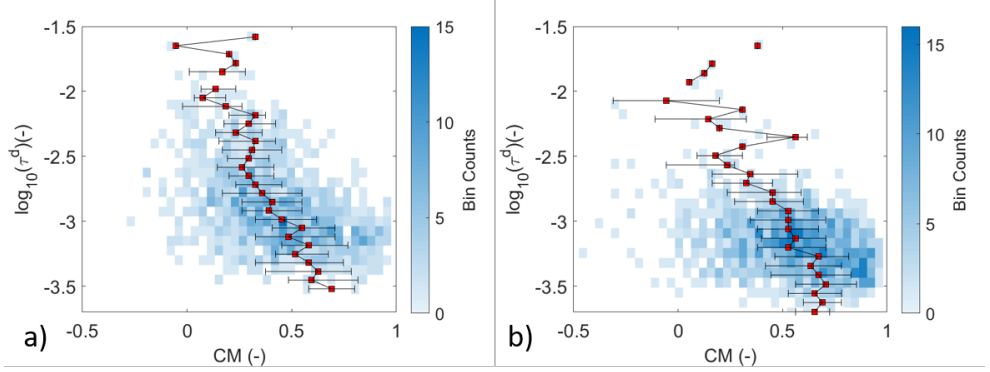


Figure 2.11: Collective motion CM against logarithm of differential tortuosity  $\tau^d$  for a) Tape A, and b) Tape B. For each horizontal bin, the median of the distribution is represented with red squares. The error bars represent the quartile interval.

Figures 2.11a) and 2.11b) show a bin scatter plot comparing  $\tau^d$  and CM. For the two tape portions analysed, there is a tendency for regions of lower differential tortuosity to move with greater coherence. Conversely, fibres that show high differential tortuosity show a lower tendency to coherent motion, which might translate into the presence of lone fibres moving independently from their surroundings, as the 'stray fibres' observed in literature at the free surface of UDCs [24]. Such an approach has the potential to identify different regimes in the fibre organisation in a material, which should be related to the manufacturing or processing methods.

LON was analysed in relation to the logarithm of  $\tau^d$  and CM, as shown in Figure 2.12. In both tapes, fibres that have a lower length of neighbourhood tend to move less collectively and have higher differential tortuosity. Conversely, a higher LON is associated with a higher tendency to collective behaviour and lower differential tortuosity. This agrees with the observation that at lower differential tortuosity, fibres might tend to have greater alignment and remain close to their original neighbourhood. It also seems to indicate that a more coherent fibre association and movement through the volume might be associated with a higher length of neighbourhood and lower tortuosity.

The quantification of these descriptors might find application both in tape manufacturing, and in the study of microstructural evolution during composite part formation. Microstructural variability can affect deconsolidation [15], consolidation [57] or microstructural conditioning [4]. Ultimately, the proposed methods might contribute towards the development of tailored microstructures for specific applications.

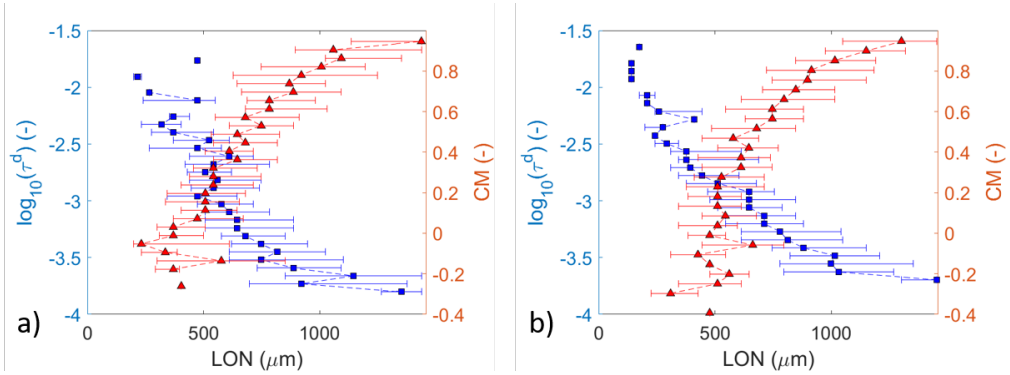


Figure 2.12: Length of neighbourhood as a function of differential tortuosity and collective motion for a) Tape A, and b) Tape B. The blue squares correspond to the median logarithm of differential tortuosity (left axis), while the red triangles correspond to the median collective motion (right axis). The error bars represent the interquartile range.

## 2.6 CONCLUSION

Understanding the three-dimensional variability of unidirectional composites is relevant for the development of advanced material modelling strategies. In this work, a novel methodology was developed for the characterisation of continuous unidirectional composites. 3D microstructural descriptors were introduced, covering trajectory analysis (differential tortuosity), group behaviour (collective motion), and network connectivity (length of neighbourhood), each representing an increasing level of complexity in the fibre architecture. These key descriptors were showcased on real material datasets from two different CF/PEEK tapes. 3D scan volumes were acquired via X-ray computed tomography, and a facile method for image analysis was used to reconstruct the 3D fibrous architecture at a single fibre path resolution.

Single fibre trajectories are described by a novel definition called differential tortuosity, which highlights the deviation of the fibre trajectory from a straight longitudinal path. The group behaviour analysis is conducted by the collective motion concept, inspired by animal locomotion, that can detect synchronous fibre bundle motion. The fibre network connectivity was evaluated by a length of neighbour contact definition that relies on the axial distance in which fibres remain in the same Voronoi neighbourhood. It was shown that these proposed descriptors enable to highlight micro- and mesoscopic features. Key observations based on these material sets are as follows. Similar through-thickness gradients, in the form of edge-core effects, were observed for all three parameters. The study of parameter interdependence was able to further describe the architectural arrangement at a single fibre resolution. For both tapes analysed, fibres with higher differential tortuosity, therefore greater deviations from the ideal longitudinal direction, show both a lower tendency to move collectively and a lower length of neighbourhood, indicating a more independent movement from their neighbourhood. Conversely, a higher length of neighbourhood is associated with a higher tendency to collective behaviour and lower differential tortuosity.

Another interesting observation is related to the effect of scanned tape length on the evolution of the length of neighbourhood (LON). The maximum value of LON is bound to the size of the scanned volume. By increasing the axial size of the scan volume, the change of fibre contacts can be increasingly sampled. Given a long enough volume, all fibres will have changed neighbours at least once. For the tapes analysed, the axial size for which this happens was found to be  $1450\text{ }\mu\text{m}$ . Such volume size constitutes a characteristic length for a unidirectional material and relates to its level of fibre interconnectivity. This provides both insight on the network arrangement and a guideline for future work in the definition of representative scan volumes.

The work contributes to bridging a gap in the classical approach and nomenclature typical of the composite field to describe and quantify complex architectural organization, by successfully employing strategies inspired by other research domains. The novel parameters introduced enable new routes for the description and quantification of complex fibre arrangements. This methodology for the analysis of UDCs might allow distinguishing different regimes of fibre organisation in similar fibre-resin systems and might also be applicable in general to the description of the architecture of fibrous material.

The parameters shown here and their interdependence will provide further insight into micro- and mesoscopic effects related to microstructure formation of UDCs. Future work will study the influence on the microstructure of the choice of manufacturing parameters, such as fibre spreading and impregnation, and the propagation of the architectural features at various lengthscales. Microstructural evolution during processing or loading could also be studied with this approach. The understanding of the scale of organisation in a material, as through the length of neighbourhood, might provide input for advanced modelling techniques such as RVEs.

## 3

## 3

## CHARACTERISING PORE NETWORKS AND THEIR INTERRELATION WITH THE FIBRE ARCHITECTURE IN UNIDIRECTIONAL COMPOSITES

*This work proposes a methodology for the characterisation of complex pore features in unidirectional composite preregs, and provides insights into the interaction between fibre architecture and pores. The method showcased allows to compare spatial distributions at a three-dimensional level, highlighting in the tape analysed a significant correspondence between regions of elevated tortuosity and increased pore fractions. Regions associated with highly tortuous meandering fibres exhibit a pronounced association with porosity located both in the bulk and at the tape surface, suggesting a strong interaction between non-collective fibre displacement and the probability of pore location. Furthermore, our study quantifies the length scale of feature propagation, shedding light on the spatial extent of microstructural pore occurrence within the composite. These findings have significant implications from a characterisation perspective to aid modelling approaches and manufacturing processes for high-performance composite preregs tapes.*

### 3.1 INTRODUCTION

Unidirectional thermoplastic composites are materials with complex microstructural features. Recent studies revealed that microstructural analysis can be used to establish the relationship between the manufacturing parameters and the microstructural features [59]. The first step in this direction is the development of methodologies that allow the identification of relevant features and evaluate their interrelations in various scales. With this goal in mind, the authors have previously introduced in **Chapter 2** novel metrics to characterise fibre architectures in unidirectional thermoplastic composite preregs, which address fibre tortuosity, collective fibre bundling effects and fibre network interconnectivity [41].

Porosity is strongly related to material processing, mechanical performance, and quality assessment of composites. Recent studies emphasise the importance of understanding the spatial characteristics of surface evolution and porosity in tapes, particularly with respect to defect analysis and the development of intimate contact [57]. Pore evolution is also relevant to the study of deconsolidation and consolidation phenomena during material processing [15, 60]. Interestingly, pores, conventionally considered defects, can be deliberately designed within thermoplastic preregs to create pathways for easier through-thickness or in-plane air removal, influencing material design and optimisation [39].

The spatial morphology of the reinforcement was found to affect permeation in thermoplastic composites through-thickness impregnation [53]. Additional studies propose qualitative observation of a possible link between pore locations and fibre tortuosity at a single fibre resolution in unidirectional composite tapes [61] and misalignment derived from structure tensor analysis in unidirectional consolidated laminates [38]. The pore distribution may therefore not be randomised, but rather linked to other microstructural features. The quantification of the link between pores occurrence and fibre architecture characteristics should be further investigated.

Microstructural information of unidirectional composites can be successfully obtained by X-ray Computed Tomography techniques, which can allow to obtain three-dimensional (3D) insights into the pore morphology and distribution in composite laminates [60, 62, 63]. While recent work leveraging Computed Tomography-based techniques was able to highlight the in-situ mechanical response of composites in relation to kink band formation under compression in the presence of defects [38], a clearer understanding of the different scales of organisational features is required.

The goal of this Chapter is to understand the interrelation of different microstructural features at the fibre and pore levels in unidirectional composite preregs, by developing an analysis methodology for 3D X-ray micro-computed tomography data at a single fibre resolution. A development-grade material with a thermoplastic matrix with complex manufacturing-induced pore morphologies was used. The investigation leads to the quantification of local microstructural phenomena linking tortuosity and the spatial propagation of porosity. This study aims to better understand the microstructural characteristics in unidirectional thermoplastic composites, with implications for manufacturing processes and material properties.

## 3.2 METHODOLOGY

This section describes the methodology followed for analysing 3D datasets of a unidirectional carbon fibre-reinforced composite prepreg. The data was obtained via X-ray microcomputed tomography and it was post-processed to extract information regarding the distribution of fibres and porosity.

### 3.2.1 MATERIAL

The unidirectional tape used is a development grade of Toray Cetex® TC1225 and was manufactured by Toray Advanced Composites. The tape used has standard modulus carbon fibre reinforcement and thermoplastic matrix. The material is the same used in previous conference work by Gomasasca et al. [61]. A portion of the tape of about 2.5 mm in width measured orthogonal to the main fibre direction, and 10 mm along the main fibre direction was cut and used for microstructural analysis.

### 3.2.2 TOMOGRAPHIC IMAGE COLLECTION

The data was acquired via X-ray micro-computed tomography (XCT) with a Zeiss Xradia 520 Versa at Naturalis Biodiversity Center, Leiden. 3D volume acquisition was obtained with a 2000x2000 pixel detector in binning mode 1, 4x magnification lens, voltage of 70 kV, power of 5 W and an exposure time of 7 s. Compared to **Chapter 2**, where a binning mode 2 was used, binning mode 1 allows to increase the field of view of the measurement, while sacrificing image quality. A schematic of the sample configuration during the measurement is provided in Figure 3.1. The sample was mounted with the fibre principal alignment direction oriented vertically, and a detector-sample distance of 40 mm. The volume reconstruction was conducted with the software Scout-and-Scan™Control System Reconstructor (Zeiss) as a standard reconstruction. The settings led to a voxel size of 0.7788  $\mu\text{m}$ . The dataset is available at reference [64]. Three scan volumes have been stitched in the fibre length direction with an overlap of 21%, for a total scan volume length of about 3500  $\mu\text{m}$ . Of that volume, a scan length of 3000  $\mu\text{m}$  was selected for the analysis.

### 3.2.3 SEGMENTATION OF FEATURES OF INTEREST

The data was first reduced to 8 bits in Fiji [44] via linear scaling to reduce the computational cost, and then manually registered. This led to a volume used for the analysis measuring 1200  $\mu\text{m}$  in the tape width (transversal to the fibre direction), 160  $\mu\text{m}$  along the tape thickness and 3000  $\mu\text{m}$  in the tape length (parallel to the main fibre direction).

To assess the spatial propagation of the features of interest, the total scan volume was split into six sub-volumes 500  $\mu\text{m}$  long along the principal fibre alignment direction  $z$ . Representative cross-sections for Sub-Volume 1 are shown in Figure 3.2. The tape orientation shown in Figure 3.2, and the definition of a top and a bottom surface, do not relate to the tape orientation during manufacturing. The subdivision of the tape into individual sub-volumes allows the neglect of long-range variations in tape profile due to bending and rotation. The  $z$  direction was chosen as it is expected that unidirectional composites will present features that will be preferentially retained along that axis. All the analyses conducted, unless highlighted explicitly in the text, were performed based on the distinction between sub-volumes.

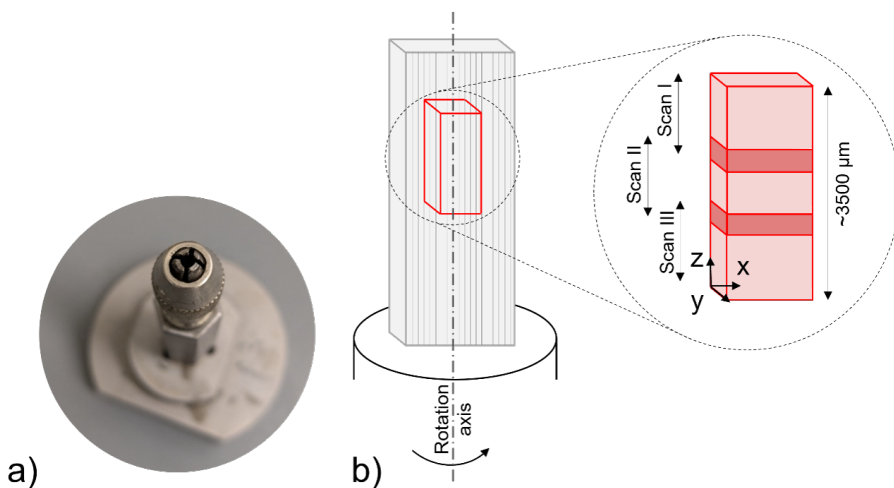


Figure 3.1: a) Detail of the sample holder used; b) schematic of the sample mounting for the XCT measurement, and of the scanned region of interest. The z axis corresponds to the fibre principal alignment direction in the sample.

The objective of the segmentation step is to distinguish fibres and porosity. Fibre and pore space segmentation was performed in Fiji using the Weka Trainable Segmentation (Weka) plugin [46], which is a trainable machine learning tool that performs pixel-based segmentation. Segmentation was performed generating two distinct classifiers: one to identify fibres and one for recognising porosity and air surrounding the tape. A training set based on ten equidistant  $xy$  cross-sections extracted from the total scan volume of 3000  $\mu\text{m}$  was used.

The obtained segmented images related to porosity were further processed via morphological operation of 3D opening with a 3D ball element of 1 voxel radius in Fiji to reduce noise in the segmentation.

Following the distinction between fibres, porosity and air surrounding the tape for each sub-volume, the following approach was implemented. First, close (internal) and open porosity regions are distinguished, and a global boundary for the tape at each sub-volume location was determined to identify open pore areas which pertain to the tape region, defined as surface pores. Secondly, the segmented fibres are converted into fibre path trajectories to further quantify the parameters of interest.

#### INTERNAL AND SURFACE POROSITY

A 3D connected region analysis was conducted on the pore space in Matlab with the functions 'bwconncomp' and 'regionprops' to identify individual pores for further quantification. A 26-connectivity criterion was used for each voxel, which considers both faces, edges, and corners to touch in defining connected components.

Two categories of porosity can be distinguished. Internal (close) pores were defined as 3D regions entirely embedded in the tape. Complex open pore networks of non-impregnated



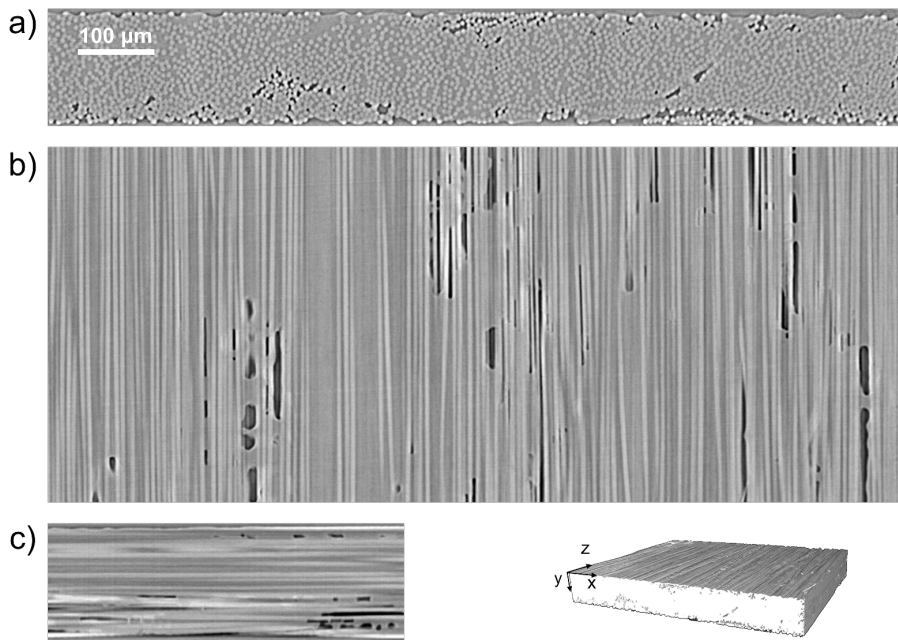


Figure 3.2: Cross-sections derived from X-ray microcomputed tomography data for Sub-Volume 1, with reference to the planes a)  $xy$ ; b)  $xz$ ; c)  $yz$ .

areas are also observed, which communicate with the air surrounding the tape. The surface porosity of pertinence to the tape was identified via the definition of a tape boundary for each sub-volume.

A schematic of the workflow conducted in Matlab for the tape boundary determination per sub-volume is shown in Figure 3.3a)-c), in reference to the  $xy$  cross-sectional plane. The segmented tape profile for each  $xy$  cross-section within the individual sub-volume was first considered as in Figure 3.3a), where open pore regions are shown in black, and regions occupied by the tape are shown in white. To determine the tape boundary in each sub-volume, the fraction of voxels occupied by the tape for each location on the  $xy$  plane have been considered, as shown in Figure 3.3b). Voxels highlighted in yellow indicate certainty of belonging to a tape area throughout the entire sub-volume, while the ones shown in blue belong to open pore regions. A threshold of 0.07 was used to binarise the normalised count map, to exclude regions with a very low probability of locating inside the tape area, and subsequently processed via a morphological operation of opening with a circular element of 3 voxels size as a noise removal step. The contour of the region identified was defined as boundary of the sub-volume and identified via the Matlab function 'bwtraceboundary'. The defined boundary represents the mesoscopic variability of the tape in each sub-volume. For each sub-volume, the connected pore regions in correspondence of the top and bottom surface touching the boundary were defined as surface pores, which are shown in cyan in Figure 3.3c).

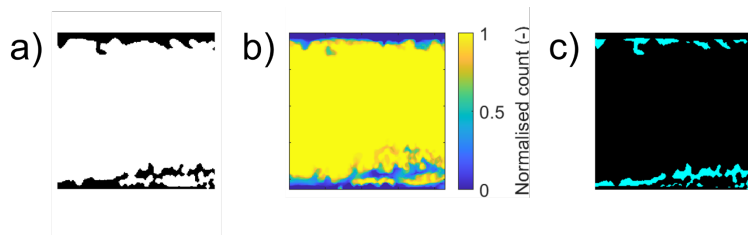


Figure 3.3: Workflow for boundary extraction for Sub-volume 1: a) segmented view where the regions showing open pores (black) and tape (white); b) normalised count of voxels showing the likelihood a voxel to locate inside the tape area; c) resulting surface porosity after boundary definition, shown in cyan.

3

### FIBRE PATH RECONSTRUCTION

Within the tape boundary for each sub-volume, the segmented cross-sections on the  $xy$  plane were averaged in groups of five to obtain a distance between data-reduced slices of about  $3.9 \mu\text{m}$ . This inter-slice distance in the data reduction was halved compared to the choice made in **Chapter 2** to help compensate for the reduction in the 3D image quality due to the different binning setting. The resulting image stack was then analysed with Trackmate, a plugin available in Fiji that allows one to identify and track circular objects moving in 3D space, or time [47]. A detector employing a Laplacian of Gaussian filter and a reference fibre diameter of  $6 \mu\text{m}$  was applied to identify the fibre centres. The selected tracker for fibre reconstruction was based on the Simple Linear Assignment Problem [47], with a maximum linking distance between fibre centres of  $5 \mu\text{m}$ , an in-plane maximum gap-closing distance of  $5 \mu\text{m}$  and a gap-closing distance along the main fibre alignment direction of 45 data-reduced  $xy$  cross-sections (corresponding to an axial length of  $225 \mu\text{m}$ ). The different settings compared to **Chapter 2** were chosen to aid in connecting fibre centres in a lower image quality volume, where otherwise more fragmented fibre information would have been retrieved. The gap-closing distance chosen is meant to facilitate fibre trajectory reconstruction in the presence of segmentation artefacts that might otherwise result in a partial portion of fibres not being recognised as one single entity. Detected fibres longer than  $60 \mu\text{m}$  were further analysed. While the fibres studied are in principle long and continuous, the threshold allows to include in the analysis partially captured fibres at the left and right sides of the tape moving in and out of the scan volume, fibres that might have a broken end, as well as portions of long fibres misinterpreted as separate fibre segments.

The fibre trajectories so obtained were further processed in Matlab. Non-defined values in the fibre trajectories have been reconstructed via the linear interpolation function 'fillmissing'. The fibre paths were then smoothed via local regression using weighted linear least squares and a  $2^{\text{nd}}$  degree polynomial model with an interpolation length of  $39 \mu\text{m}$ .

### 3.3 QUANTIFICATION OF METRICS FOR THE MATERIAL DESCRIPTION

#### 3.3.1 DESCRIPTION OF PORE FEATURES

For each sub-volume, the variability in the distribution of porosity was first assessed by the local pore fraction  $P_f$ , determined on a voxel basis for the three projection planes  $xy$ ,  $zy$  and  $xz$  as the fraction of voxels occupied by pores at each cross-sectional location.

The geometrical characteristics of individual internal and surface pores were then quantified via ellipsoid approximation based on their principal semi-axes. The metrics proposed in the work of Mehdikhani et al. [62] were used for comparison, namely Roundness (R), Geometrical Mean (GM) and Elongation (E):

$$R = \frac{c}{b} \quad (3.1)$$

$$GM = (cb)^{1/2} \quad (3.2)$$

$$E = \frac{a}{GM} \quad (3.3)$$

where  $a, b$ , and  $c$  are the semi-major, semi-medior and semi-minor axes of the approximated ellipsee. Pores with a volume greater than 1 voxel were considered for this analysis.

#### 3.3.2 FIBRE DIFFERENTIAL TORTUOSITY

The differential tortuosity of fibres was defined as in Chapter 2 [41, 61]:

$$\tau^d = \frac{L}{L_0} - 1 \quad (3.4)$$

Where  $L$  is the fibre length, and  $L_0$  is the length of the scan space in the principal fibre alignment direction over which  $L$  is evaluated. The parameter represents the trajectory deviation of a fibre from a perfectly straight path in the principal alignment direction. A fibre perfectly aligned to the main fibre direction will have a tortuosity of zero. The more alignment is lost in the fibre, or the more the angular deviation from the alignment direction is, the more tortuosity will increase. The logarithm of tortuosity will be considered in the analysis.

Differently from Chapter 2 where differential tortuosity was calculated over the entire scan length, in this Chapter the parameter was determined on a sliding window aligned with the principal fibre alignment direction  $z$  of  $L_0 = 43 \mu\text{m}$ , equivalent to approximately 6-7 times the fibre diameter. The value was considered small enough to retain local properties, while allowing for an extent of local homogenisation and noise removal. A schematic of the calculation is shown in Figure 3.4. The window of calculation moves along each fibre trajectory to account for varying fibre length and to obtain a 3D distribution of the parameter.

#### 3.3.3 DATA REDUCTION OF PORE REGIONS AND DIFFERENTIAL TORTUOSITY FOR FEATURE CORRELATION

In the sample studied, pores tend to locate in-between fibres as qualitatively visible in Figure 3.2. Local tortuous behaviour might influence pore locations, and possibly create far-field

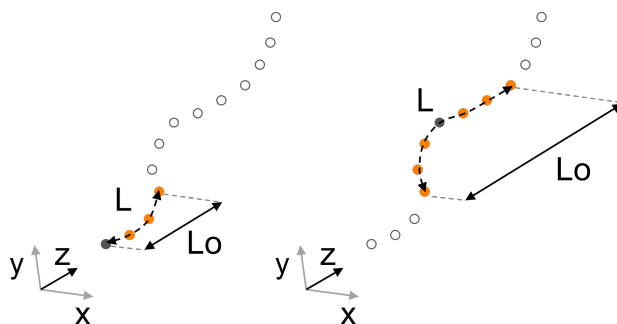


Figure 3.4: Schematic for the calculation of differential tortuosity: represented on the left is the edge of the fibre, on the right at the centre of the fibre. In black is shown the point of calculation of local tortuosity, and in orange the window of calculation over the distance  $L_o$  aligned to the principal alignment direction  $z$ .  $L$  is the length measured along the fibre trajectory.

effects. To study possible correlation of tortuosity and pore locations, the following method was developed. A max-filter was applied both on the binarised segmented pore volume and on the linearly interpolated differential tortuosity values as an image processing step to consider a translation tolerance for the compared features. Subsequently, differential tortuosity was compared at a voxel level to pore-free, internal, and surface porosity regions.

An example of image processing induced by the max-filter operation is shown in Figure 3.5 for the case of the porosity distribution. The max-filter works through a moving kernel, over which only the maximum value is retained. In this work, a cubic kernel of 15 voxels on each side (equivalent to  $11.7 \mu\text{m}$ , about 1.5 times the fibre diameter) was used as a moving window across the volume, with a stride of 15 voxels and no padding. A sensitivity analysis on the effect of the kernel size can be found in Appendix G.



Figure 3.5: a) Segmented porosity cross-section on the  $xy$  plane, where pores are highlighted in white; b) same cross-section after max-filtering with a cubic element of 15 voxels side, corresponding to approximately 1.5 times the fibre diameter.

### 3.3.4 DETERMINATION OF CHARACTERISTIC LENGTHSCALES OF DIFFERENTIAL TORTUOSITY AND PORE REGIONS

The propagation of porosity and differential tortuosity along the volume studied was assessed via the determination of their characteristic lengthscales based on spatial similarities of  $xy$  cross-sections of the max-filtered parameters. The use of spatial similarity analysis was used in the study of tow-based discontinuous composites via cross-correlation equations to extract information on the characteristic lengthscale of strain fields [65] and in unidirectional composites to study fibre misalignment in microscopy images [66]. Alternative ways for detecting similarity in arrays are Sum of Square Differences [67], Sum of Absolute Differences [68], and Euclidean Distance [69], which are conceptually similar approaches that can be applied to observe parameter variations at a voxel level. In this work, feature similarity analysis was conducted on binarised volumes by considering a normalised Sum of Absolute Differences (nSD) formulation:

$$nSD(z_i, z_j) = \frac{1}{N_{ij}} \sum_{k=1}^{N_{ij}} |(A_i)_k - (A_j)_k| \quad (3.5)$$

where  $z$  is the principal fibre alignment direction,  $A_i$  and  $A_j$  are two binarised cross-sections at locations  $i$  and  $j$  along  $z$  and  $N_{ij}$  is the combined number of voxel locations related to the feature observed for the two cross-sections (for the pore network, the pore voxel locations; for the tortuosity distribution, the voxels with value greater than the median). In the case of a binarised volume, the range of nSD goes from 0, indicating no change in the voxel values between the two slices, to 1, indicating a change in all voxels considered. A schematic of the calculation applied on a simplified case study is reported in Figure 3.6.

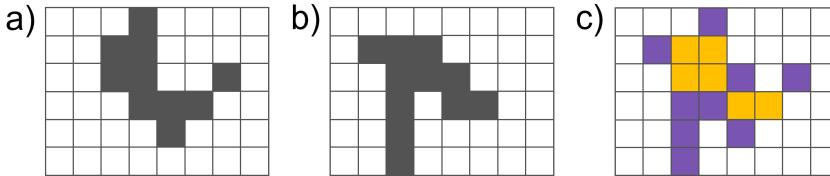


Figure 3.6: Simplified example of the application of the similarity method a) slice  $A_i$ , pore voxels highlighted in grey; b) slice  $A_j$ , pore voxels highlighted in grey; c) resulting map of nSD values for the global pore voxels in the two slices, counting a global number of pore locations  $N_{ij} = 15$ . The intersection of the pore regions are highlighted in orange (6 voxels), while the regions not overlapping are shown in purple (9 voxels), resulting in a value of  $nSD = 9/15 = 0.6$ .

## 3.4 RESULTS AND DISCUSSION

### 3.4.1 POROSITY

#### QUANTIFICATION OF CROSS-SECTIONAL PORE CLUSTERING

Figure 3.7a1), a2) and a3) show the porosity fraction  $P_f$  determined for each voxel location on the projection planes  $xy$ ,  $xz$  and  $yz$  for Sub-volume 1. The maps corresponding to all sub-volumes can be found in Appendix A.

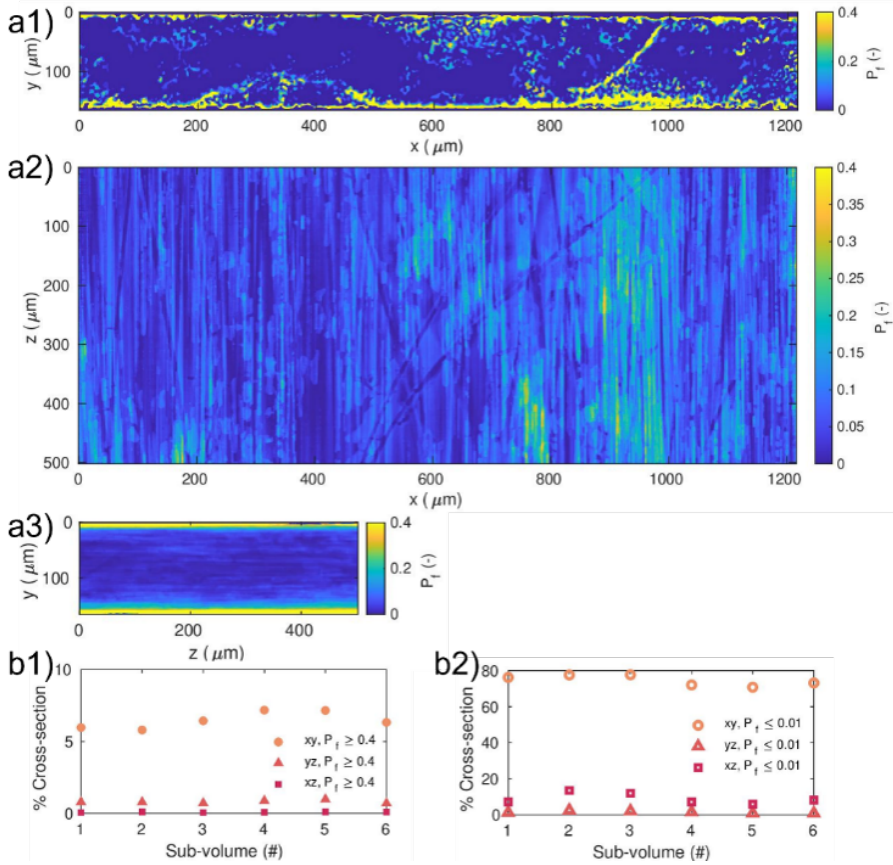


Figure 3.7: For Sub-volume 1, pore fraction ( $P_f$ ) maps for the three projection planes a1)  $xy$ , a2)  $xz$  and a3)  $yz$ ; for all sub-volumes and the three projection planes, fraction of cross-section occupied by b1) high pore fraction ( $P_f \geq 0.4$ ) and b2) low pore fraction ( $P_f \leq 0.01$ )

The pore fraction maps highlight that pores are not distributed homogeneously in the three projection planes considered for each sub-volume. On the  $xy$  plane high pore fraction regions tend to appear at discrete cross-sectional locations. The  $yz$  plane shows an edge-core effect in the distribution of the porosity fraction, with a higher pore fraction on the top and bottom surfaces of the tape. On the  $xz$  plane, the porosity fraction appears more homogeneously distributed.

Based on the pore fraction distributions on the three reference planes  $xy$ ,  $yz$  and  $xz$ , the extent of pore clustering on each of the three planes have been evaluated. Pore clustering indicates the extent to which pores are located in a limited (clustered) region on a reference plane or whether they are more homogeneously distributed. To quantify this characteristic, the fraction of the reference plane occupied by regions of high-pore fraction with  $P_f \geq 0.4$  (meaning that pores occupy more than 40 % of the voxels at those cross-sectional locations),

and by low pore fraction regions with  $P_f \leq 0.01$  (corresponding to less than 1 % pores), were evaluated. The results are shown respectively in Figure 3.7b1) and Figure 3.7b2). The  $xy$  plane shows both the highest percentage of high- $P_f$  regions, up to 7 % compared to less than 1 % for the  $yz$  and  $xz$  planes, and the highest percentage to low- $P_f$  regions, up to 80 % compared to less than 20 % for the  $yz$  and  $xz$  planes. Clustering of high  $P_f$  regions on the  $xy$  plane, compared to  $yz$  and  $xz$ , suggests a preferential global orientation of the pore network with the main fibre direction  $z$  and a greater spatial variability of the porosity distribution across the tape width. The results were consistent for all sub-volumes, supporting the choice of  $z$  as the direction of feature propagation in Section 3.3.4.

### GEOMETRICAL ANALYSIS OF INTERNAL AND SURFACE PORES

A 3D view highlighting the different cross-sectional distributions of internal and surface pores for Sub-volume 1 is shown in Figure 3.8a). The through-thickness edge-core distribution of the pore fraction shown in the previous section in Figure 3.7a3) was observed in more detail in Figure 3.8b), where each line for each pore class refers to a different sub-volume. Consistently for each sub-volume, a higher pore fraction was found on the bottom side of the tape according to the chosen reference orientation, and it can be mainly attributed to surface pores. Internal porosity appears less pronounced but shares the tendency to an edge-core effect, which overlaps with the through-thickness locations of surface pores. Figure 3.8c) highlights that the depth affected by surface porosity can exceed half the thickness of the tape, which in this example is about  $150 \mu\text{m}$ . However, no connected pore paths were found between the top and the bottom surfaces.

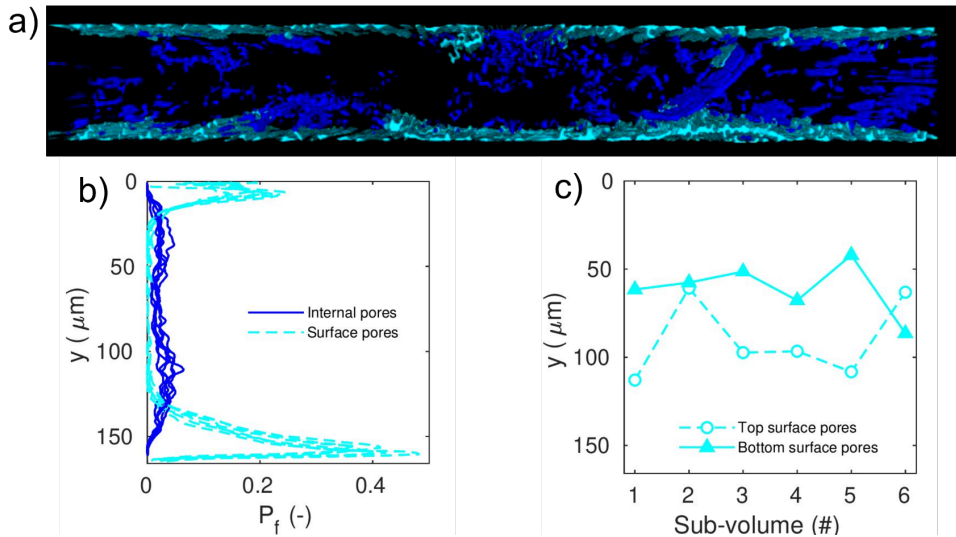


Figure 3.8: Distinction between internal and surface pores a) 3D representation for Sub-volume 1 of internal pores (in cyan) and surface pores (blue); b) through-thickness pore fraction  $P_f$ ; c) coordinate of the maximum inner edge of the top and bottom surface pores.



The morphology of internal and surface pores was analysed based on ellipsoid approximation in Figure 3.9, which shows the aggregated results from the entire scan volume, in this case without considering the artificial boundaries created by the subdivision in distinct sub-volumes. The three parameters considered are compared to the pore volume  $V_p$ , shown on the horizontal axis, which is measured based on pore voxels, and each pore is shown as a single datapoint. Roundness decreases from a value of 1 (perfectly circular cross-section) towards a value of zero (flattened cross-section) with increasing pore volume  $V_p$  for both internal and surface pores, as seen in Figure 3.9a). Surface pores tend to be flatter at the same volume than internal pores. The Geometrical Mean of the two smaller semi-axis shown in Figure 3.9b), which indicates the size of the pore cross-section, increases with  $V_p$ . A similar parameter trend is found for internal and external pores in log-log scale, but with a larger range for surface pores. Elongation, which relates the major semi-axis to the Geometrical Mean, also increases with  $V_p$ , at a higher rate for surface pores than for internal pores, as shown in Figure 3.9. The result indicates the general tendency of larger pores to have a higher aspect ratio between their length and cross-sectional dimension. Additional information on the statistics of internal and surface pores can be found in Appendix B.

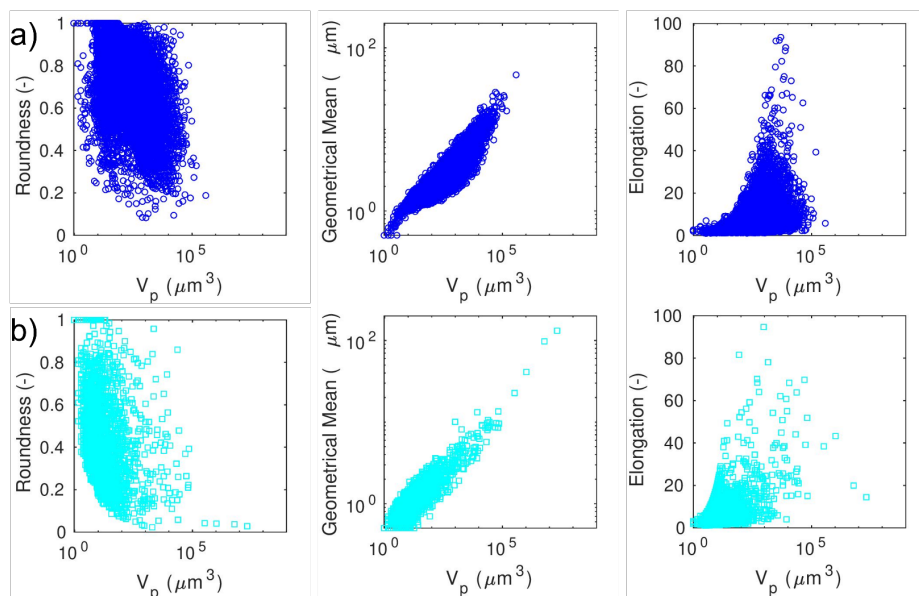


Figure 3.9: Geometrical characteristic of pores as a function of pore volume ( $V_p$ ) for the full scan, for a) internal pores; b) surface pores. Pore volume and Geometrical mean are expressed in logarithmic scale.

### IMPLICATIONS ON TAPE MANUFACTURING PROCESSES

The methodology here developed for the porosity description in freestanding unidirectional composite tapes allowed to highlight features of relevance for tape manufacturing control. The tape boundary definition used to identify surface porosity enabled the identification



of both surface pores affecting the inner tape portions and surface pores more strongly related to the surface topology of the tape. The boundary definition for each sub-volume highlighted an overall straight geometry of the top and bottom tape surfaces, as visible in Figure 3.3 c) and Figure 3.8a). Surface pores at the top and bottom edges and internal pores constitute a discontinuous network. The tape manufacturing process and consolidation step strongly influence surface porosity. Similar complex surface pore features have been reported in the manufacturing of thermoplastic prepregs from aqueous polymer slurry [39], and the methodology proposed in this work shows the potential to further explore the characteristics of such materials in relationship to their performance.

Pores developing through the tape thickness are expected to negatively affect the local transverse strength of the tape; however, in the case of surface pores, they might provide advantages for air evacuation during subsequent processing, as seen in the case of partially impregnated prepregs [39]. The surface porosity related to the topological variability of the tape is instead more strongly associated with the roughness of the tape surface. In the case studied, where the tape surface is matrix-poor, local fibre path deviations from the main alignment direction  $z$  of the exposed fibres on the tape surface can be qualitatively observed, which is expected to influence both the tape surface roughness, and the consolidation performance [70]. The portion of surface pores linked to roughness is expected to disappear during part manufacturing and might positively contribute towards intimate contact development [57].

Details of the spatial arrangement of pores on the  $xz$  plane are represented in Figure 3.10, and more extensive examples are provided in Appendix D. Both internal pores (in blue) and surface pores (in cyan) might appear on  $xz$  cross-sections as separate 'collapsed' entities aligned in the principal fibre direction  $z$  inbetween the same fibres. Similar pore formations were observed in unidirectional thermoset composites as a result of the collapse of larger pores [71]. It is therefore possible that in the tape here analysed the same features might similarly originate from the degeneration of larger pores during processing. In particular, Figure 3.10 highlights that surface and internal pores are found at multiple locations to align along the  $z$  direction in close proximity, which suggests that part of the internal pore population could originate from the collapsed surface porosity. Overlaps between internal and surface pores were shown in their through-thickness distribution in Figure 3.8b) and in the cross-sectional clustering on the  $xy$  plane in Figure 3.7a), further suggesting that propagation between the two pore classes. The portion of surface pores entering the tape thickness might be more closely related to pore network propagation to internal porosity, and might favour air evacuation during consolidation [39]. The hypothesis derived from the tape analysis could be used to gain a deeper understanding of the tape manufacturing process, particularly in relation to the mechanisms of porosity evolution during resin impregnation.

### 3.4.2 DIFFERENTIAL TORTUOSITY

Differential tortuosity  $\tau_d$  was evaluated for each fibre at a local level to obtain a 3D distribution of the parameter. Figure 3.11a) shows a projection on the  $xy$  plane of the maximum differential tortuosity values for each fibre in Sub-Volume 1, highlighting the cross-sectional variability of the parameter in logarithmic scale. Values of  $\log_{10}(\tau_d) \geq 0$  shown in yellow indicate highest tortuosity values greater than 1, while  $\log_{10}(\tau_d) \leq -4$  in

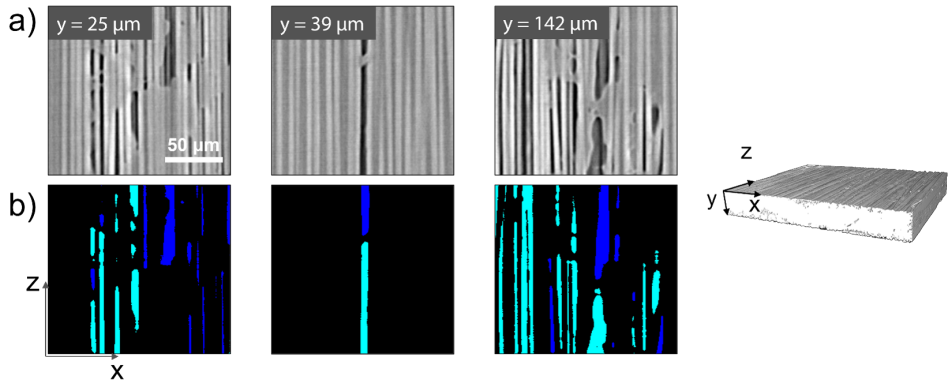


Figure 3.10: Examples from Sub-volume 1 of a)  $xz$  cross-sections of the scan volume; b) corresponding segmented pore views, indicating internal pores in dark blue and surface pores in cyan. The full cross-sections are available in Appendix D.

purple indicate values of tortuosity lower than 0.0001. The tortuosity maps corresponding to all sub-volumes can be found in Appendix C.

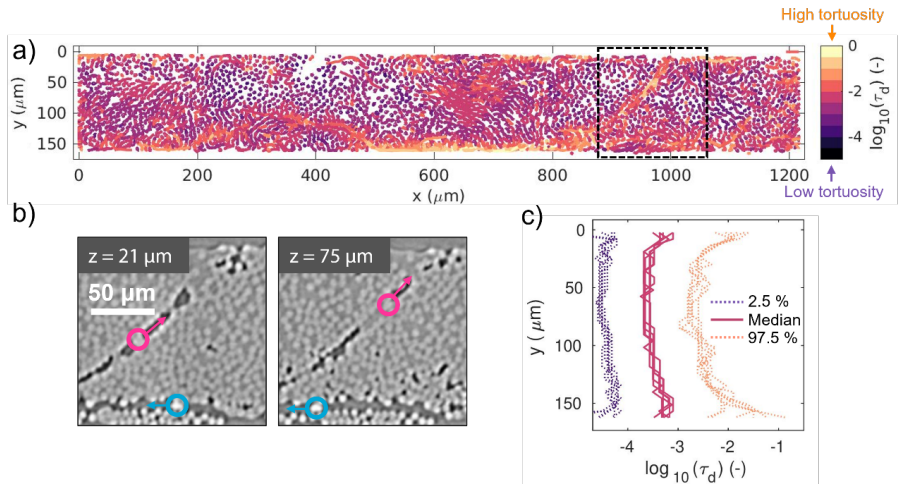


Figure 3.11: a) Cross-sectional distribution of the logarithm of differential tortuosity for Sub-volume 1, where each fibre path is projected on the  $xy$  plane and colour-coded depending on their maximum local tortuosity value; b) two fibre centres with visible ovalisation moving in high-tortuosity, one highlighted in magenta and one in blue, tracked at two  $z$  locations in the blue dashed regions in a); c) through-thickness distribution of differential tortuosity, each line corresponding to a different sub-volume. The median value, 2.5 % quantile and 97.5 % quantile are highlighted for each sub-volume.

Some fibres are observed to move along trajectories with high tortuosity and misalign-

ment, traversing the tape thickness or migrating along the bottom surface. Two such high-tortuosity fibres traversing the region marked with a black dashed square in Figure 3.11a) are highlighted in Figure 3.11b) in magenta and blue respectively, at two different locations along the tape length  $z$ . The trajectories of both fibres appear to intercept pore locations, visible in a darker colour in the greyscale image.

The through-thickness distribution of local tortuosity shown in Figure 3.11c) highlights an edge-core effect with higher tortuosity at the tape surfaces, especially pronounced in the 97.5 % quantile of the distribution, consistently for all sub-volumes.

### 3.4.3 RELATIONSHIP BETWEEN PORE DISTRIBUTION AND FIBRE TORTUOSITY

Qualitative observations of correspondence of the spatial distribution of both pores and tortuosity for Sub-Volume 1, corresponding to a lengthscale of 500  $\mu\text{m}$ , can be seen in the projection plane  $xy$  by comparing Figure 3.7 a) with Figure 3.11 a) and b). Higher tortuosity can be found at similar cross-sectional locations of higher pore fraction regions. The same observations can be extended for all sub-volumes with reference to Appendices A and C, suggesting that possible correspondences between tortuosity and pore distribution might remain valid both at a local and over longer lengthscales, possibly due to the propagation of both parameters along the main fibre alignment direction.

Further indication of a correspondence of the two descriptors can be provided by their through-thickness edge-core effect, with higher porosity and tortuosity at the tape edges, shown in Figures 3.8b) and 3.11e). On the tape surfaces, the greater freedom of fibre displacement translates to higher tortuosity, causing surface topological changes which are included in the definition of surface pores here proposed. In the case of thermoset unidirectional composite processing, pores can get trapped between fibres closer than a characteristic threshold [72], which is the case where high tortuosity and misalignment are present in conjunction to high fibre volume content. Comparable effects could be induced during thermoplastic tape manufacturing in the presence of similar features of the fibre architecture, depending on the impregnation strategy.

#### CORRELATION OF PORE DISTRIBUTION AND FIBRE DIFFERENTIAL TORTUOSITY

The 3D distributions of tortuosity, internal pores and surface pores were data-reduced by max-filtering as described in Section 3.3.3, and compared on a voxel-by-voxel basis. For each pore voxel, and for each pore-free voxel, the corresponding value of tortuosity was reported in Figure 3.12a) with differential tortuosity shown in logarithmic scale. Each line shown represents a distinct sub-volume. In the material studied, the methodology proposed was able to capture that distribution of tortuosity values intercepted by internal and surface pores shows a shift towards higher values compared to pore-free regions, consistently for all sub-volumes. In particular, regions with the highest range of tortuosity  $\log_{10}(\tau_d) \geq -2$  (corresponding to  $\tau_d \geq 0.01$ ) are found in surface pores and internal pores, but not in pore-free regions, highlighting the relevance of high tortuosity features on the pore population. In particular, surface pores are shown to have a larger tail of the distribution towards higher tortuosity values, suggesting a greater influence compared to internal pores. The results show consistency across the six sub-volumes, indicating that the conclusion is valid over an extended lengthscale.

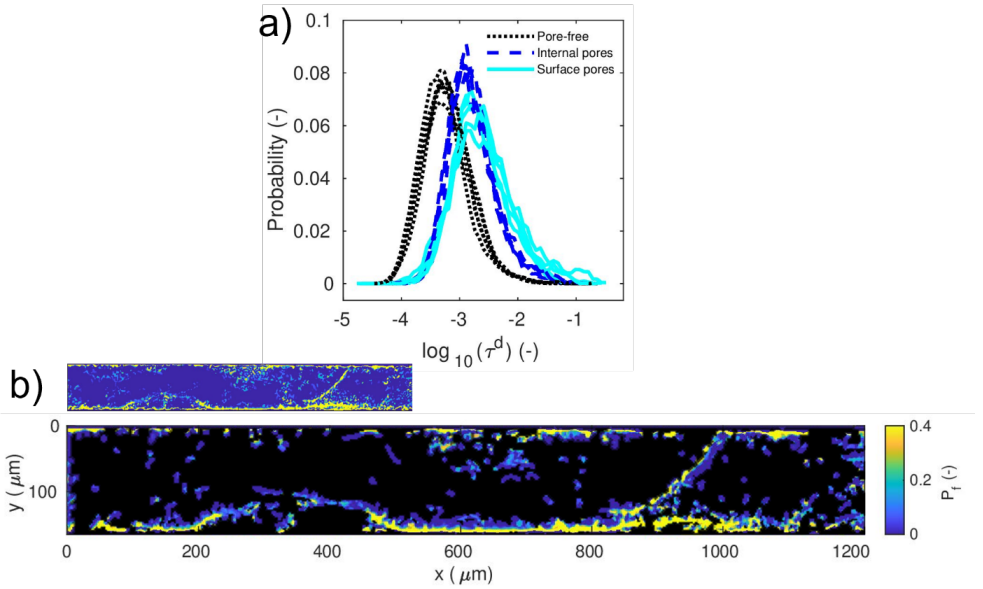


Figure 3.12: a) Differential tortuosity values in correspondence of pore-free regions, internal pores and surface pores for all sub-volumes; b) above: miniature image recalling the pore fraction distribution on the  $xy$  plane for Sub-volume 1 shown in Figure 3.7 a1); below: the same pore fraction distribution was masked in black, to display in colour only the pore probability overlapping to fibre trajectories in the higher tortuosity range with a maximum  $\log_{10}(\tau_d) \geq -2$ .

An added advantage of using data reduction is that small shifts between parameters are automatically taken into account. In principle, no fibres (hence, no tortuosity values) are present at exact pore locations, preventing an effective correlation. Through max-filtering with an adequately sized kernel, the local microstructural information can be more easily compared. Max-filtering might restrict the range of tortuosity values by cutting its lower range, but it is expected to locally enhance the visibility of areas of high tortuosity values to assess their influence on the surrounding microstructure, which is of value for the analysis. To clarify the effect of the max-filter element size results obtained, a sensitivity analysis was conducted as reported in Appendix G. The results of the sensitivity analysis highlight that the results shown are still valid in the range of element sizes employed.

A possible explanation of the relationship between tortuosity and pore distribution is at the level of microstructure formation. Regions with higher local tortuosity could generate cavities and barriers to resin flow during impregnation [72], creating far-field effects on the pore evolution. Furthermore, pore pressure can impose significant fibre movement in the case of thermoset matrices [72], and a similar effect might also occur in higher viscosity systems such as thermoplastic matrices. Pore evolution might therefore also influence, to a degree, the local fibre architecture in its immediate surroundings. Features such as collective bundling effects of fibres, fibre network connectivity (**Chapter 2**) [41], fibre neighbours contacts [37, 41, 73] and local fibre volume fraction could also impact the pore

distribution and should be addressed in future research to improve our understanding of the mechanisms of microstructure formation.

### MEANDERING FIBRES IN HIGH-TORTUOSITY REGIONS

The methodology developed highlighted strong interactions between high-tortuosity regions and the pore distribution. For the tape studied, the fibres in the highest tortuosity range move along preferential corridors running transversally to the thickness of the tape and along its lower edge with high misalignment from the principal fibre alignment direction. Examples are provided in Figure 3.11b) and Figure 3.13a). Since pores appear linked to high tortuosity regions in the tape studied, meandering fibres populating high tortuosity corridors constitute a key feature.

3

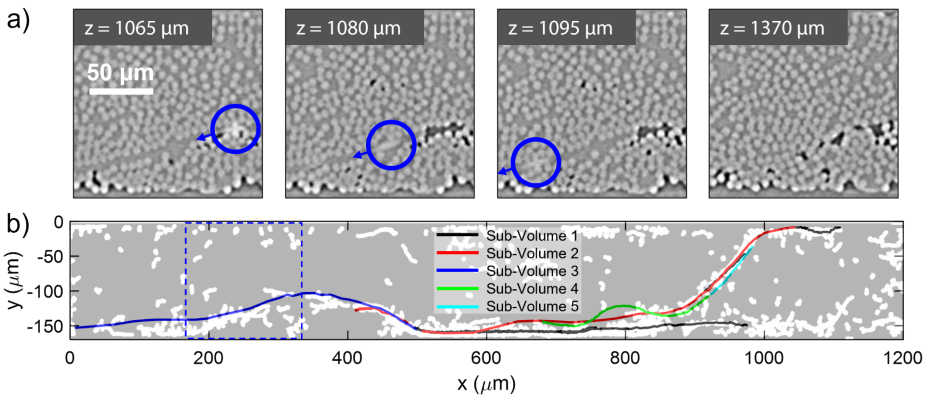


Figure 3.13: a) Meandering fibre visible inside the blue circle, at different locations along the tape length, and subsequent disappearance of the corridor generated in the last frame; b) manually tracked meandering fibre paths for Sub-Volume 1 to 5 projected on the  $xy$  plane, overlapping to the fibre trajectories with a maximum  $\log_{10}(\tau_d) \geq -2$  for Sub-Volume 1, shown in white. The cross-sectional region shown in a) is highlighted in a dashed square.

Such meandering fibres represent mechanically weaker points in the tape, and might initiate fracture [26], but might also lead to crack branching [74]. Furthermore, because carbon fibres are conductive, through-thickness fibre migration could constitute topology-dependent electrical percolation pathways [75] with possible consequences on the electrical conductivity of preregs for processing techniques such as induction welding. Meandering fibres constitute, therefore, a disruption of the microstructure that should be carefully controlled and tailored during manufacturing.

One possible hypothesis is that the presence of individual meandering fibres across the tape thickness might originate from local variations in tension across the fibre tow. Tension differences within the tow can occur during manufacturing; however, in the case of single meandering fibres, the loss of tension might result from the rupture of individual filaments on the tow surface due to frictional forces during dry tow spreading [52]. Limiting the degree of fibre breakage through control of the spreading process could, therefore, result in lower meandering fibres and more aligned microstructures, with reduced porosity events downstream in the manufacturing process.

Characterisation routes such as laser measurement units can be integrated as in-line techniques to aid in identifying broken fibres and improving the manufacturing control [76]. Meandering fibres traversing the thickness of prepregs with conductive fibre reinforcement, such as carbon fibres, could be identified via electrical conductivity measurements based on six-probe methods [75] and Eddy current testing [77]. In the application of 3D techniques such as lower resolution X-ray micro-computed tomography analysed with structure tensor method [78] and X-ray scattering tensor tomography [79], care should be used in avoiding excessive homogenisation of the microstructural information, as single fibre triggering events for larger scale phenomena might otherwise be missed.

Meandering fibres show high cross-sectional ovalisation on the  $xy$  plane and appear to move along resin-rich corridors, as also reported in the work of Yu et al. for highly misaligned fibres [80]. Local ordering effects are observed around such corridors, consisting of fibre alignment along the sides of the trajectory of meandering fibres, which are retained both before and after its passage. The meandering fibre highlighted in Figure 3.13a), which corresponds to the blue curve in Figure 3.13b) in Sub-Volume 3, appears in the field of view shown at about  $z = 1065 \mu\text{m}$  and exits it at  $z = 1095 \mu\text{m}$ , however, the corridor effect generated along its passage can be qualitatively observed to disappear only  $270 \mu\text{m}$  further in the principal alignment direction, at about  $z = 1370 \mu\text{m}$ . In general, the lengthscale affected by the transit of a meandering fibre is observed to be influenced by the tortuosity of the fibre. The local ordering effect around resin corridors left by fibres with high tortuosity and misalignment might be related to far-field effects on the surrounding microstructure and cause greater disruption in regions with high fibre volume fraction, which is the case in this work.

In the workflow used, the detection of meandering fibres is a tedious process due to their out-of-average behaviour. Trackmate might not recognise high tortuosity fibre correctly especially in the case of high ovalisation of their transversal cross-section. A careful selection of the "gap closing distance" was useful to link partially detected portions of a fibre, however, loss of information was still observed. The trajectories of some manually-tracked meandering fibres located in a high-tortuosity corridors in five consecutive sub-volumes are reported Figure 3.13b). The trajectories of some of those fibres span multiple volumes. A view of the manually traced fibres on the  $xz$  projection plane is shown in Appendix E. The fibres shown were only partially detected in the automated fibre extraction step. The microstructural information shown in Figure 3.11a), compared to the manually tracked fibres in Figure 3.13b), suggests that the overall effect of the high-tortuosity corridors was still conveyed in the analysis at the sub-volume scale. If more accuracy was needed in future work to strengthen the analysis further, the authors recommend image-pre processing techniques to facilitate distinguishing misaligned individual fibre trajectories at a 3D level [37, 81], and finer post-processing strategies to link partial fibre segments, as shown elsewhere in the literature [82].

### 3.4.4 DETERMINATION OF THE LENGTHSCALE OF PROPAGATION FOR PORE NETWORK AND TORTUOSITY

The methodology showcased in the previous Section highlighted a preferential location of pores in higher tortuosity regions, compared to pore-free areas, in the material used as the case study. In this section, a methodology to investigate the spatial evolution of the two



features is applied to assess possible correspondences in their lengthscale of propagation, based on the method introduced in Section 3.3.4.

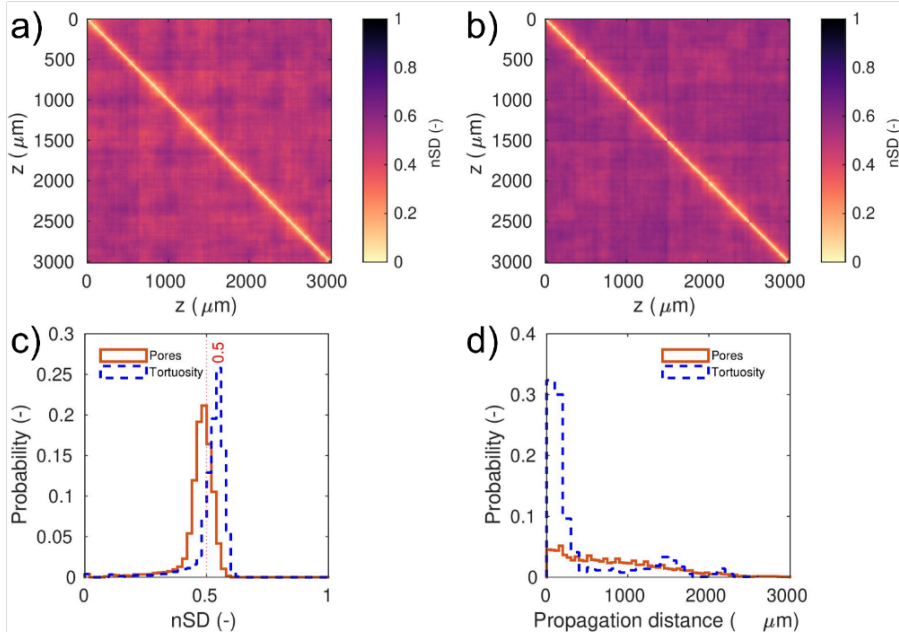


Figure 3.14: Distance map of the similarity score  $nSD$  for the full scan volume in relation to the  $x-y$  plane and a cubic max-filtering element of 15 voxel side for a) pores and b) differential tortuosity; c) histogram of the similarity score  $nSD$  for pore network and high differential tortuosity, with the selected threshold of evaluation at  $nSD = 0.5$  highlighted in a red dashed line; d) lengthscale of feature propagation for pore and tortuosity regions falling in the range  $0 \leq nSD \leq 0.5$ .

Figure 3.14a) and b) show the distance map obtained by determining  $nSD$  with a cubic kernel of 15 voxel side for each pair of max-filtered slices across the full volume for differential tortuosity and pores, respectively. The distance map of the similarity score is symmetrical with respect to the top-left-bottom-right diagonal. The values of  $nSD$  along said diagonal are obtained by comparing a cross-section with itself, resulting in a perfect match and, hence, a value of  $nSD$  equal to 0, indicating no change in the parameter distribution. For the same case of a cubic max-pooling element of 15 voxel size, a summary of the similarity values for Figure 3.14a) and b) is provided in the histograms of Figure 3.14c), which shows  $nSD$  in the range of 0 to 0.65 for both parameters. Based on the analysis performed in Appendix F, a value of  $nSD = 0.5$  was selected as a lower bound to assess feature similarity. At that value of  $nSD$ , half of the feature distribution is retained, while half has migrated to different locations. In this case, the 68 % of the pore regions and the 19 % of the high tortuosity regions fall in the range of  $nSD$  between 0 and 0.5, corresponding to the highest similarity range. The results indicate that while most pore regions propagate through the volume, at the scale observed high tortuosity regions show a greater local fluctuation.

The distribution of distances between  $xy$  cross-sections in which high similarity is encountered, hence with  $0 \leq \text{nSD} \leq 0.5$ , are reported in Figure 3.14d). For both the porosity network and high tortuosity regions, propagation distances are found up to the range of 2000–3000  $\mu\text{m}$ , going beyond the limit of single sub-volumes and reaching the edge of the scan volume analysed. Data related to propagation distances beyond 2000  $\mu\text{m}$  should however be considered with caution due to the limit in the size of the scan volume and consequent low sampling in the range 2000–3000  $\mu\text{m}$ .

The distribution of propagation distances for the pore network is wider compared to the high tortuosity, suggesting a greater retention of characteristic features along the fibre length direction. The results of pore network similarity might be influenced by the criteria used to define surface porosity, which is based on a fixed tape boundary valid at each  $xy$  cross-section for a sub-volume and might, therefore, increase similarity within the sub-volume. However, since the distribution of propagation distances found is much longer than the 500  $\mu\text{m}$  length of each sub-volume and that it was taken into account in the definition of the nSD threshold in Appendix F, the influence of the boundary choice on the results is expected to be limited.

In the case of tortuosity, a more evident peak in the 400  $\mu\text{m}$  range can be observed in Figure 3.14d), followed by a tail towards longer lengthscale values. Since the range of tortuosity that interests pore locations is wider than the one considered in the lengthscale analysis, a difference between high tortuosity and pore distribution was expected. In particular, restricting the range of tortuosity considered corresponds to isolating parameter variations more strongly influenced by local characteristics such as meandering fibres.

The similarity assessment was based only on the locations of pores and high-tortuous regions in their evolution along the alignment direction  $z$ . This means that regions that are, for example, pore-free are not assessed in the similarity analysis. The outcome should be therefore read as an indication of the stability along  $z$  of the pore locations. The choice was made to ensure that the focus of the evaluation was only on the features analysed.

Max-filtering creates a degree of local homogenisation in the similarity analysis, which can modulate the scale of feature observation while reducing the computational time. An adequate fine-tuning of the kernel used to extract characteristic lengthscales for specific case studies can aid in defining representative characteristics of the material. While the method development was conducted with a cubic kernel with a 15 voxel side, corresponding to about 1.5 times the fibre diameter, different kernel size choices are expected to affect the level of homogenisation and, therefore, the similarity results. A sensitivity analysis of the kernel size and its effect on the similarity results is shown in Appendix G, which highlights how the kernel size can modulate the observed scale of features, with smaller kernels capturing finer details and larger kernels highlighting broader distributions, although at the cost of increased homogenisation.

The lengthscales extracted through the similarity analysis for each microstructural feature considered could find application in the definition of Representative Volume Elements (RVE). RVE tailored to consider specific lengthscales of microstructural variability for different fibre and pore features might allow for more accurate modelling of composite prepregs. Due to the low sampling at the edges of the scan space, however, it is advisable that larger portion of the material should be assessed to the extinction of the features observed.



### 3.5 CONCLUSION

The work focused on the 3D microstructural analysis of an experimental unidirectional prepreg based on X-ray microcomputed tomography data, with a focus on the characterisation of its pore network and fibre architecture characteristics. To assess the consistency of the findings, the scan length was split into six sub-volumes in the principal fibre alignment direction to analyse the features of interest.

Pore distribution analysis indicated a tendency for both surface and internal pores to cluster in areas with increased tortuosity, indicating a complex relationship between pore evolution and fibre architecture that needs further investigation. This correlation suggests a strong connection between porosity evolution and fibre paths, and in particular potential interactions between pore distribution and meandering fibres, characterised by high tortuosity and misalignment. The results suggest that single meandering fibres can trigger larger-scale phenomena, features that might get overlooked in common homogenisation approaches typical of multiscale studies. A possible origin of meandering fibres is from the rupture of long fibres by friction during dry tow spreading, with consequent loss in tension. Early steps in the manufacturing process might, therefore, profoundly affect the final tape microstructure and lead to porosity events downstream in the process. The optimisation of the tape manufacturing process is of prime importance in controlling the final prepreg microstructure.

The quantification of characteristic lengthscales of the pore network and tortuosity along the principal alignment direction showed feature propagation across multiple sub-volumes. This work strongly indicates that the characteristic scale of feature propagation is beyond the current observation scale, emphasising the need to acquire larger volumes to assess characteristic lengthscales in unidirectional composite tapes. A deeper understanding of lengthscales of feature propagation might find application in developing more accurate representative volume elements of the tape microstructure.

The work is focused on the methodology development for the analysis of unidirectional composite tapes with complex pore structures, hence the extent to which the volume analyses is representative of the whole tape is not discussed. For a complete characterisation of a unidirectional tape and assessment of its variability, microstructural studies at multiple locations along the principal fibre direction and in the transversal direction would be advisable. Such a study could help clarify the effect of manufacturing processes that lead to the tape microstructure, and the tape performance in engineering practice. A first step in this direction is conducted in **Chapter 4**.



## 4

## CHARACTERISING THE VARIABILITY OF UNIDIRECTIONAL PREPREGS AT MULTIPLE OBSERVATION SCALES

4

*Understanding the microstructural variability in unidirectional composite prepreg tapes is relevant to investigating mechanisms of tape microstructure formation, their impact on its processability and the mechanical performance of the final composite part. It has been shown that three-dimensional microstructural variability at the single-fibre level can be resolved by X-ray micro-computed tomography (XCT). However, to define a representative microstructural fingerprint of a given tape, investigations at the required small voxel size lead to limited volumes of observation, which might not be representative. This research aims to extend these findings via a multiscale approach, considering scales of observations, from microscopic (single fibre) up to mesoscopic (dimension of tape) length scale, to generate further insight into the microstructural organisation of thermoplastic prepreg tapes. By exploring the ability of XCT imaging for carbon fibre-reinforced thermoplastic composites at different voxel sizes, the work aims to identify the limitations of the use of different scales of observations to capture features of microstructures and their propagation from micro- to mesoscale level. While structure tensor analysis appeared to correctly capture misaligned regions in XCT images with small voxel size (1/10 of the fibre diameter), the method proved ineffective for larger voxel size images (1/2 of the fibre diameter).*

## 4.1 INTRODUCTION

Understanding the microstructural variability in unidirectional composite prepreg tapes, which are critical for the automation of large-scale composite production, is relevant for investigating mechanisms of microstructure formation and their impact on the processability and mechanical performance of the resulting composite part. Investigations based on X-ray micro-computed tomography (XCT) are becoming increasingly common in the field of composite characterisation to understand its three-dimensional (3D) variability. High-resolution XCT scans resolving individual fibres provide detailed microstructural information to identify relevant morphological characteristics in unidirectional composites. Approaches quantifying clustering effects in the fibre organisation [84], tortuosity of trajectories, bundling effects and 3D inter-connectivity in fibrous architecture (**Chapter 2**) [41] allow for local variability studies and highlight fine aspects of the level of organisation in the material. Evaluation of how processing or mechanical loading affects the microstructure can also be quantified, for example, in relation to debulking [85], bundle reorientation during compression loading [18], and kink band formation [86].

In manufacturing unidirectional composite prepregs, accurate microstructure characterisation is essential to identify local defects, such as regions of significant fibre misalignment. These features can adversely affect the mechanical performance of composites, particularly in terms of longitudinal stiffness and compressive strength [87, 88]. In high-fibre volume fraction tapes, individual highly tortuous or misaligned fibres can also influence the local organization of the surrounding microstructure, with their effects propagating over hundreds of micrometres (**Chapter 3**) [58]. While high-resolution XCT scans (with voxel size around 1/10th of the fibre diameter, discussed in our previous work on carbon fibres-reinforced tapes (**Chapter 2** and **Chapter 3**) [41, 58, 61], provide fine-scale details and allow clear visualization of single misaligned fibre effects, their limited field of view and long scan times make them impractical for analyzing large areas of tapes. These constraints, compounded by the high-resolution requirements of single-fibre tracking, limit the applicability of XCT for manufacturing quality screening and process optimization. Finding ways to identify single-fibre misalignment effects at a coarser resolution over larger areas would, therefore, help make XCT a more accessible technique for manufacturing quality screening. However, all these approaches have limitations due to the limited field of view, typically a few millimetres.

Structure tensor analysis is an image analysis technique that has been widely used in the study of fibre-reinforced composite materials due to its ability to capture fibre orientation distributions across a broad range of resolutions, with voxel sizes reported from approximately one to three fibre diameters in glass fibre composite laminates [22, 78]. Karamov et al. demonstrated the method's fidelity by comparing histograms of orientation angle components derived from single-fibre analysis and structure tensor calculations. Their results showed a strong correlation, suggesting that structure tensor analysis is effective for evaluating local variability even at lower resolutions [22]. Jeppesen et al. used structure tensor analysis to compare fibre orientation variability in unidirectional carbon fibre prepreg laminates and pultruded profiles. The method effectively quantified differences in the standard deviation of fibre orientations, enabling meaningful comparative studies [21]. Furthermore, Ferguson et al. applied structure tensor analysis to evaluate kink band formation in pultruded carbon fibre composites at a resolution of 2  $\mu\text{m}$ , showcasing

its utility in identifying critical structural features [40]. Even though the applicability of structure tensor analysis is vast in the composites field, the specific case of free-standing unidirectional carbon fibre prepreg tapes has yet to be addressed in the literature.

Multiscale approaches might bridge the gap between high-resolution observations and macroscale variability in unidirectional composite tapes. Additionally, assessing information loss from varying voxel sizes is critical for ensuring that essential features of the microstructure are accurately represented. This Chapter aims to investigate a multiscale approach in the case of unidirectional carbon fibre-reinforced thermoplastic tapes exposing misalignment areas to observe the propagation of defects in scans performed at different voxel sizes. By integrating observations across multiple scales, this work evaluates the effectiveness of state-of-the-art image analysis methods in quantifying variability at the fibre levels across different voxel sizes. To achieve this, low-voxel size scans were used to establish ground truth data for individual fibre tracking. These results were then compared with microstructural metrics resulting from the structure tensor method at coarser voxel sizes.

## 4.2 MATERIALS AND METHODS

### 4.2.1 SAMPLE ACQUISITION

To allow a multiscale approach for studying microstructural features in a commercial grade of Toray Cetex 1225TC carbon fibre-reinforced thermoplastic prepreg tapes (Toray), four samples measuring 25 mm by 25 mm were extracted from a 300 mm wide tape along the width direction. A schematic is shown in Figure 4.1a. Characterization was performed via XCT to generate datasets at different voxel sizes: 0.8  $\mu\text{m}$ , 2  $\mu\text{m}$ , and 3.5  $\mu\text{m}$ . The XCT measurements were performed using a Zeiss Xradia Versa 520. Geometric magnification was optimized to achieve the desired total magnification in combination with either 0.4x or 4x optical magnification. A total of 2401 projections were acquired per scan, utilizing a 2024 x 2024 pixel CCD sensor operated without pixel binning. Volumetric data was reconstructed by Filtered Back Projection (FBP). The image acquisition settings used for the different magnifications are given in Table 4.1. For each sample, the scans for all magnifications were obtained in a single session to avoid misalignment between the scan volumes at different voxel sizes and to aid in identifying a common region of interest between the volumes at different voxel sizes. A cross-section of the region of interest considered for the following analysis is shown in Figure 4.1b for Sample 4 at all resolutions. For the measurement, the tapes were clamped at their bottom side and free-standing in air, visible in a darker colour at the top and bottom of the region of interest. Microporosity is present and distinguishable as darker regions through the tape cross-section, while fibres can be seen as lighter circles. The resulting sizes of the regions of interest for the four samples are reported in Table 4.2.

### 4.2.2 MICROSTRUCTURAL ANALYSIS

The acquired volumes were manually registered in Fiji [44] to orient the tapes along their principal fibre alignment direction. The same region of interest was identified at all voxel sizes via manual volume selection. The scanned samples showed microporosity. To aid in dedicated steps for the fibre architecture analysis, segmentation of fibres and pores was performed via the Fiji plugin Weka trainable Segmentation [44, 46]. Segmentation of the

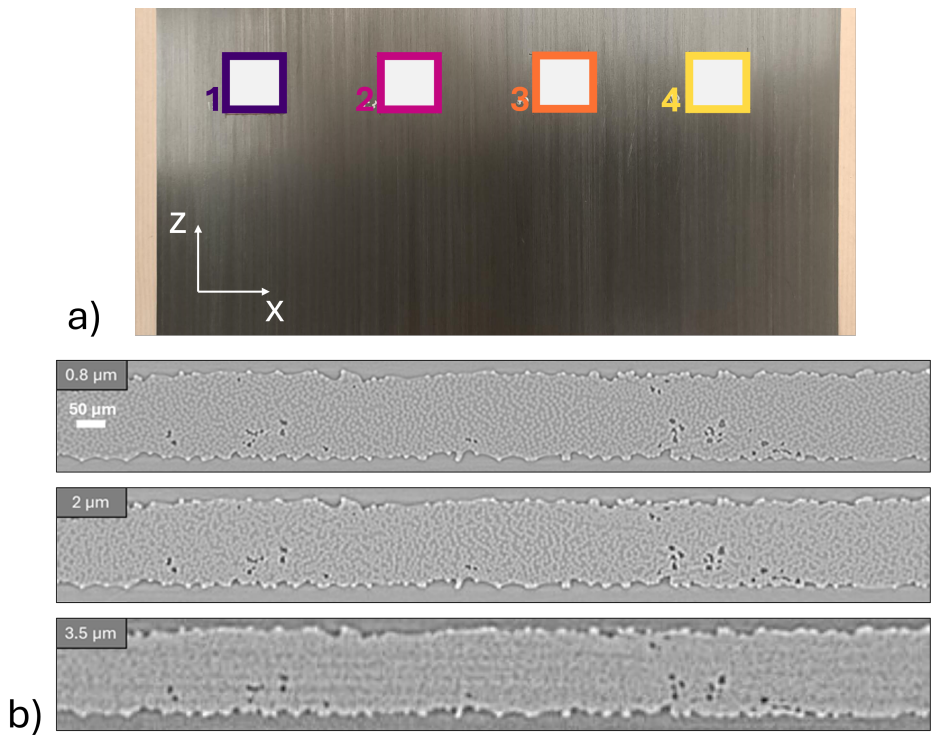


Figure 4.1: a) Schematic of the sample extraction from the unidirectional tape, with z fibre alignment direction and x direction along the tape width, b) For Sample 4, same transversal cross-section in the region of interest (xy plane) of overlap at the three voxel sizes considered.

Voxel size ( $\mu\text{m}$ )	0.8	2	3.5
Voltage (kV)	80	80	80
Power (W)	7	7	7
Projections (-)	2401	2401	2401
Exposure time (s)	12	12	6.7
Magnification (-)	4x	4x	0.4x

Table 4.1: Settings used for the X-Ray Computed Tomography volume acquisition.

fibrous phase was conducted only on the 0.8  $\mu\text{m}$  and 2  $\mu\text{m}$  voxel size datasets since higher voxel size led to excessive homogenisation for fibre phase extraction. Pore information was used in this work to optimise the segmented fibre maps for artefact suppression. The segmented pores for the 0.8  $\mu\text{m}$  and 2  $\mu\text{m}$  voxel size scans were further processed by morphological filtering in Fiji via MorpholibJ [89] via 3D opening with a spherical element of radius size 2 and 1, respectively, for artefact removal, while further morphological operations were not performed on the 3.5  $\mu\text{m}$  scan.

Direction	Sample 1	Sample 2	Sample 3	Sample 4
x ( $\mu\text{m}$ )	1526	1242	1546	1495
y ( $\mu\text{m}$ )	164	187	210	197
z ( $\mu\text{m}$ )	1084	1388	1400	1440

Table 4.2: Size of the region of interest for the four samples. The direction x aligns to the tape width direction, y to the thickness, z to the fibre alignment direction. Dimensions were calculated based on the  $0.8 \mu\text{m}$  dataset and rounded to the nearest integer.

### STRUCTURE TENSOR ANALYSIS

Structure tensor analysis captures local orientations in the image with a variation in image intensity by applying gradient operations. Given a scalar field  $V(x, y, z)$ , such as a greyscale 3D image, the second-order structure tensor can be determined as:

$$S = \sum \nabla V \cdot \nabla V^T = \sum \begin{bmatrix} \left(\frac{\partial V}{\partial x}\right)^2 & \frac{\partial V}{\partial x} \frac{\partial V}{\partial y} & \frac{\partial V}{\partial x} \frac{\partial V}{\partial z} \\ \frac{\partial V}{\partial y} \frac{\partial V}{\partial x} & \left(\frac{\partial V}{\partial y}\right)^2 & \frac{\partial V}{\partial y} \frac{\partial V}{\partial z} \\ \frac{\partial V}{\partial z} \frac{\partial V}{\partial x} & \frac{\partial V}{\partial z} \frac{\partial V}{\partial y} & \left(\frac{\partial V}{\partial z}\right)^2 \end{bmatrix} \quad (4.1)$$

This matrix is computed at each point by summing the outer products of the image gradient  $\nabla V$  with itself over a local neighbourhood. Each entry in the matrix encodes directional correlations of gradients: for instance,  $\frac{\partial V}{\partial x} \frac{\partial V}{\partial y}$  represents the co-occurrence of changes along the x and y directions.

The Gaussian derivative can be adopted to compute the intensity gradient  $V$  with a kernel size  $\sigma$  [21, 90], and the structure tensor is constructed by convolution with a Gaussian kernel  $K_\rho$ :

$$S = K_\rho * (\nabla V_\sigma \cdot \nabla V_\sigma^T) \quad (4.2)$$

In this formula,  $*$  represents convolution,  $\sigma$  (smoothing scale) is the standard deviation of the Gaussian filtering kernel applied to the image prior to gradient computation, determining the balance between noise suppression and the preservation of fine structural details, and  $\rho$  (integration scale) represents the standard deviation of the Gaussian kernel  $K_\rho$  over which the local gradient products are averaged, influencing the robustness and spatial coherence of the resulting orientation estimates. The formulation of the structure tensor used in this work follows the implementation by Jeppesen et al. [91]. Their code uses isotropic Gaussian kernels, a smoothing scale ( $\sigma$ ) and integration scale ( $\rho$ ) tailored to the voxel size and fibre diameter as follows:

$$\sigma = \sqrt{\frac{(R_f/v)^2}{2}} \quad (4.3)$$

$$\rho = 4 \cdot \sigma \quad (4.4)$$

where  $R_f$  is the fibre radius, and  $v$  is the voxel size. The values of  $\sigma$  and  $\rho$  (given in voxel) for the three voxel sizes considered are reported in Table 4.3. Since fibre structures have

abrupt intensity variations across their transversal cross-section but almost zero intensity change in the longitudinal direction, their orientation can be determined as the direction of minimum grayscale intensity variation, attributed to the eigenvector corresponding to the smallest eigenvalue of the second-order structure tensor. In this work, the misalignment angle  $\theta$ , ranging from  $0^\circ$  to  $90^\circ$ , is defined as the angle between the local material direction identified via the structure tensor and the principal fibre alignment direction  $z$ . In this work, we do not measure the azimuth angle on the  $xy$  plane as this is prone to high errors due to typically small angles  $\theta$ , especially at high voxel size. A schematic is shown in Figure 4.2.

Processing	0.8 $\mu\text{m}$	2 $\mu\text{m}$	3.5 $\mu\text{m}$
Unfiltered (U)	$\sigma=3.09, \rho=12.36$	$\sigma=1.24, \rho=4.96$	$\sigma=0.71, \rho=2.84$
Segmentation Masking (SM)	$\sigma=3.09, \rho=12.36$	$\sigma=1.24, \rho=4.96$	$\sigma=0.71, \rho=2.84$
Segmentation Masking + beta filtering (SM $\beta$ )	$\sigma=3.09, \rho=12.36,$ $\beta=0.95$	$\sigma=1.24, \rho=4.96,$ $\beta=0.95$	$\sigma=0.71, \rho=2.84,$ $\beta=0.88$

Table 4.3: Summary of methods used for fibre misalignment analysis at different voxel sizes.

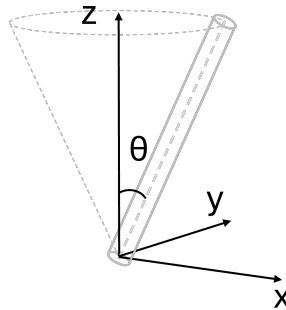


Figure 4.2: Schematic illustrating the definition of the misalignment angle  $\theta$  of a straight fibre segment from the principal fibre alignment direction  $z$ .

In the methodology used by Jeppesen et al. [90, 91], the structure tensor on the full 3D space is first calculated, followed by filtering with a mask based on the Otsu thresholding of the grayscale original volume, isolating the fibrous phase and excluding matrix regions presumed devoid of fibre directional information. However, the results were shown on images of the fully consolidated laminates in the absence of porosity or edges of the material, which, in the case of unidirectional tapes, become highly relevant due to their lower thickness and higher porosity content. Since in the case study considered in this work, additional artefacts related to defects such as porosity were encountered, Otsu thresholding was substituted by the combination of the Otsu-thresholded probability map of segmented fibres derived from Weka segmentation and of the segmented pores. In addition, structural anisotropy was used as a filtering criterion for further artefact removal to correct for



imperfections in the segmentation approach. The approach was employed in literature to aid in segmentation analysis of matrix and yarns of different orientations in carbon fibre-reinforced woven composites by considering anisotropy and orientation angle [92], and to segment tows, matrix pockets and pores in carbon fibre-reinforced unidirectional composite laminates [8]. The structural anisotropy was calculated at each voxel location as:

$$\beta = 1 - (\lambda_{min} / \lambda_{max}) \quad (4.5)$$

where  $\lambda_{min}$  and  $\lambda_{max}$  are, respectively, the maximum and minimum eigenvalues of the structure tensor at each voxel location. In case of high structural anisotropy, the value of  $\beta$  will tend to 1 ( $\lambda_{min} \ll \lambda_{max}$ ), while in regions of low anisotropy  $\beta$  will tend to zero ( $\lambda_{min} \approx \lambda_{max}$ ). In the case of unidirectional composites, the assumption justified by the literature is that regions with greater anisotropy should generally be more closely related to the fibrous microstructure [8]. In comparison, regions with lower anisotropy should indicate regions of porosity, matrix-rich areas and interfaces between the two. For the voxel size of  $0.8 \mu\text{m}$  and  $2 \mu\text{m}$ , an anisotropy threshold value of  $\beta = 0.95$  was chosen. In the case of the  $3.5 \mu\text{m}$  voxel size dataset, a lower value of  $\beta = 0.88$  was deemed more suitable, as the threshold used for finer voxel sizes led to the exclusion of structure tensor values in large areas of tape. The parameters for the three voxel size datasets and data refinement levels are summarized in Table 4.3.

#### SINGLE FIBRE ANALYSIS

The methodology for analysing low-voxel size scans at  $0.8 \mu\text{m}$  was based on the method shown in our previous work, applied to the segmented fibre maps (**Chapter 2** and **Chapter 3**) [41, 58, 61]. The segmented fibrous phase, optimised by further filtering from pore artefacts, allowed us to trace individual fibre paths with the Fiji plugin Trackmate [47] using the same parameters highlighted in the methodology in **Chapter 3**. The fibre trajectories were detected over  $60 \mu\text{m}$  and further processed in Matlab to interpolate missing data linearly via the function ‘fillmissing’ and smooth them via the function ‘smooth’ with a 2nd-order polynomial and an interpolation length of  $50 \mu\text{m}$ . Since the kernel radius used here for structure tensor analysis for all datasets has a diameter of  $[2.4 \cdot \rho \cdot v] = 79.36 \mu\text{m}$  (with  $v$  voxel size), a comparable measure of the angular misalignment from the principal alignment direction for each detected fibre was determined locally at each detected traces fibre location with a moving window of  $80 \mu\text{m}$ .

## 4.3 RESULTS AND DISCUSSIONS

### 4.3.1 SINGLE FIBRE TRACKING

The method described previously for single fibre trajectory extraction was only applied to the  $0.8 \mu\text{m}$  voxel size dataset. For the  $2 \mu\text{m}$  voxel size dataset, tracking was not successful, as segmentation led to large connected regions of fibres that could not be effectively separated into entities which could be traced via Trackmate. Consequently, fibre tracking was not attempted for the  $3.5 \mu\text{m}$  voxel size dataset. The material variability across the different samples analysed is shown in Figure 4.3. The presence of highly misaligned regions can be observed in Figure 4.3a for Sample 4, where each 3D fibre trajectory is projected on

the transversal cross-sectional plane and is colour-coded depending on its maximum local misalignment value. The same representation is provided for all Samples in Appendix H. Highly misaligned fibres are shown in a darker colour and can be observed at the tape's top and bottom surfaces, as well as in discrete locations through the tape thickness. The histogram in Figure 4.3b displays all local misalignment values calculated at each point of the extracted fibre trajectories over an axial length of  $80\ \mu\text{m}$ , which highlights microstructural variability within each sample, with an initial peak for all samples at low local misalignment angles and a tail towards high misalignment angles up to angles of about  $40^\circ$ . While the majority of the local 3D fibre segments analysed have low misalignment values, which is expected in the case of an unidirectional composite tape, the presence in the fibre architecture of regions of higher misalignment is a relevant microstructural feature to highlight since they negatively impact the longitudinal strength of the material [87] and its stiffness [88], with higher likelihood of fracture initiation [26].

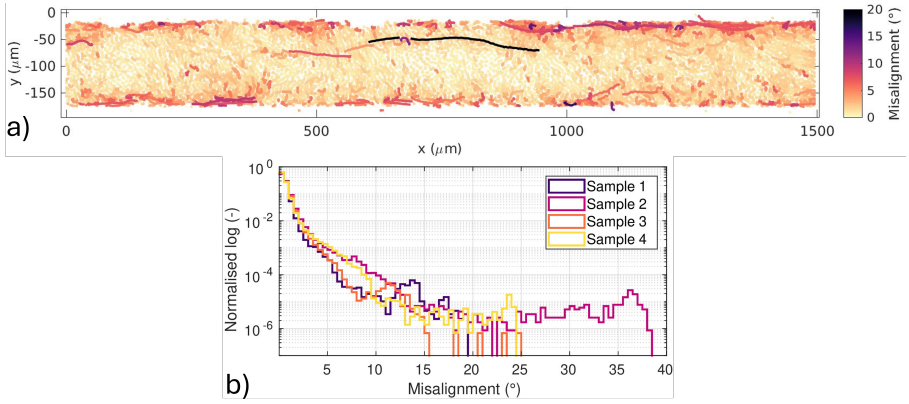


Figure 4.3: a) Consolidated view of the 3D misalignment distribution at a single fibre level for Sample 4 in the  $0.8\ \mu\text{m}$  voxel size dataset, where each fibre is projected on the transversal cross-section and colour-labelled with its maximum local misalignment value b) Histogram of the local misalignment range for Samples 1-2-3-4 at a  $0.8\ \mu\text{m}$  voxel size.

#### 4.3.2 STRUCTURE TENSOR ANALYSIS

Three procedures of the structure tensor analysis are compared at first. As summarized in Table 4.3, the unfiltered misalignment (U), misalignment after segmentation masking (SM), and misalignment after segmentation masking with anisotropic filtering ( $\text{SM}\beta$ ) are three levels of refinement of the structure tensor output which affect the range of the obtained fibre orientations. Exemplarily, Sample 4 at  $2\ \mu\text{m}$  voxel size is shown in Figure 4.4.

To visualize 3D fibre orientations in a 2D representation, the maximum misalignment angle  $\theta$  along the z-axis at each transversal cross-section location is shown for the three levels of data refinement in Figure 4.4a-c. In the unfiltered misalignment dataset (U), structure tensor calculations reveal artifact-laden fibre orientation information, particularly outside the tape region (e.g., in air) or in areas with complex features such as pores and

matrix boundaries, where sharp angular variations occur and are translated by structure tensor calculation in high-angle values. Processing the structure tensor values using a segmentation mask (SM) and applying anisotropic filtering ( $SM\beta$ ) effectively reduced these artefacts while preserving regions of high fibre misalignment observed in similar cross-sectional locations as identified in the single fibre analysis (Figure 4.3a).

While only consolidated cross-sectional data for Sample 4 are shown, the histogram comparison in Figure 4.5 shows quantitatively the impact of masking on the 3D structure tensor values on all samples, highlighting a common trend: anisotropic filtering significantly reduced the range of high-misalignment values detected, restricting the upper limit to approximately  $15\text{--}27^\circ$  across all datasets. While the range of angles obtained after  $SM\beta$  filtering was relatively consistent for Samples 1, 3, and 4 with the results obtained via single fibre analysis, the structure tensor method did not accurately capture the full range of misalignment values for Sample 2, which single-fibre analysis revealed to extend up to  $\approx 40^\circ$ . Further investigation is needed to refine the threshold values for anisotropic filtering and assess their influence on the observed microstructural features and the extent to which it might inadvertently mask significant misalignment features when the proximity of high misaligned fibres and matrix-pore interfaces occurs.

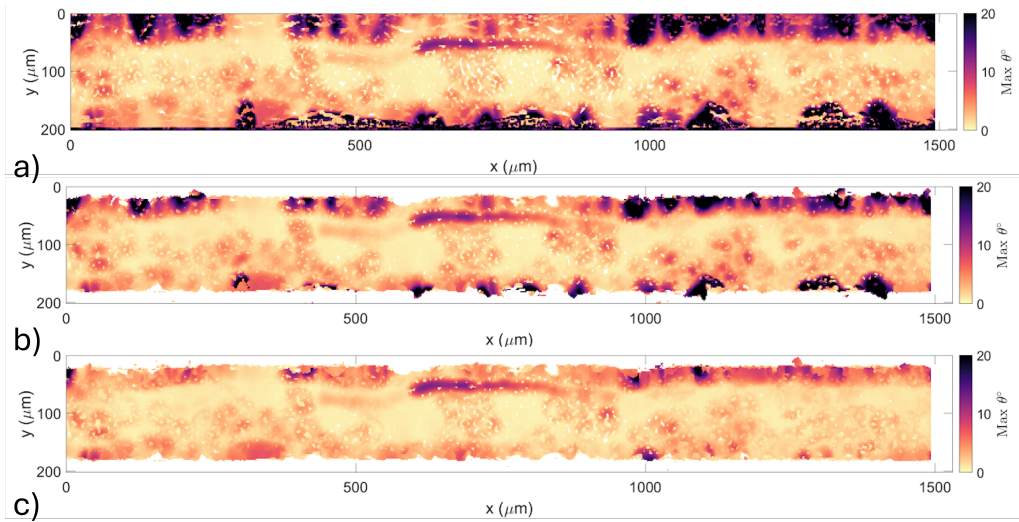


Figure 4.4: Consolidated view of the 3D structure tensor via its maximum value for each location on the xy plane for the  $2\text{ }\mu\text{m}$  voxel size scan of Sample 4: a) before filtering b) after filtering with a mask based on fibres and pores segmentation c) after anisotropic filtering.

To evaluate more in detail the reliability of the methodology used to represent the cross-sectional distribution of maximum misalignment angles  $\theta$ , Sample 4 after  $SM\beta$  masking was here reported for the three datasets at  $0.8\text{ }\mu\text{m}$ ,  $2\text{ }\mu\text{m}$ , and  $3.5\text{ }\mu\text{m}$  voxel size (Figure 4.6a1–a3). The equivalent views for all Samples studied are reported in Appendix I. The structure tensor successfully captured features such as edge-core effects in the cross-sectional misalignment distribution at the finest voxel size ( $0.8\text{ }\mu\text{m}$ ,  $\approx 10$  voxels across the fibre diameter). However,

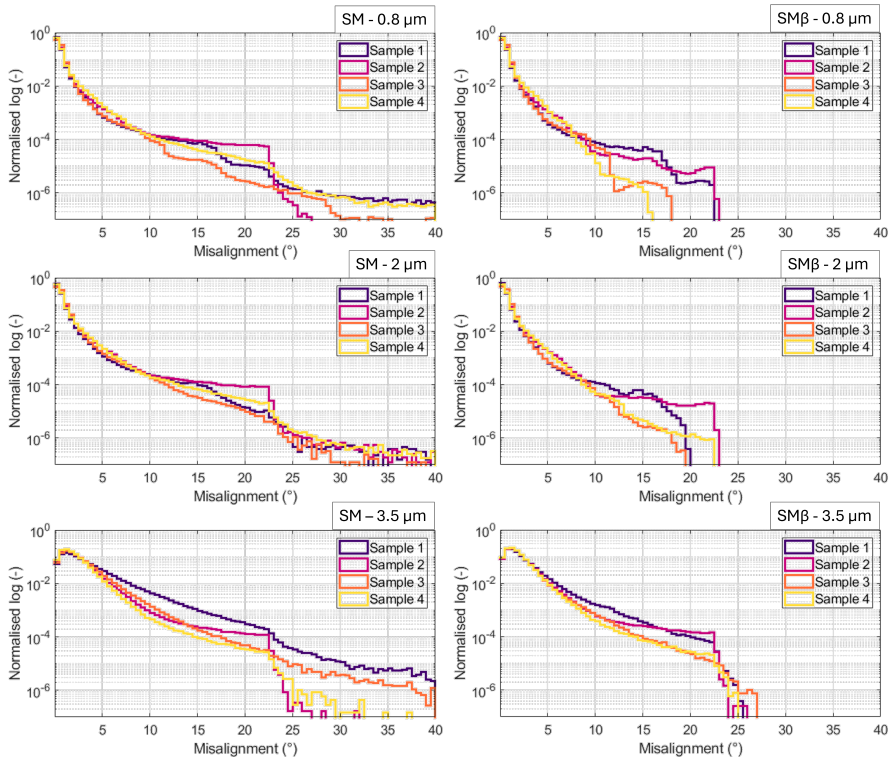


Figure 4.5: Histogram of the full range of misalignment angles derived from structure tensor for Samples 1-2-3-4, after segmentation masking (SM) and after anisotropic filtering (SM $\beta$ ).

the high-misalignment region in the tape bulk (600–800  $\mu\text{m}$  width, Figure 4.6a1) displayed a lower range of values compared to single-fibre trajectory analysis (Figure 4.3a), indicating potential limitations in the accuracy of misalignment angles derived from the structure tensor. This discrepancy was also evident in the histograms (Figure 4.5 versus Figure 4.3b), where the structure tensor yielded lower maximum misalignment values than single-fibre analysis.

For larger voxel sizes, the visibility of fine features diminished, and noise increased. At 2  $\mu\text{m}$  ( $\approx 3$  voxels across the fibre diameter, Figure 4.6a2), analysis uncertainty rose, with the structure tensor showing “bleeding” effects into surrounding areas [21], resulting in an inflated cross-sectional distribution of high-misalignment values. At 3.5  $\mu\text{m}$  ( $\approx 2$  voxels across the fibre diameter, Figure 4.6a3), noise and discretization errors led to overestimated misalignment values, as reflected in histograms (Figure 4.5d). A noticeable shift in the distribution peak for low misalignment toward  $\approx 2^\circ$  was observed and further quantified in Figure 4.6b, which reports the mean values of the full 3D misalignment distribution derived from both structure tensor and single fibre analysis. The standard deviation of the 3D misalignment values also shows a distinct increase in all 3.5  $\mu\text{m}$  datasets compared to lower voxel sizes as shown in Figure 4.6c, which is consistent with the observations of

Straumit et al. [92] in steel-epoxy unidirectional composites at a same voxel size-to-fibre diameter ratio.

The effects observed are likely due to approaching the Nyquist limit, which affects the resolution and precise identification of low-misalignment regions. While the number of sampling voxels per fibre, as well as the noise and contrast levels in the image, are expected to influence the resolution of fibre features, it is possible that the appropriate scan coarseness for reliably resolving these features is determined not solely by fibre diameter but also by inter-fibre distance, and therefore depends on the characteristics of the heterogeneous morphology. This tape exhibits several regions of close fibre packing, as qualitatively observed in the cross-section of Sample 4 in Figure 4.1b. In contrast, other carbon-fibre-reinforced unidirectional prepregs with lower fibre volume fraction and greater inter-fibre spacing may allow for scans across a wider range of voxel sizes where fibres remain sufficiently resolved for tensor evaluation (and for single-fibre tracing, as described in Section 4.3.1).

While the above considerations are based on 3D histogram distributions of misalignment values and their consolidated 2D representations, future work should delve deeper into the 3D spatial relationships of misalignment values and their propagation through the volume to assess with greater detail the differences in accuracy of the methods used (single fibre and structure tensor) in the local misalignment values identification at a 3D level. Additionally, there is not a clear agreement on an analytical definition of smoothing and integration scales, as different formulations were reported in the literature [78, 90]. A more tailored choice of these parameters could enable more effective feature extraction from datasets with larger voxel sizes, as suggested in the literature [21, 40, 78].

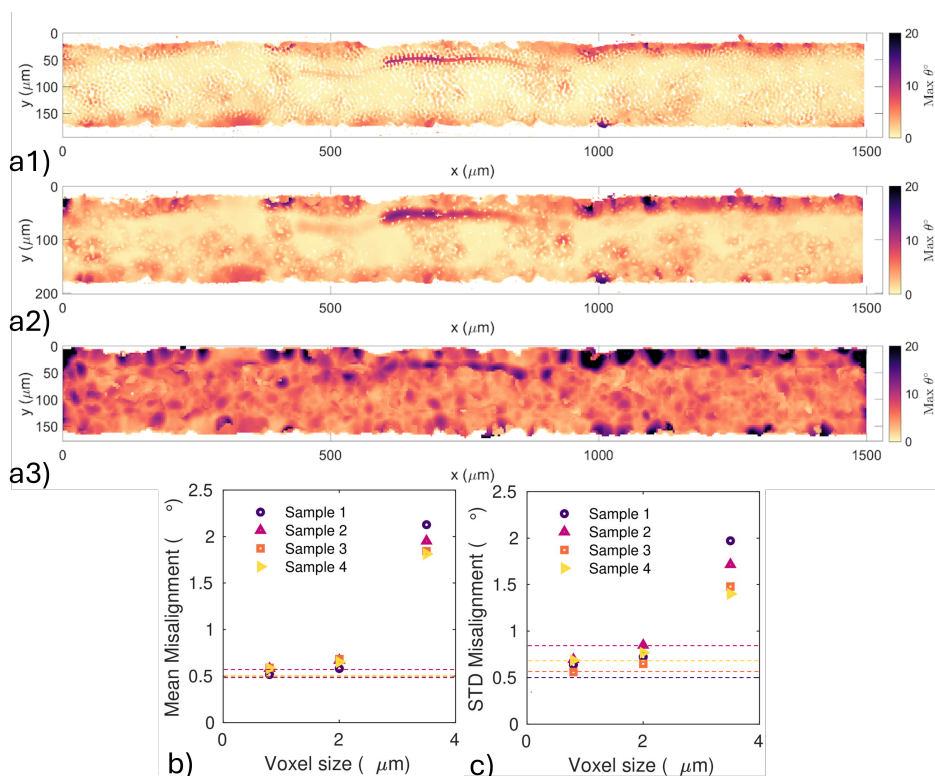


Figure 4.6: Consolidated view of the misalignment angle  $\theta$  derived from the 3D structure tensor via its maximum value for each location on the xy plane for Sample 4 at different voxel sizes after SMbeta filtering: a1) 0.8  $\mu\text{m}$  a2) 2  $\mu\text{m}$  a3) 3.5  $\mu\text{m}$ ; b-c) mean and standard deviation (STD) of the 3D misalignment values obtained via structure tensor analysis (symbols in the legend) and from single fibre analysis (horizontal lines following the same colour-coding).).

## 4.4 CONCLUSION

This chapter demonstrated a novel methodology for assessing microstructural variability in unidirectional carbon fibre-reinforced tapes using multiscale XCT imaging. By systematically varying voxel sizes, we identified critical thresholds for fiber-level analysis. The findings offer recommendations for selecting appropriate voxel sizes depending on the level of detail required, as reported in Table 4.4 as a practical guidance to researchers and practitioners. Single fibre reconstruction was feasible only at the smallest voxel size (0.8  $\mu\text{m}$ , 1/10th of the fibre diameter). At the same time, structure tensor analysis extended the capability to observe effects related to single fibre misalignment phenomena to voxel sizes up to 2  $\mu\text{m}$  (1/3rd of the fibre diameter). While the cross-sectional distribution of maximum misalignment values displayed for one of the samples showed close qualitative similarities to the distribution obtained at a single fibre level, the workflow used via structure tensor appears to lose information on high local misalignment angles above 25  $^\circ$ , highlighting pos-



sible limitations of the method in accurate angle determination. Larger voxel sizes ( $3.5\text{ }\mu\text{m}$ ,  $1/2$  of the fibre diameter) were unsuitable for misalignment evaluation via structure tensor due to excessive local homogenization most likely due to approaching the Nyquist limit for fibre features, leading to significant information loss. Key challenges in the structure tensor analysis at all voxel sizes included artefacts caused by phase boundaries and air gaps interpreted as high misalignment, most likely due to the sharp directionality variations in those tape regions. The novelty of combining machine-learning-based segmentation strategies with filtering via structure tensor eigenvalue anisotropy reduced high-angle artefacts and proved essential for accurately highlighting areas populated by misaligned fibres. In this context, optimization of segmentation techniques and anisotropic filtering thresholds should be pursued to enhance the precision of feature extraction.

To summarise, while fine voxel size scans are still the standard for the analysis of fine microstructural features related to single fibre misalignment in unidirectional composite tapes, structure tensor analysis shows potential for bringing the analysis to a mesoscale level, potentially allowing to follow feature propagation over larger regions and reducing the requirements for XCT scanning. Within the Nyquist limit for feature detection, the limits of data processing for the voxel size reported in this study could possibly be relaxed to higher values in tapes with lower fibre volume fraction and greater inter-fibre spacing, which in these samples is observed to be qualitatively lower than the fibre diameter and might be a limiting factor in feature resolution. The adequate scan coarseness might, therefore, be highly dependent on the characteristics of the heterogeneous morphology. Future work should address the 3D spatial relationships between local fibre misalignment and larger microstructural phenomena with statistical rigour. Such insights could inform the development of predictive models linking single-fibre behaviours to bulk material properties, ultimately aiding in optimising tape manufacturing processes for improved mechanical performance.

Table 4.4: Summary of methods used for fibre misalignment analysis at different voxel sizes.

	0.8 $\mu\text{m}$	2 $\mu\text{m}$	3.5 $\mu\text{m}$
Single fibre trajectory analysis	Successful	Unsuccessful	Unsuccessful
Structure tensor analysis	Successful	Successful	Unsuccessful





# 5

## CONCLUSION AND PERSPECTIVES

In this chapter, the concluding remarks of the thesis are presented. Section 5.1 summarises the key findings from **Chapter 2**, **Chapter 3** and **Chapter 4**. Section 5.2 discusses the main challenges encountered during the research and explores potential short-term directions for further investigation. Finally, Section 5.3 provides an outlook on the long-term impact of this work within the field of composite research.

## 5.1 INSIGHTS FROM THE WORK

The research conducted in **Chapter 2**, **Chapter 3** and **Chapter 4** builds on the understanding of microstructural features in unidirectional composite tapes. This work proposes a methodology for describing the hierarchical characteristics of the fibre reinforcement architecture, analysing the tape porosity network and its relationship with the fibre architecture, and exploring the reliability of extracting relevant features of interest at different observation scales.

In **Chapter 2**, the understanding of the microstructural organisation in unidirectional composites was advanced through the development of a novel methodology that introduces three innovative descriptors: differential tortuosity, collective motion, and length of the neighbourhood. These descriptors are designed to capture increasing levels of complexity in fibre architectures, ranging from single fibre deviations to group behaviours and network interconnectivity. The findings uncover organisational features that were previously unidentified, providing critical insights into the material's structure and its implications for both performance and modelling.

Differential tortuosity highlights deviations in the fibre trajectory from a perfectly straight longitudinal path, exposing variability in fibre alignment that can be related to both global misalignment and fibre loss of tension during tape manufacturing. The study identifies through-thickness gradients, or edge-core effects, where fibres near the edges of the tape exhibit greater tortuosity compared to those in the core. This phenomenon is hypothesised to result from manufacturing processes, such as mechanical tow spreading and impregnation, but could also be influenced by intrinsic dry tow architectural characteristics, such as its original level of fibre entanglement.

The concept of collective motion, inspired by models of synchronised movement in biological systems, quantifies the coherence of fibre group dynamics. Regions with well-aligned fibres demonstrate higher collective behaviour, while tape edge regions display less organised motion. This finding underscores the hierarchical organisation of fibres, which might reflect a different degree of microstructural disruption due to processing.

The length of neighbourhood (LON) descriptor measures the persistence of fibre contact within local neighbourhoods along the axial length of the tape. Results indicate in the tapes studied lower LON values for surface fibres, reflecting higher interconnectivity, whereas core fibres maintain stable associations over longer lengths. This highlights the variability in architectural cohesion across the material, and provides indications of characteristic lengthscales of fibre association throughout the material.

Interrelations between these descriptors provide additional insight into the hierarchical nature of tapes. In the materials investigated, fibres with higher tortuosity are less likely to exhibit collective behaviour or stable neighborhood associations, indicating more independent movement. Conversely, fibres with lower tortuosity tend to move coherently in groups and maintain longer-lasting interactions with their neighbours. However, different

combinations of parameters could be found in practice in the presence of different defect types. For example, the identification of a group of fibres with high collective motion and tortuosity at the edge of the tape could indicate a stray bundle. In contrast, a single meandering fibre migrating through the volume will only display high tortuosity but low collective behaviour. The specific combination of parameter values has, therefore, the potential to highlight different regimes of organisation. Such insight have the potential to guide defect classification and provide feedback in manufacturing process optimisation and insight into the mechanical performance of tapes.

These findings bridge traditional composite characterisation techniques with interdisciplinary approaches, enabling a deeper understanding of microscopic fibre arrangements. The study further emphasises the significant influence of manufacturing processes on fibre organisation. Moreover, the introduced descriptors provide a robust approach for future research on structural evolution, material processing, and advanced modelling techniques. By elucidating the hierarchical structure of UDCs, this work lays the groundwork for tailoring microstructures to meet specific application requirements and enhancing the accuracy of material performance predictions.

In **Chapter 3**, a novel methodology for characterising the pore networks in unidirectional composite prepregs is presented, linking porosity to fibre architecture. The findings reveal a significant interplay between pore distribution and fibre characteristics, highlighting the possible influence of local fibre differential tortuosity on porosity formation and propagation. They also highlight the formation of characteristic features, such as lenticular resin-rich regions, along the trajectories of fibres with high tortuosity and misalignment.

In the tape sample studied, the analysis shows that highly tortuous and misaligned fibres often correlate with regions of increased porosity, both at the surface and within the bulk of the material. Surface pores are found to exhibit greater variability and elongation compared to internal pores, with both types showing clustering at discrete locations. The study identifies a clear edge-core gradient in both pore distribution and tortuosity. Data-reduction strategies were used to correlate the parameters, showing how pore regions are more likely to be located in high-tortuosity regions, particularly in regions populated with meandering fibres. Meandering fibres are stray fibres characterised by high tortuosity and misalignment, which impose local ordering on the surrounding microstructure along their trajectory. The association between high-tortuosity regions and pore locations suggests that for the manufacturing process used, local fibre tortuosity and misalignment can create conditions that promote pore formation, possibly due to disrupted resin flow or microstructural inhomogeneities.

By quantifying the characteristic lengthscales of these features, the study demonstrates that both tortuosity and porosity propagate over hundreds, up to thousands, of micrometres along the fibre alignment direction. This insight is vital for understanding the microstructural organisation and for further optimising manufacturing processes. For instance, the presence of meandering fibres, which traverse the tape thickness, highlights mechanical weaknesses and potential fracture initiation points but also underscores the importance of controlling manufacturing steps such as dry tow spreading.

The thesis work suggests that complex relationships and interplays between microstructural features at the fibre and matrix level exist. Further research on impregnation processes in different manufacturing methods might help highlight the criticality of tortuous regions

in pore formation and evacuation, and vice-versa. The manufacturing methodology used for the tape analysed in this work has not been disclosed, which means the observations reported may not be directly applicable to tapes produced through different manufacturing processes. However, the broader implications of the insights gained might guide researchers in investigating 3D fibre orientation effects on permeability and the dynamics of pore removal in unidirectional composites. A deeper understanding of the interaction between pores and fibre architecture can inform the development of representative volume elements (RVEs) for more accurate material modelling, and the insight from the lengthscale analysis can provide guidelines for lengthscales of interest. This research also emphasises the need for broader material sampling, addressed in **Chapter 4**, and multi-scale studies to ensure comprehensive characterisation of tape microstructure and variability.

In **Chapter 4**, a multiscale approach to characterising microstructural variability in unidirectional carbon fibre-reinforced thermoplastic prepreg tapes is investigated. By employing different voxel resolutions, the research examines fibre misalignment linked to meandering fibre effects with both single fibre analysis as in the previous chapters and structure tensor analysis based on grayscale gradient. For four locations collected in the transversal direction of the tape (orthogonal to the main fibre alignment direction), the same region of interest captured at different magnifications was analysed. While the finest resolution ( $0.8\ \mu\text{m}$  voxel size, approximately 1/10th of the fibre diameter), allowed for detailed single-fibre trajectory analysis, the field of view is limited and scans are time-intensive. Scanning at coarser resolutions allows for the covering of larger material areas and provides a faster and more extensive sampling of the material. The question is, therefore, whether coarser resolution (hence, larger voxel sizes) can still allow the extraction of relevant fibre features of interest, such as meandering fibres, while filtering out artefacts related to porosity and tape contour variability.

The results from low voxel size measurements based on single fibre tracking were used as a reference ground truth to analyse misalignment outputs from larger voxel size measurements via structure tensor analysis. Since only the structure tensor data related to fibre voxels is of interest for this analysis, the results were further post-processed to remove non-relevant data related to matrix and air regions via a combination of image segmentation and filtering based on the anisotropy of local eigenvalues. These methods successfully reduce artefacts at critical locations, enhancing the precision of misalignment detection. This method effectively identifies regions of high fibre misalignment, including pronounced edge-core gradients, where misalignment tends to be higher near tape edges. However, as voxel size increases, the accuracy of structure tensor analysis declines due to lower image quality, which prevents accurate extraction of fibre misalignment effects.

The findings highlight the importance of optimising XCT imaging parameters for accurate material characterisation. The study demonstrates that inter-fibre spacing and heterogeneous morphology significantly impact resolution thresholds, especially as they approach the Nyquist limit for feature detection. In high-fibre volume fraction materials, like the one analysed, imaging at smaller voxel sizes can pose greater challenges in accurately identifying single-fibre effects if the inter-fibre spacing is not adequately sampled. In contrast, this issue might appear less pronounced in lower fibre volume fraction materials, where larger inter-fibre distances allow for imaging larger areas at lower magnification while still resolving individual fibres effectively.

## 5.2 DISCUSSION AND SHORT-TERM PERSPECTIVES

### 5.2.1 CAPTURING FEATURES OF INTEREST

#### IMAGING ARTEFACTS AND SEGMENTATION BOTTLENECKS

Accurate characterisation of composite microstructures remains a critical challenge, particularly when resolving features of interest within high-fibre volume fraction materials. Limitations in imaging and segmentation techniques, along with artefacts, low contrast between constituents, and noise in scans, can compromise data quality. Insufficiently reliable data may lead to misinterpretation or misrepresentation of the material's true characteristics, obscuring critical features and hindering efforts to extract meaningful insights from composite materials such as carbon fibre/thermoplastic matrix systems.

In XCT scans, artefacts frequently occur at phase boundaries where grayscale intensity values for matrix, pores, or fibres are in close proximity. This challenge is exacerbated by the low contrast in materials like carbon fibre composites, making it difficult to distinguish between individual fibres or to resolve fibre spacing, which is critical feature that dictates segmentation accuracy as highlighted in **Chapter 4**. Although binning has been used to improve image quality (as explored in **Chapter 2**), it limits the practicality for subsequent analysis since the field of view is further reduced.

Advanced segmentation methods, including machine learning-based techniques, have shown promise in overcoming these issues. For instance, Trainable Weka Segmentation (TWS) was used in this work with improved phase distinction compared to classical thresholding approaches like Otsu's method [46]. Machine-learning methods have an improved ability to adaptively mitigate artefacts in intensity variations regions near phase boundaries, enabling more reliable segmentation of complex microstructures. The performance of TWS is, however, limited since it is not informed on the shape of the features to be segmented, and it was applied in this work as 2D segmentation on single slices and not in the 3D space. To bridge this gap and further improve the segmentation capacity in high-resolution scans, methods such as recognising star-convex polygons, originally designed for cell identification in biology [93], could be effective in recognising circular fibre cross-sections in 2D transversal slices of the image volume. Routes to bring the segmentation to its full potential by leveraging the 3D information are available from medical imaging, where problems of segmentation of fibrous material have been addressed [94, 95].

Unidirectional composite tapes present unique segmentation challenges compared to fully consolidated laminates due to their irregular contours and porosity. While consolidated laminates generally exhibit smoother phase boundaries, tape datasets often contain artefacts at these irregular interfaces. Recent efforts to enhance segmentation accuracy include deep learning approaches for pore segmentation in filament-wound composites [96] and contour extraction based on commercial software such as Photoshop, which was employed by Emtiaz et al. in the study of additively manufactured continuous carbon fibre thermoset composites [97]. As applied in **Chapter 4**, anisotropic filtering has been used to address such segmentation difficulties in lower-resolution measurements. However, improperly tailored filtering can introduce additional artefacts, necessitating precise parameter optimisation to preserve valuable data. These challenges underline the need for improved grayscale segmentation methods to bypass artefact-related issues.

A different route to improve the quality of the image features extracted would be to

enhance the image quality to be processed. For example, super-resolution techniques using CycleGAN models show promise for enhancing the quality of noisy CT scans. By improving resolution and reducing noise, these methods have increased the accuracy of detecting microstructural events such as fibre breakage in time-lapse XCT measurements [98, 99].

### FIBRE PATH EXTRACTION

The fibre reconstruction approach employed in this work, Trackmate [47], leverages Fiji, a free and open-source platform [44]. The tracking method utilised a Linear Assignment Problem approach, originally developed for the study of live-cell time-lapse sequences. This method has proven effective for extracting trajectory information in well-segmented samples and unidirectional microstructures with minimal fibre misalignment.

The fibre tracking method shown in this thesis was built around the assumption of a principal direction of fibre alignment, which introduced limitations in analysing more complex fibre architectures. For example, in the case of highly misaligned fibres with visibly ovalised transversal cross-sections, Trackmate exhibited reduced performance and increased error rates. As highlighted in **Chapter 3**, this fibre tracing method struggled to achieve perfect reconstruction for fibres with significant deviations from the average alignment, requiring manual tracing for correctly representing selected meandering fibres. Complementary methodologies such as the one proposed by Sosa-Rey et al. [82] to reconstruct fragmented fibre information might be useful in future work to increase the accuracy of the extracted fibre trajectories and the calculated 3D parameters.

Direction-agnostic approaches, such as those looking at the 3D voxel distribution as in the commercial software for image analysis Avizo, GeoDict, VGStudio Max [22], offer improved capability for reconstructing intricate structures. In particular, for the case of fibres, cylindrical template-matching approaches can be used to follow fibre trajectories. The downside of the method is the need for correct calibration of the multiple fitting parameters available for template matching. The approach has, however, the capability to address the case of discontinuous or recycled fibre architectures with higher intrinsic variability, where principal-direction approaches may fall short.

## 5.2.2 MICROSTRUCTURAL DESCRIPTION AND ANALYSIS

### DESCRIBING THE FIBRE MICROSTRUCTURAL COMPLEXITY

The descriptors of variability proposed in this work provide a novel framework for studying 3D microstructural complexity. To further extend the capability of accurate description of three-dimensional effects of composite materials and further explore feature relationships at a microstructural level, these descriptors could be studied in conjunction with more traditional metrics such as fibre volume fraction [100, 101] and nearest neighbour distance and angle probability distribution [102]. The application of fibre cluster analysis, based on triangulation and neighbour distance criteria, might further clarify rules of the microstructural organisation [84, 85, 97].

The definition of differential tortuosity proposed in this work is tailored to the case study of unidirectional composites. Different tortuosity definitions might be more suitable in the more general case of fibre architecture with no reference principal alignment direction, as in randomly oriented discontinuous composites. For instance, Nelms et al.

adapted our definition of differential tortuosity by calculating it with respect to a reference length along the mean misalignment direction of each fibre in their work on compression micromechanics in composite material [86]. Additional parameters describing single fibre trajectories, such as fibre curvature and wave amplitude [103], can be included.

For collective motion effects, fibre path similarity analysis and dynamic time warping might constitute additional tools for characterising spatially linked effects within the material. Time warping, in particular, has been used to analyse individual animal trajectories during herding [104]. While the current definition of collective motion refers to bundling effects linked to coherent fibre movement throughout the material volume, different descriptors of neighbourhood interactions could be derived. As an example from the work of Houriet et al. on flow-inspired anisotropic patterns in 3D printing of liquid crystalline polymers [105], similar descriptions to vortex patterns could be associated with certain fibre organisation effects.

From a perspective of quantification of characteristic lengthscales for unidirectional tapes, in **Chapter 2** and **Chapter 3**, different approaches have been proposed both based on single fibre neighbourhood analysis and on the propagation of 3D microstructural descriptors. Greater emphasis was given in this work to lengthscales and feature propagation analysis along the longitudinal fibre alignment direction, rather than across the transversal direction. The data acquired in **Chapter 4** qualitatively highlights a high variability of features across the transversal direction of the tape studied. Future work should quantify microstructural propagation lengthscales in the transversal direction and the possible scale of periodicities in the microstructure linked to the manufacturing process.

### PORE NETWORK ANALYSIS

The challenge of three-dimensional pore network characterisation is broadly approached in geological science, energetic material and biology. Jones et al. used several parameters to characterise pore networks. The minimum radius of all covering spheres between two junctions in the medial axis can provide insights into the constrictions of the network. Coordination Number was employed to determine the number of throats connected to each pore, offering a measure of connectivity within the network. Finally, the Accessible Pore Radius was measured as the radius of the largest sphere that can penetrate into a pore from the scaffold periphery, indicating the accessibility of the pore space [106]. Holzer et al. highlighted the importance of using tortuosity analysis to study pathways in porous media in relation to diffusion and permeability [107]. Lagadec et al. applied the Euler–Poincaré Characteristic, a topological invariant, to study connectivity within pore networks in lithium-ion battery components, drawing a direct link to their performance [108]. Alatrash et al. employed fractal dimension and Distance Ordered Homotopic Thinning algorithm to quantify the irregularity and complexity of pore structures in carbonate samples [109]. Lisitsa et al. used persistent homology for topology-based characterisation of pore space changes due to chemical dissolution of rocks [110].

The use of these descriptors, combined with fibre trajectory analysis, could be leveraged in monitoring the temporal and spatial changes of pore networks in unidirectional tapes and laminates, with a focus on transitions from well-defined structures to degenerate or collapsed states. Potential applications to explore complex phenomena associated with pore evolution during processing, such as tape formation and deconsolidation or consolidation events, could bring further understanding into the material behaviour.



## MEANDERING FIBRE ANALYSIS

Meandering fibres in UDCs are crucial microstructural features with potentially significant implications for material properties such as longitudinal stiffness and compression performance. These fibres, characterised by their tortuous paths and high degrees of misalignment, have been observed to induce local microstructure reorganisation, such as the formation of resin-rich 'lenticular spaces' which can propagate hundreds of micrometres through the composite longitudinal direction, as shown in **Chapter 3**, and should be further quantified in future work. Possible strategies based on local fibre volume fraction considerations or on the study on the fibre neighbourhood analysis via Voronoi tessellation as in 3D printed fiber-reinforced polymers from microscope images by Li et al. [111] might help to quantify further induced resin-rich areas effects linked to meandering fibres.

From the hypothesis of meandering fibres being the result of fibre breakage, in-line measurement of broken fibres on the surface of tapes during the tape manufacturing process could be possible through integrated laser measurement units [76]. Further characterisation routes for identifying meandering fibres travelling within the thickness of prepregs reinforced with conductive fibres, such as carbon fibres, could include electrical conductivity measurements using six-probe methods [75] and Eddy current testing [77].

From a modelling perspective, incorporating criteria that capture local collective motion and reorganisation around these fibres can provide a more nuanced understanding of their impact on mechanical performance. Such effects might be lost in materials with lower fibre volume fractions, where local fibre migration might have less influence on neighbourhood reorganisation.

### 5.2.3 MULTISCALE ANALYSIS

Multiscale analysis of unidirectional composites offers significant opportunities to advance the statistical evaluation of their variability, with the potential of identifying a unique fingerprint of a given tape and informing on defect characterisation for quality control. While high-resolution investigations remain essential for capturing single-fibre effects, zooming out to larger scales is necessary to achieve a more holistic understanding of microstructural variability. High-resolution images also imply long scan times to acquire information over limited volumes of material. Therefore, efforts to identify mesoscale parameters that reflect microscale phenomena would be highly beneficial.

The second-order structure tensor was used to extend the capability of capturing meandering fibre effects in larger observation scales. Further studies should look into further optimisation of the structure tensor results via further understanding of the influence of filtering at a 3D level. The analysis of in-plane transversal cross-section angle information, which at  $0.8 \mu\text{m}$  voxel size from single fibre analysis can be successfully extracted for collective motion analysis, is for now discarded in the structure tensor approach based on possible inaccuracies in its calculation in a highly unidirectional microstructure imaged at low resolution. Determining such local orientation at a multiscale level might enable the analysis of the propagation of bundling phenomena in larger material volumes, adding to the material understanding.

The option of leveraging segmentation results from high-resolution scans to train machine learning segmentation of low-resolution scans and bridge the information gap should also be explored. Possible examples of such workflow come from both the medical



field [112] and from the composite fields, where segmentation data based on high-resolution Synchrotron CT scans as training for a 3D CycleGan approach to enhance lower resolution CT scans [98].

The analysis of misalignment data derived from structure tensor analysis follows the common approach in the literature to evaluate histograms of the full range of detected misalignment values for comparative studies. However, a more convincing comparison of the reliability of local misalignment values at a 3D level within the same regions of interest could be performed, either voxel-by-voxel or via max-filtering methods. While at the lowest resolution explored in this work ( $3.5\text{ }\mu\text{m}$  voxel size) fibre locations and misalignment are not recognisable anymore, data on pore network information could still be extracted in future work. For materials where strong correlation between pore locations and high-tortuosity and misalignment fibre locations is validated with a method such as the one proposed in **Chapter 3**, knowledge of pore network architecture might be leveraged as a 'tracer' of microstructural effects at a fibre level and enable assumption of feature propagation over larger material volumes at low resolutions. While lower-resolution XCT scans might help bridge the gap in the understanding of spatial propagation of microstructural features such as meandering fibres and pore networks, the understanding of local fibre effects at high resolution over large material areas is still restricted by the experimental barrier of long scan times and challenging segmentation and data processing. Establishing an understanding of the number and spatial distribution of scans that can provide statistically significant information on the microstructure is still an open question, which potentially requires extensive data acquisition and processing, and might have to be tailored for different materials to account for their differences in variability.

A potential approach to bridging the gap between different observation scales and the challenge of large-scale data acquisition is to train numerical models to identify 3D microstructural variability descriptors—derived from XCT data—using 2D information. Optical microscopy, a widely accessible 2D technique, enables large-area sampling of fibre neighbourhood descriptors such as distance, angle, local fibre volume fraction, and local ordering effects. However, it lacks the ability to extract complex hierarchical features, such as those proposed in this work. A model capable of translating transversal cross-sectional data into probabilistic predictions of local 3D microstructural descriptors could enhance the value of optical microscopy, enabling the upscaling of microstructural investigations in unidirectional composite materials, for example, through the prediction of likely locations of meandering fibre corridors, and their propagation across the transversal cross-section.

#### 5.2.4 PROCESS-STRUCTURE-PROPERTY RELATIONSHIPS

In this work, the focus has been on the development of methodology for analysing features at fibre architecture and pore network levels. In this scope, linking architecture features to the microstructure formation mechanism and to the processability and performance of the final part is left for future work. By controlling the manufacturing parameters, it might be possible to precisely influence the microstructural variability and propagation of features such as meandering fibres. Accurate microstructural designs might enable specific properties. For example, the work of Amacher et al. on thin-ply composites suggests possible size effects involved in material property optimisation [2].

The conclusions highlighted in this thesis work on possible relationships between fibre

architecture effects and pore distribution are limited to the case study analysed. They should serve as a methodology approach for the study of interrelations and propagation of features. Different manufacturing routes, such as tape impregnation method or fibre tension parameters, might lead to different inter-relation between features. Such effects should be taken into account to critically evaluate the results shown.

#### **POROSITY EVOLUTION AND INTERPLAY WITH THE FIBRE ARCHITECTURE**

A possible validation of the hypothesis that meandering fibres may originate from fibre breakage—and that pore locations might be linked to this phenomenon as well—can be found in the research by Awenlimobor et al. [113]. Their study highlights the tendency for pore nucleation at fibre ends during 3D printing of discontinuous carbon fibres embedded in an Acrylonitrile Butadiene Styrene (ABS) matrix. This underscores the critical importance of precise manufacturing control in the early stages of tape production to minimise defects that could significantly affect the final material properties.

In the current method for defining pore space in tapes, as presented in **Chapter 3**, surface porosity is characterised using a global boundary that captures the variability across a fixed length (500  $\mu\text{m}$  in this case). This approach assumes that mesoscale variability in the tape contour, such as rotation or bending, is negligible. However, this assumption is not universally applicable. A more generalised approach incorporating a locally defined tape boundary would be valuable for addressing surface variability across larger material volumes in future studies.

To add on the insights in **Chapter 3** on possible links between fibre tortuosity and pore network in unidirectional composite tapes, further indications on relationships between porosity and fibre architecture characteristics in unidirectional composites were explored by Emtiaz et al. [97]. Their study identified a connection between pore formation and fibre clustering during the impregnation of carbon fibres with epoxy resin in the additive manufacturing of continuous carbon fibre thermoset composites. These findings further point towards complex interrelations between fibre architecture and porosity network in composite materials, underscoring the need for precise manufacturing control to ensure optimal microstructure formation.

Additional relationships between fibre architecture and porosity may emerge when examining how porosity evolves at the laminate level during crucial manufacturing stages like tape deconsolidation. Additional research is necessary to fully comprehend how these processing stages affect the final performance of the material.

#### **EDGE-CORE EFFECTS**

Edge-core effects for both fibre descriptors and pore distribution were consistently observed throughout this thesis. These effects reveal greater microstructural disruption at the tape surfaces compared to its core. This phenomenon may be linked to microstructure formation mechanisms during tape spreading, with the extent of frictional forces and the dry tow architecture influencing the depth of disruption. The through-thickness microstructure may appear homogeneous for tapes with a thickness smaller than the disrupted depth, as no discernible edge-core gradients can form. Studying the varying degrees of tape spreading provides valuable insights into how this process shapes microstructural architectures and contributes to edge effects. Furthermore, such investigations may uncover the microstructural origins behind the enhanced performance of thin-ply tapes in composite applications,

offering a deeper understanding of the interplay between manufacturing processes and material properties.

### **PREDICTIVE MODELING AND SIMULATION**

Accurate microstructural characterisation is essential for predictive modelling of unidirectional composite tapes to assess their mechanical performance, damage evolution, and manufacturability. A key challenge in this field is defining a representative microstructure, as the accuracy of simulations depends on how well the microstructural features are captured. Advanced characterisation techniques should therefore facilitate the identification of key statistical features that can be incorporated into computational models to improve predictive accuracy.

A crucial aspect of microstructural modelling is determining statistically representative volume elements (RVEs) that accurately reflect the variability of the material. These RVEs serve as computational domains where key microstructural features are retained to ensure realistic mechanical behaviour. While coarse homogenised microstructural data may be sufficient for predicting stiffness, failure simulations—such as those involving crack propagation or fibre breakage—require a more detailed representation of local defects. Features such as meandering fibres, bundling effects, and local voids can strongly influence failure behaviour. Therefore, an important consideration is determining the minimum number of samples needed to capture the statistical variability of a unidirectional tape, ensuring that the extracted dataset provides a reliable foundation for material modelling.

Several computational methods have been explored for generating artificial microstructures, each offering different advantages depending on the material system. For example, Guo et al. employed Generative Adversarial Networks (GANs) to generate 2D transversal cross-sections of composite materials, successfully replicating resin-rich regions [114]. Other studies have focused on statistical approaches, where microstructures are generated based on descriptors of fibre distributions and matrix properties [115, 116]. However, these methods are largely limited to materials with low fibre volume fractions, restricting their applicability to high-performance composites.

Beyond composite materials, methodologies from other disciplines could be adapted for microstructural synthesis. Perlin noise, a technique commonly used in texture generation, has been applied in medical imaging studies to simulate cancer-specific architectures [117]. Similar approaches could be explored to generate synthetic composite microstructures with controlled heterogeneity. Another promising approach is MCRpy, a computational framework developed for material research [118–121], which has recently been used to generate artificial metal microstructures [122]. Extending MCRpy to composite materials could enable the rapid synthesis of statistically accurate microstructures for predictive modelling.

Extrapolating microstructural features for unexplored manufacturing conditions is another key challenge, particularly when experimental data are limited. Machine learning and generative models offer solutions by learning the statistical distributions of existing microstructures and predicting variations under new conditions. Integrating these models with experimental data could aid in optimising manufacturing processes, enhance material design, and improve failure prediction, reducing reliance on costly trials.

### 5.3 LONG-TERM PERSPECTIVES

This thesis provides a new perspective on studying and designing composite tapes, with a focus on fibre architecture and pore networks. By integrating high-resolution 3D data from X-ray micro-computed tomography, the work establishes a hierarchical approach to microstructural analysis, allowing for the quantification of intricate features that influence composite performance. Beyond advancing fundamental understanding, these methodologies have direct applications in quality control, defect mitigation, and process optimisation, offering insights relevant to aerospace, automotive, and renewable energy industries.

One key contribution is the potential to track microstructure evolution throughout manufacturing stages. Understanding how fibre alignment, tortuosity, and pore networks develop under different processing conditions can help identify critical defect formation points, improving manufacturing reliability. Additionally, this approach provides a framework for studying dynamic material behaviours, such as deconsolidation, where fibre-matrix interactions and porosity changes influence final composite properties.

Future research can build on these findings by exploring application-driven behaviours, such as compression failure mechanisms, where localised microstructural features contribute to kink band initiation and propagation. Similarly, tailored fibre architectures could support the design of morphing structures, enabling adaptable mechanical responses in aerospace applications. In hydrogen storage systems, analysing crack networks in relation to fibre and pore structures could enhance material safety and reliability.

The development of representative volume elements (RVEs) tailored to specific microstructural features represents another important avenue for future work. Accurate modelling of composites requires information on complex attributes such as fibre tortuosity, pore clustering, and interconnectivity. Furthermore, generating artificial microstructures informed by experimental data could enable virtual testing of composites, significantly accelerating the design and optimisation process. By addressing these areas and capitalising on the methodologies developed, future research can deepen our understanding of microstructure-performance relationships, optimise manufacturing processes, and expand the applicability of unidirectional composites in advanced engineering fields. These efforts promise to drive innovation and enable the development of tailored high-performance materials.



## APPENDIX: PORE FRACTION ACROSS SUB-VOLUMES

This appendix refers to **Chapter 3**. In this Appendix, the pore fraction distribution for the full scan volume is shown. Figure A.1 shows the variation of pore fraction on the  $xy$  plane for the six sub-volumes identified. Figure A.2 and Figure A.3 show the variation of pore fraction on the  $xz$  plane. Figure A.4 shows the variation of pore fraction on the  $yz$  plane.

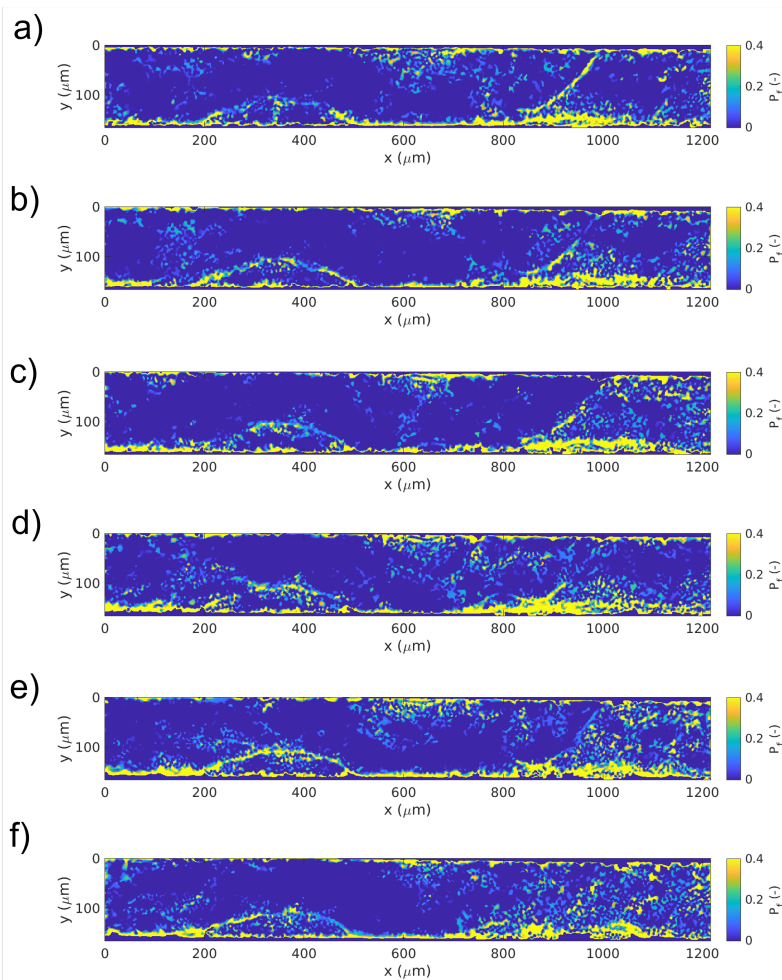


Figure A.1: Pore fraction maps for the  $xy$  plane for a) Sub-Volume 1; b) Sub-volume 2; c) Sub-volume 3; d) Sub-Volume 4; e) Sub-Volume 5; f) Sub-Volume 6.

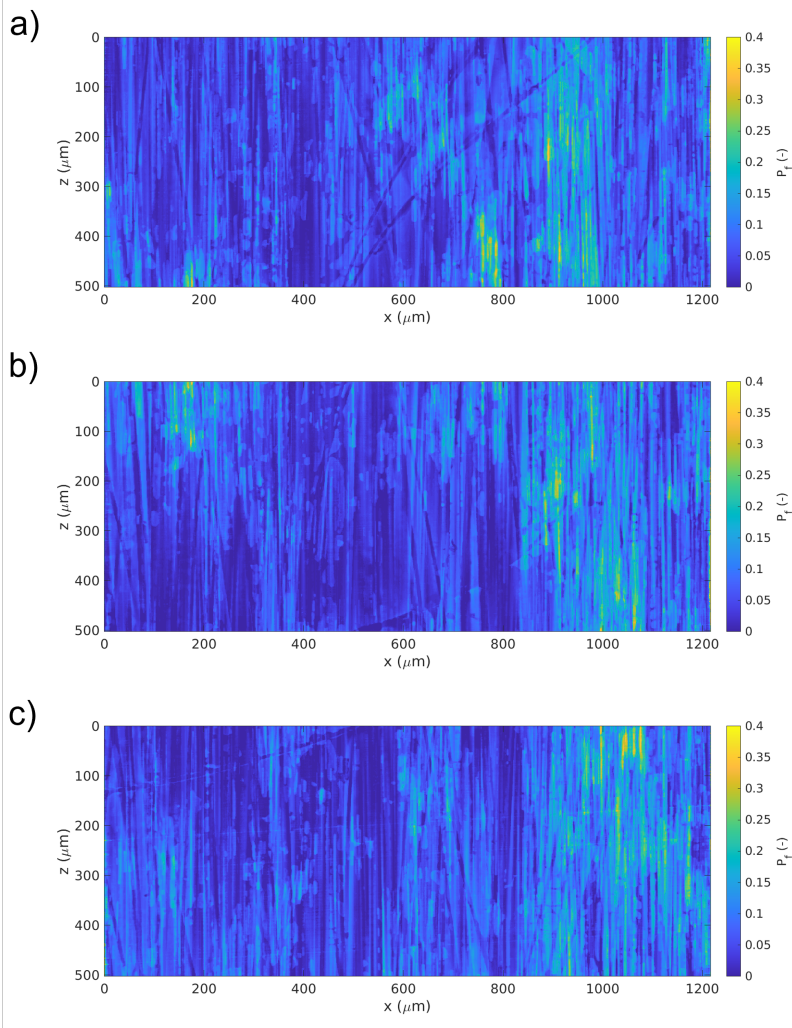


Figure A.2: Pore fraction maps for the  $xz$  plane for a) Sub-Volume 1; b) Sub-volume 2; c) Sub-volume 3.



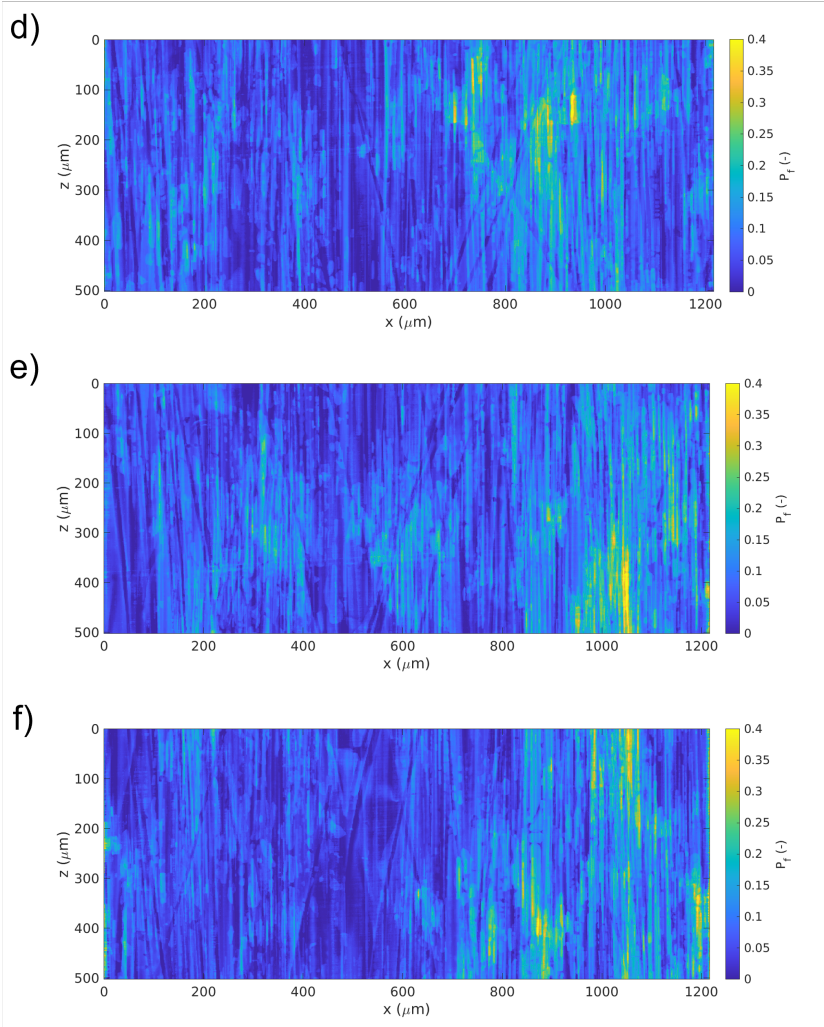


Figure A.3: Pore fraction maps for the  $xz$  plane for d) Sub-Volume 4; e) Sub-Volume 5; f) Sub-Volume 6.



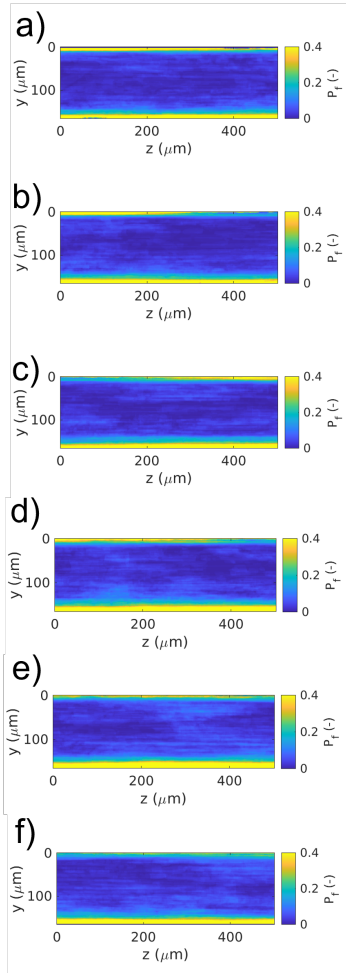


Figure A.4: Pore fraction maps for the  $zy$  plane for a) Sub-Volume 1; b) Sub-volume 2; c) Sub-volume 3; d) Sub-Volume 4; e) Sub-Volume 5; f) Sub-Volume 6.



# B

## B

### APPENDIX: STATISTICAL ANALYSIS OF INTERNAL AND SURFACE PORE GEOMETRY

This appendix refers to **Chapter 3**.

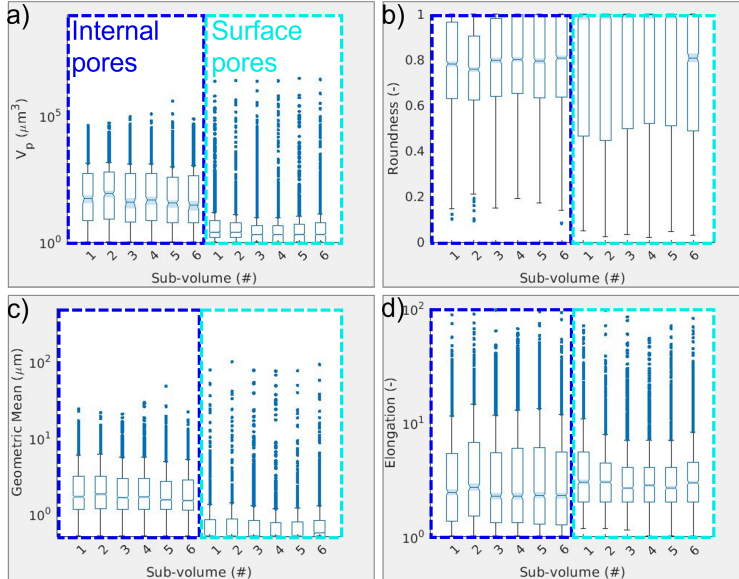


Figure B.1: Boxplots for individual sub-volumes for internal and surface pores a) pore volume b) roundness c) geometrical mean d) elongation.

Figure B.1 shows for surface and internal pores the values of median, interquartile

**B**

range and full range. The statistical analysis in Figure B.1 show significant difference in all parameters considered. The volume of surface pores is shown to be lower than for internal pores in Figure B.1a). The effect is partly due to the definition of surface pores through the sub-volume boundary, which can isolate small pockets of volume on the tape edge. Figure B.1b) shows that surface pores are statistically more round than internal pores. The Geometrical Mean is statistically lower for surface pores as in Figure B.1c), however the range of the parameter is larger than for internal pores. Elongation tends to be similar for internal and surface pores, however internal pores tend to have a larger interquartile range as shown in Figure B.1d).

# C

## C

## APPENDIX: TORTUOSITY MAPS ACROSS SUB-VOLUMES

This appendix refers to **Chapter 3**. In this Appendix, the tortuosity maps relative to the  $xy$  plane are shown for all sub-volumes in Figure C.1.

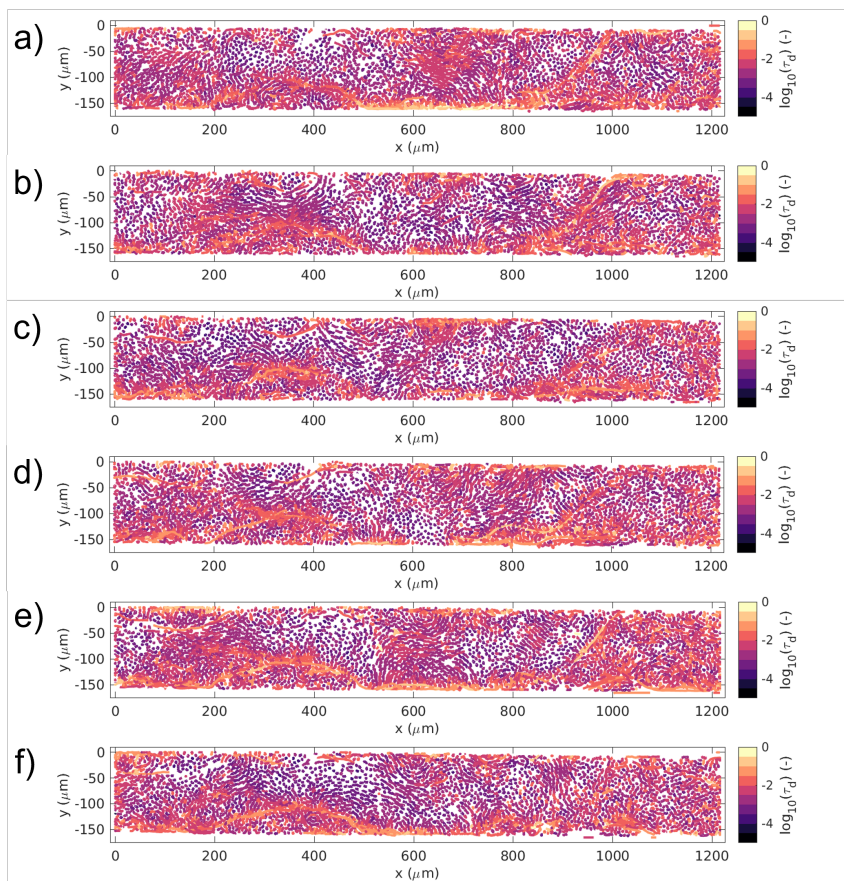


Figure C.1: Tortuosity maps for a) Sub-Volume 1; b) Sub-volume 2; c) Sub-volume 3; d) Sub-Volume 4; e) Sub-Volume 5; f) Sub-Volume 6.

# D

## APPENDIX: SEGMENTED REPRESENTATION OF INTERNAL AND SURFACE PORES

**D**

This appendix refers to **Chapter 3**. Figure D.1 and Figure D.2 show the segmented view of internal and surface pores for three  $xz$  cross-sections of the tape analysed. The pore direction aligns with the main fibre direction. At a cross-sectional level, pores within the same class can appear fragmented along the  $z$  direction, as if following each other in the  $z$  direction in close proximity. This feature might not reflect their three-dimensional development, as might be part of the same connected region.

Proximity of pores in the  $z$  direction is shown to occur within the same pore class, but also between internal and surface pores, and it can be observed in multiple instances in the figures shown. Close alignment of internal and surface pores might indicate degeneration of surface pores in internal pores during tape manufacturing.

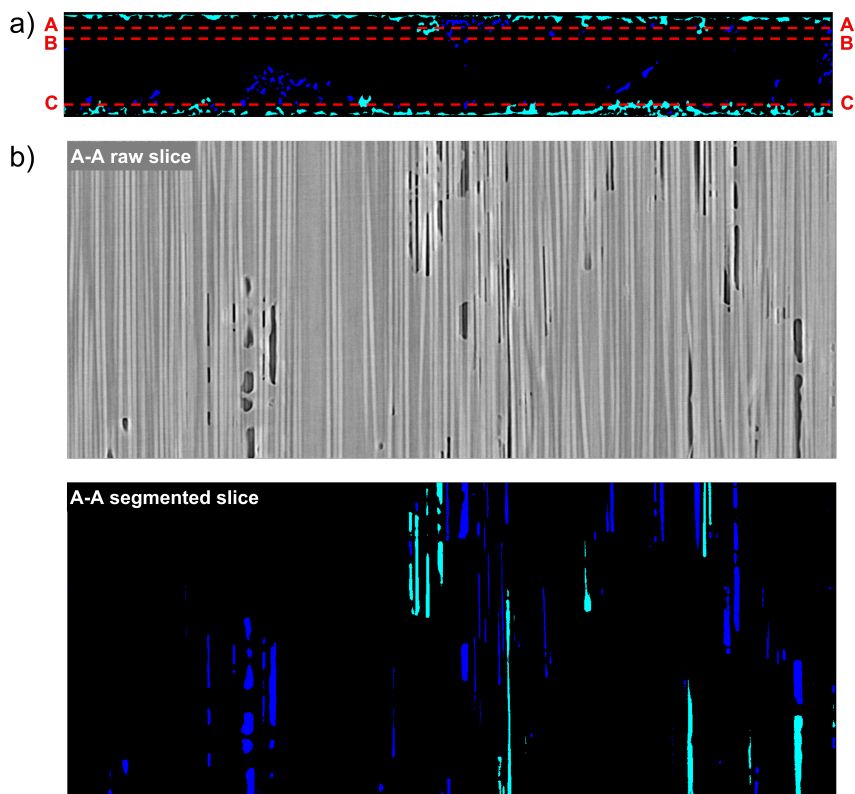
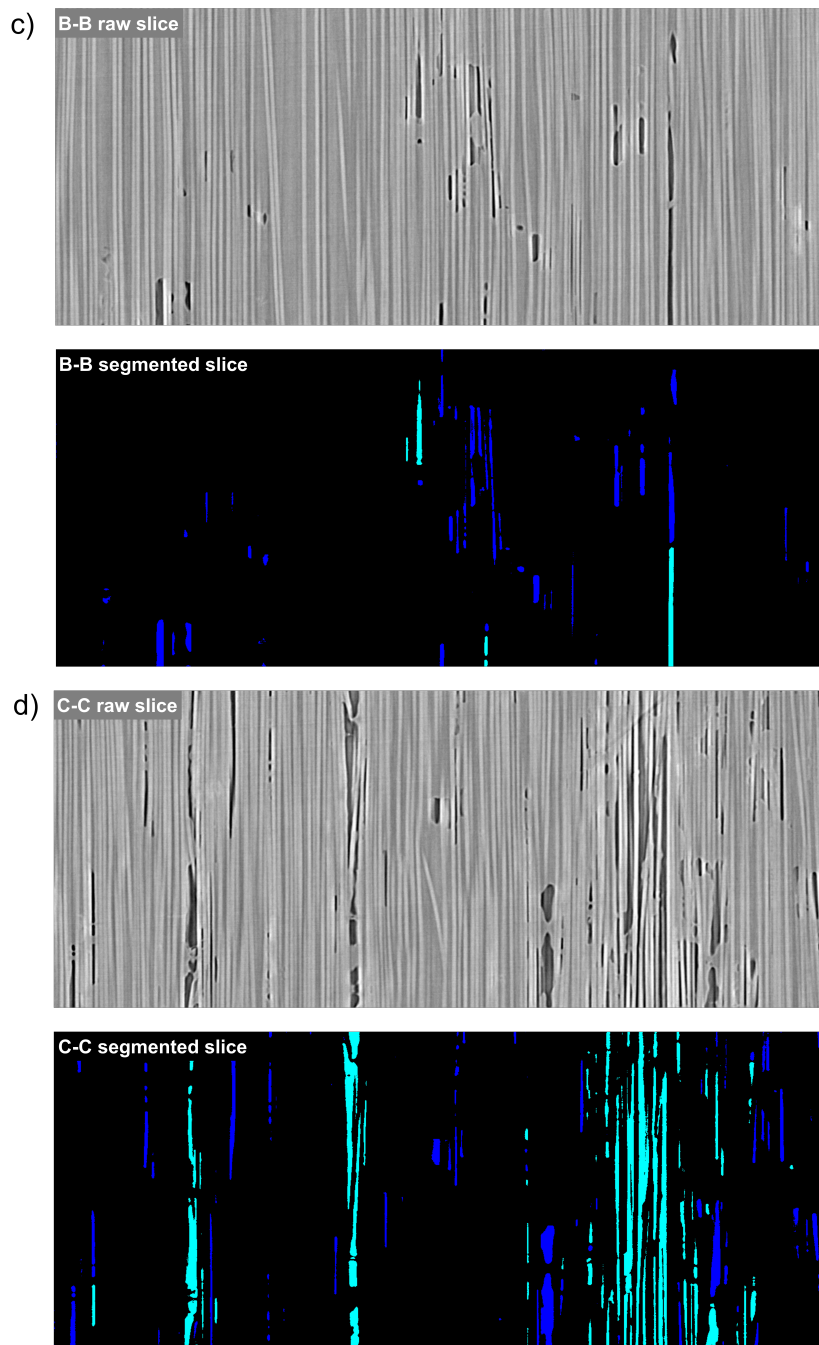


Figure D.1: a) Segmented slice of pores on the  $xy$  plane. Internal pores are highlighted in light blue, while surface pores are shown in cyan. Horizontal dashed lines indicate the location of the subsequent  $xz$  slices; b)  $xz$  slice A-A, shown as raw and segmented.





D

Figure D.2: Continuation of Figure D.1, internal pores are highlighted in light blue, while surface pores are shown in cyan c)  $xz$  slice B-B, shown as raw and segmented; d)  $xz$  slice C-C, shown as raw and segmented.



# E

## APPENDIX: MANUALLY TRACKED MEANDERING FIBRES

This appendix refers to **Chapter 3**. Manually tracked meandering fibres in Sub-Volumes 1 to 5 have been here shown projected on the  $xz$  plane in Figure E.1 and Figure E.2. No fibre was manually tracked in Sub-Volume 6. The colours used to label the fibres correspond to the legend used in Figure 12 of the main manuscript.

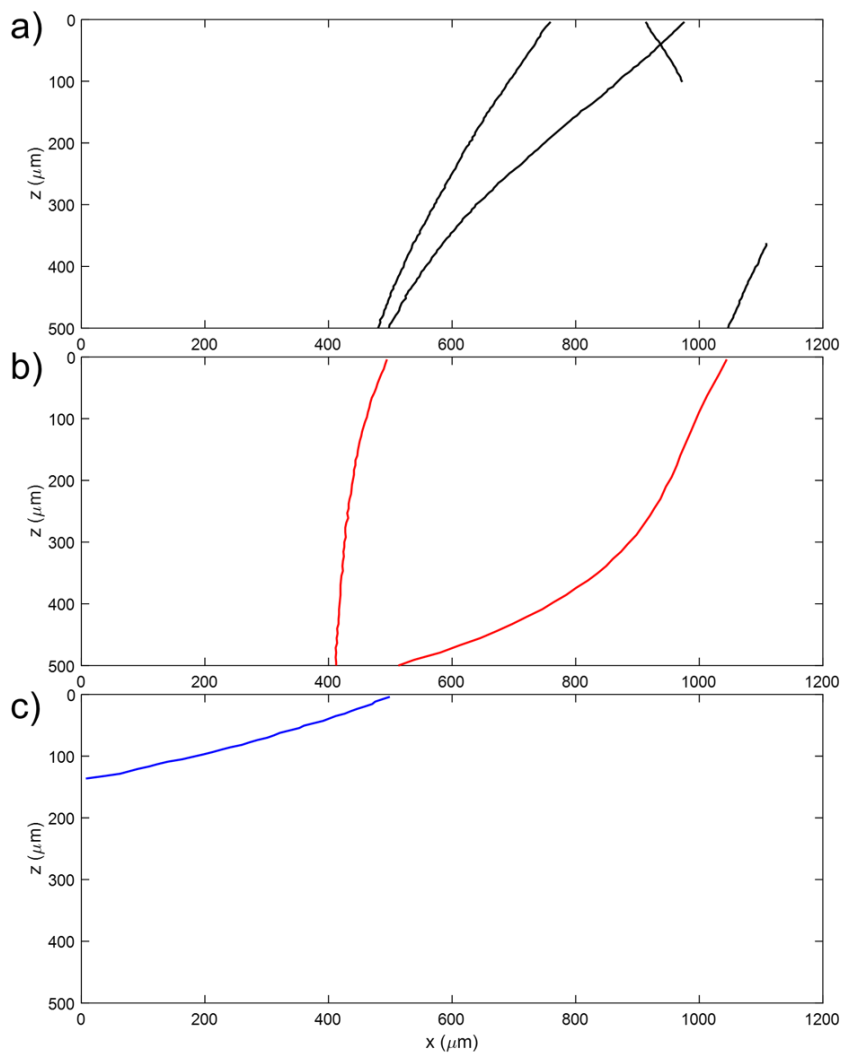


Figure E.1: Manually tracked meandering fibres projected on the  $xz$  plane for a) Sub-volume 1; b) Sub-volume 2; c) Sub-volume 3.

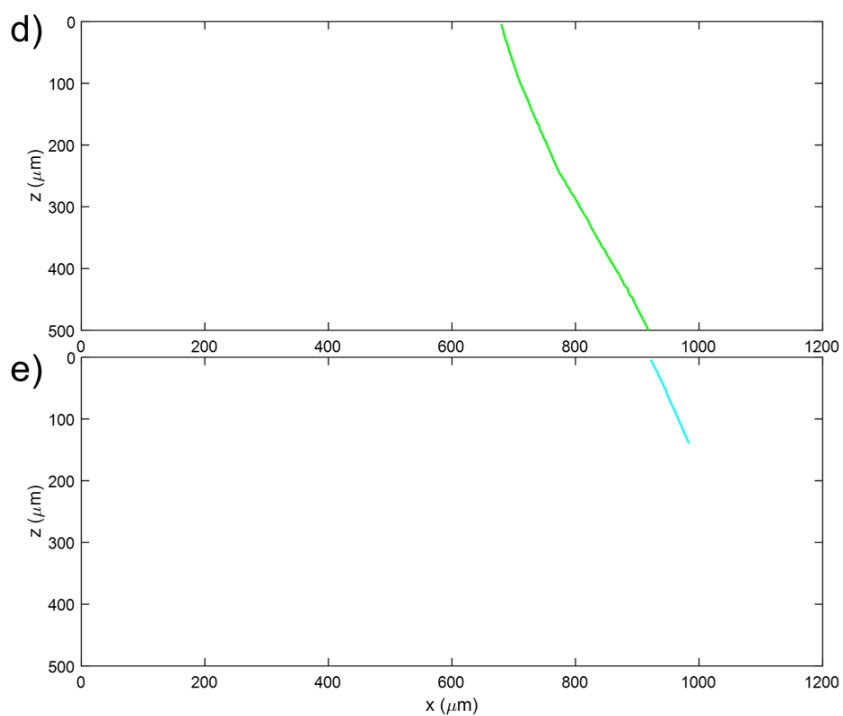
**E**

Figure E.2: Manually tracked meandering fibres projected on the  $xz$  plane for d) Sub-Volume 4; e) Sub-Volume 5.



# F

## APPENDIX: DETERMINATION OF A THRESHOLD OF HIGH nSD SIMILARITY

### F

This appendix refers to **Chapter 3**. A reference range of nSD values to determine high-similarity between datasets was constructed based on the porosity distribution. Four subsets of the tape porosity were extracted in such a way that they had the same scan length of the total scan, and a square cross-section on the  $xy$  plane with side equal to the thickness of the scan space. The regions are extracted one beside the other, starting from the leftmost side of the tape, and are shown in Figure F.1a). Since it is expected in a unidirectional composite a greater alignment of features in the fibre orientation direction would lead to much greater correlation than across the width, the four subsets are assumed to have low similarity. The possible presence of periodicity of the pore microstructure across the width is here neglected. The overall distribution of nSD values conducted on all subset combinations (but not with themselves) are shown in Figure F.1 as an orange line, which shows a significant shift towards higher nSD values compared to the results of similarity of the tape with itself shown in blue.

It should be noted that some features within the subsets might still show similarity across them, such as higher porosity at the top and bottom edges. This is reflected in the reference distribution having lower values than  $nSD = 0.8$ , with a tail of values below 0.5. However, the majority of the voxels compared in the subsets show a higher extent of deviation compared to the case study, confirming that the choice of subsets can be representative of a lower extent of similarity. A value of  $nSD = 0.5$  was therefore defined a upper boundary indicator of the high similarity range. At that value, half of the spatial distribution of the parameter considered is retained.

Collateral work uses similarity studies via cross-correlation equations to study spatial propagation of features [65, 66]. Such studies refer to values of cross-correlation of 0.1 in a value range of  $[-1, 1]$ , with 1 corresponding to perfect correlation. The chosen threshold value of  $nSD = 0.5$  therefore appears close to the criteria highlighted in literature.

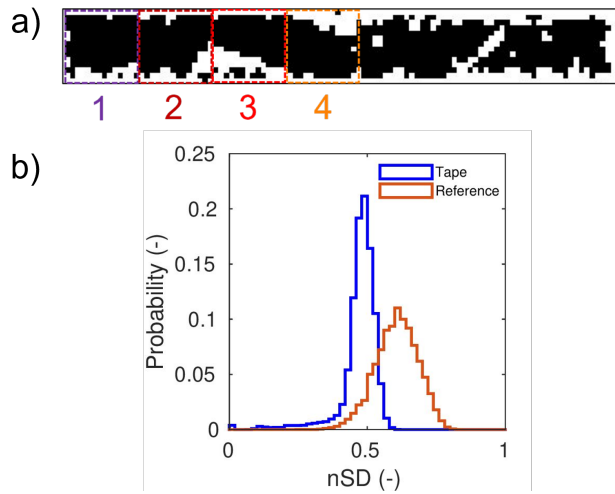


Figure F.1: a) Subsets considered for the reference; b) Similarity study of the scan volume with itself (blue line) and among subsets (orange line).



# G

## APPENDIX: SENSITIVITY ANALYSIS ON THE KERNEL SIZE FOR MAX-FILTERING

This appendix refers to **Chapter 3**. The choice of different kernel sizes and shapes can help modulate the scale of feature observation, and the results of the similarity analysis. Since the degree of homogenisation induced by max-filtering is a function of the kernel used, in Figure G.1 different kernel sizes were compared. The kernels used are cubic, with sides ranging from 5 voxels (about half a fibre diameter) to 30 voxels (about three times the fibre diameter).

For the correlation of tortuosity and pores, increasing element size causes distributions to move towards slightly higher tortuosity values, which can be related to the increasing level of homogenisation in the max-filtering operation. Furthermore, consistently for all the kernel sizes used, the results show a slight increase in the differences between the range of tortuosity where pores are found compared to pore-free regions, showing that the result reported in the main manuscript for a kernel size of 15 voxels is still representative with the element sizes here used.

Concerning the length of propagation of the pore and tortuosity distributions obtained through the similarity analysis, different kernel sizes appear to highlight different features.

At the smallest kernel size of 5 voxels, the propagation lengthscale for pores is limited within the 120  $\mu\text{m}$  range, highlighting more local similarity effects. The max-filtering, in this case, still applies limited homogenisation and highlights more local distinct pore structures, which might not correlate in the long range. With an element size of 10 voxels, the lengthscale captured for pores increases, reaching regions with high similarity values of around 300  $\mu\text{m}$ . At 15 voxels, the propagation length further increases (result shown in the main manuscript), indicating that pore features tend to propagate beyond the single sub-volume analysed at that scale of observation. At an element of size 30 voxels, the lengthscale of pore propagation reaches the limit of the scan length.

Regarding high-tortuosity regions, an increase in their propagation distance is also observed with increasing kernel dimension. However, the impact of the kernel size is

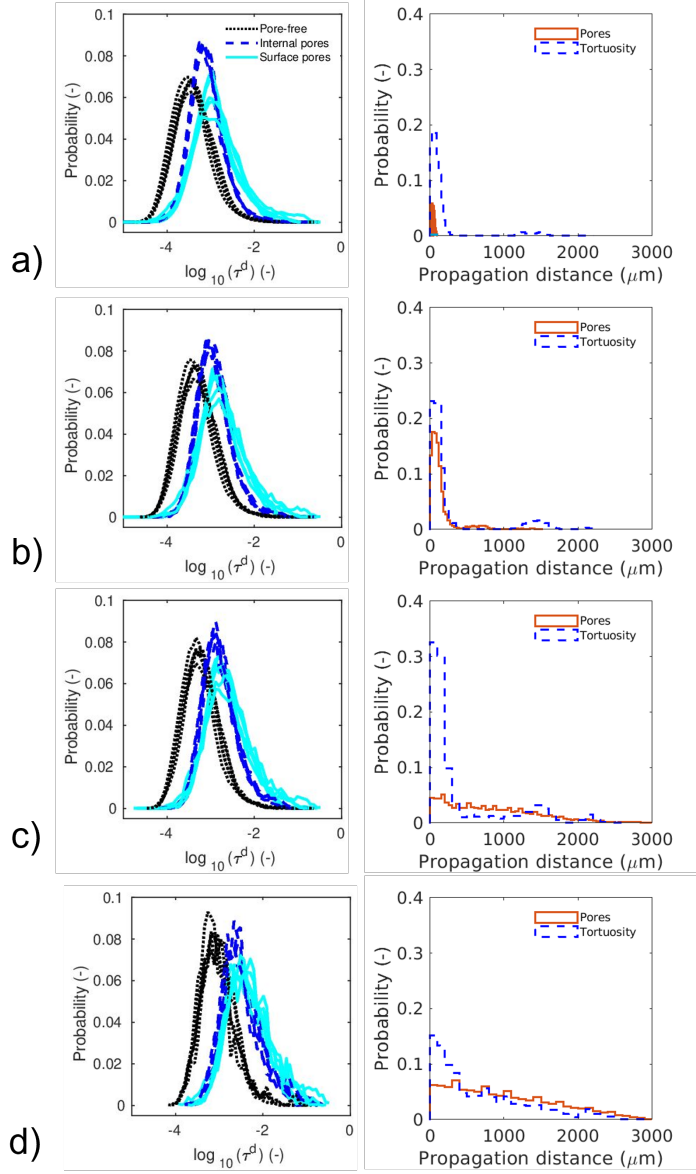


Figure G.1: Results of the correlation of tortuosity and pore areas (left), and extracted lengthscales of propagation for pores and tortuosity (right) for different kernel sizes a) [5,5,5] b) [10,10,10] c) [15,15,15] (used in the main manuscript) d) [30,30,30].

less prominent. A possible explanation is that while the porosity distribution consists of multiple small separate entities, the high-value range of the tortuosity distribution linearly

interpolated to the 3D space is composed of larger and more connected elements.

It should be, however, noted that a kernel size of 30 voxels corresponds to about six data points through the thickness of the tape, which might lead to a too-high level of homogenisation.



# H

## APPENDIX: SINGLE-FIBRE MISALIGNMENT FOR ALL SAMPLES

This appendix refers to **Chapter 4**. In this Appendix, the misalignment maps derived from single fibre analysis relative to the  $xy$  plane are shown for all samples in Figure H.1.

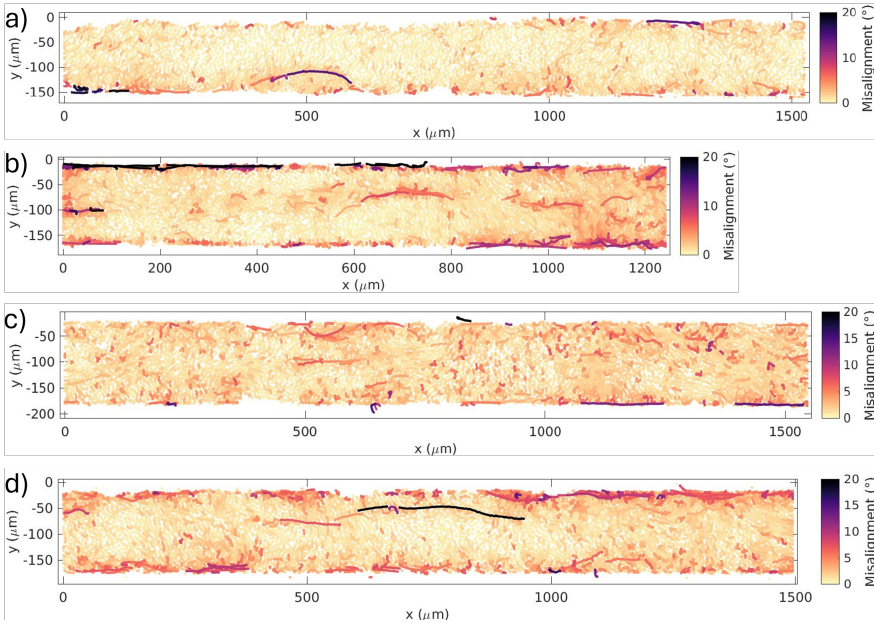


Figure H.1: Misalignment maps, where each single fibre trajectory is projected on the  $xy$  plane and labelled according to its maximum misalignment value for a) Sample 1; b) Sample 2; c) Sample 3; d) Sample 4.



# I

## APPENDIX: STRUCTURE-TENSOR-BASED MISALIGNMENT FOR ALL SAMPLES

This appendix refers to **Chapter 4**. In this Appendix, the misalignment maps derived from structure tensor analysis relative to the  $xy$  plane are shown for all samples in Figure I.1 for 0.8  $\mu\text{m}$  dataset, in I.2 for 2  $\mu\text{m}$  dataset, and in I.3 for 3.5  $\mu\text{m}$  dataset.

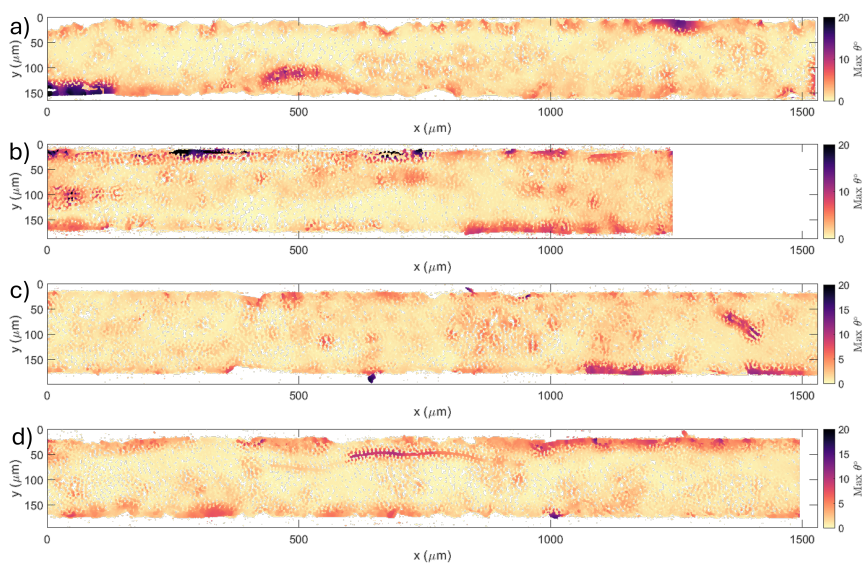


Figure I.1: Misalignment maps determined via structure tensor analysis of  $0.8\ \mu\text{m}$  datasets, where the maximum structure tensor value on each cross-sectional location on the transversal cross-sectional plane  $xy$  is shown, for a) Sample 1; b) Sample 2; c) Sample 3; d) Sample 4.



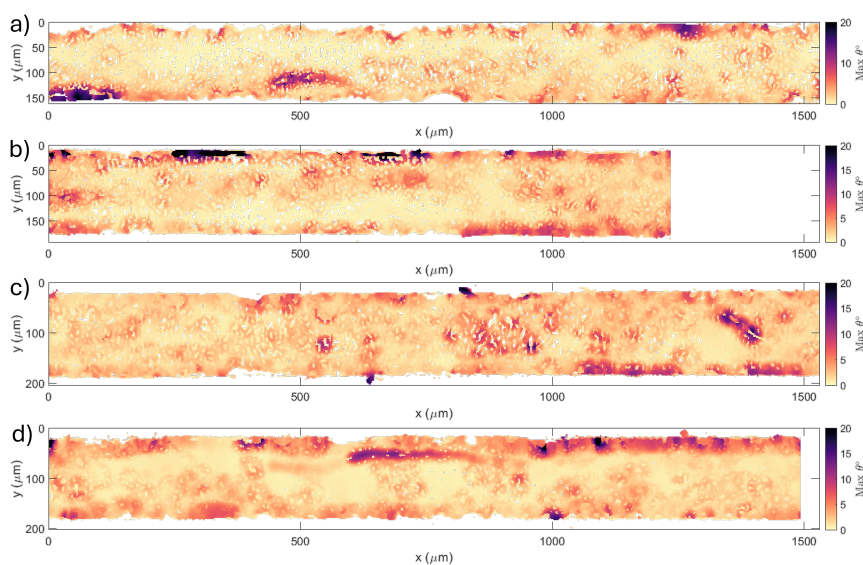


Figure I.2: Misalignment maps determined via structure tensor analysis of  $2\ \mu\text{m}$  datasets, where the maximum structure tensor value on each cross-sectional location on the transversal cross-sectional plane  $xy$  is shown, for a) Sample 1; b) Sample 2; c) Sample 3; d) Sample 4.

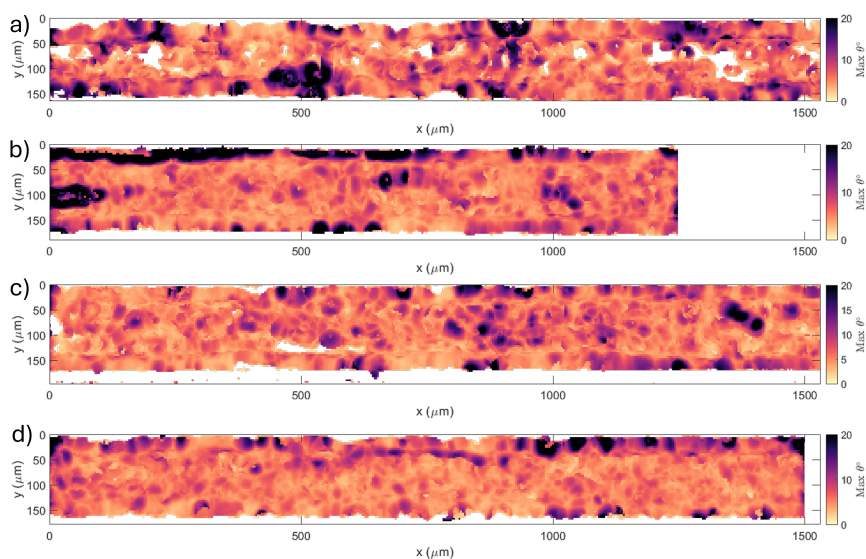


Figure I.3: Misalignment maps determined via structure tensor analysis of  $3.5\ \mu\text{m}$  datasets, where the maximum structure tensor value on each cross-sectional location on the transversal cross-sectional plane  $xy$  is shown, for a) Sample 1; b) Sample 2; c) Sample 3; d) Sample 4.

# BIBLIOGRAPHY

## REFERENCES

- [1] F. Malgioglio, S. Pimenta, A. Matveeva, L. Farkas, W. Desmet, S. V. Lomov, and Y. Swolfs, "Microscale material variability and its effect on longitudinal tensile failure of unidirectional carbon fibre composites," *Composite Structures*, vol. 261, no. October 2020, p. 113300, 2020. [Online]. Available: <https://doi.org/10.1016/j.compstruct.2020.113300>
- [2] R. Amacher, J. Cugnoli, J. Botsis, L. Sorensen, W. Smith, and C. Dransfeld, "Thin ply composites: Experimental characterization and modeling of size-effects," *Composites Science and Technology*, vol. 101, pp. 121–132, 2014. [Online]. Available: <http://dx.doi.org/10.1016/j.compscitech.2014.06.027>
- [3] P. Parandoush and D. Lin, "A review on additive manufacturing of polymer-fiber composites," *Composite Structures*, vol. 182, pp. 36–53, 2017. [Online]. Available: <https://doi.org/10.1016/j.compstruct.2017.08.088>
- [4] M. Eichenhofer, J. C. Wong, and P. Ermanni, "Exploiting cyclic softening in continuous lattice fabrication for the additive manufacturing of high performance fibre-reinforced thermoplastic composite materials," *Composites Science and Technology*, vol. 164, no. May, pp. 248–259, 2018. [Online]. Available: <https://doi.org/10.1016/j.compscitech.2018.05.033>
- [5] T. H. Vaneker, "Material Extrusion of Continuous Fiber Reinforced Plastics Using Commingled Yarn," *Procedia CIRP*, vol. 66, pp. 317–322, 2017. [Online]. Available: <http://dx.doi.org/10.1016/j.procir.2017.03.367>
- [6] A. Thakur and X. Dong, "Printing with 3D continuous carbon fiber multifunctional composites via UV-assisted coextrusion deposition," *Manufacturing Letters*, vol. 24, pp. 1–5, 2020. [Online]. Available: <https://doi.org/10.1016/j.mfglet.2020.02.001>
- [7] B. R. Denos, D. E. Sommer, A. J. Favaloro, R. B. Pipes, and W. B. Avery, "Fiber orientation measurement from mesoscale CT scans of prepreg platelet molded composites," *Composites Part A: Applied Science and Manufacturing*, vol. 114, no. August, pp. 241–249, 2018. [Online]. Available: <https://doi.org/10.1016/j.compositesa.2018.08.024>
- [8] N. Q. Nguyen, M. Mehdikhani, I. Straumit, L. Gorbatikh, L. Lessard, and S. V. Lomov, "Micro-CT measurement of fibre misalignment: Application to carbon/epoxy laminates manufactured in autoclave and by vacuum assisted resin transfer moulding," *Composites Part A: Applied Science and Manufacturing*, vol. 104, pp. 14–23, 2018. [Online]. Available: <https://doi.org/10.1016/j.compositesa.2017.10.018>

- [9] T. Baranowski, D. Dobrovolskij, K. Dremel, A. Hölzing, G. Lohfink, K. Schladitz, and S. Zabler, "Local fiber orientation from X-ray region-of-interest computed tomography of large fiber reinforced composite components," *Composites Science and Technology*, vol. 183, no. February, 2019. [Online]. Available: <https://doi.org/10.1016/j.compscitech.2019.107786>
- [10] T. A. Sebaey, G. Catalanotti, and N. P. O'Dowd, "A microscale integrated approach to measure and model fibre misalignment in fibre-reinforced composites," *Composites Science and Technology*, vol. 183, no. June, p. 107793, 2019. [Online]. Available: <https://doi.org/10.1016/j.compscitech.2019.107793>
- [11] R. Belliveau, É. Léger, B. Landry, and G. LaPlante, "Measuring fibre orientation and predicting elastic properties of discontinuous long fibre thermoplastic composites," *Journal of Composite Materials*, 2020. [Online]. Available: <https://doi.org/10.1177/0021998320949635>
- [12] L. Schöttl, D. Dörr, P. Pinter, K. A. Weidenmann, P. Elsner, and L. Kärger, "A novel approach for segmenting and mapping of local fiber orientation of continuous fiber-reinforced composite laminates based on volumetric images," *NDT and E International*, vol. 110, no. June 2019, 2020. [Online]. Available: <https://doi.org/10.1016/j.ndteint.2019.102194>
- [13] F. Gommer, A. Endruweit, and A. C. Long, "Analysis of filament arrangements and generation of statistically equivalent composite micro-structures," *Composites Science and Technology*, vol. 99, pp. 45–51, 2014. [Online]. Available: <http://dx.doi.org/10.1016/j.compscitech.2014.05.008>
- [14] M. Mehdikhani, C. Breite, Y. Swolfs, M. Wevers, S. V. Lomov, and L. Gorbatikh, "Combining digital image correlation with X-ray computed tomography for characterization of fiber orientation in unidirectional composites," *Composites Part A: Applied Science and Manufacturing*, vol. 142, no. November 2020, p. 106234, 2021. [Online]. Available: <https://doi.org/10.1016/j.compositesa.2020.106234>
- [15] T. K. Slange, L. L. Warnet, W. J. Grouve, and R. Akkerman, "Deconsolidation of C/PEEK blanks: on the role of prepreg, blank manufacturing method and conditioning," *Composites Part A: Applied Science and Manufacturing*, vol. 113, no. July, pp. 189–199, 2018. [Online]. Available: <https://doi.org/10.1016/j.compositesa.2018.06.034>
- [16] G. Catalanotti and T. Sebaey, "An algorithm for the generation of three-dimensional statistically representative volume elements of unidirectional fibre-reinforced plastics: Focusing on the fibres waviness," *Composite Structures*, vol. 227, p. 111272, 2019. [Online]. Available: <https://doi.org/10.1016/j.compstruct.2019.111272>
- [17] F. Gommer, K. C. A. Wedgwood, and L. P. Brown, "Stochastic reconstruction of filament paths in fibre bundles based on two-dimensional input data," *Composites Part A: Applied Science and 555 Manufacturing*, vol. 76, pp. 262–271, 2015. [Online]. Available: <http://dx.doi.org/10.1016/j.compositesa.2015.05.022>

- [18] M. J. Emerson, K. M. Jespersen, A. B. Dahl, K. Conradsen, and L. P. Mikkelsen, "Individual fibre segmentation from 3D X-ray computed tomography for characterising the fibre orientation in unidirectional composite materials," *Composites Part A: Applied Science and Manufacturing*, vol. 97, pp. 83–92, 2017. [Online]. Available: <http://dx.doi.org/10.1016/j.compositesa.2016.12.028>
- [19] M. J. Emerson, V. A. Dahl, K. Conradsen, L. P. Mikkelsen, and A. B. Dahl, "Statistical validation of individual fibre segmentation from tomograms and microscopy," *Composites Science and Technology*, vol. 160, no. January, pp. 208–215, 2018. [Online]. Available: <https://doi.org/10.1016/j.compscitech.2018.03.027>
- [20] K. Amjad, W. J. Christian, K. Dvurecenska, M. G. Chapman, M. D. Uchic, C. P. Przybyla, and E. A. Patterson, "Computationally efficient method of tracking fibres in composite materials using digital image correlation," *Composites Part A: Applied Science and Manufacturing*, vol. 129, no. October 2019, p. 105683, 2020. [Online]. Available: <https://doi.org/10.1016/j.compositesa.2019.105683>
- [21] N. Jeppesen, L. P. Mikkelsen, A. B. Dahl, A. N. Christensen, and V. A. Dahl, "Quantifying effects of manufacturing methods on fiber orientation in unidirectional composites using structure tensor analysis," *Composites Part A*, vol. 149, no. July, p. 106541, 2021. [Online]. Available: <https://doi.org/10.1016/j.compositesa.2021.106541>
- [22] R. Karamov, L. M. Martulli, M. Kerschbaum, I. Sergeichev, Y. Swolfs, and S. V. Lomov, "Micro-CT based structure tensor analysis of fibre orientation in random fibre composites versus high-fidelity fibre identification methods," *Composite Structures*, vol. 235, no. November 2019, p. 111818, 2020. [Online]. Available: <https://doi.org/10.1016/j.compstruct.2019.111818>
- [23] A. T. Zehnder, V. Patel, and T. J. Rose, "Micro-CT Imaging of Fibers in Composite Laminates under High Strain Bending," *Experimental Techniques*, vol. 44, no. 5, pp. 531–540, 2020. [Online]. Available: <https://doi.org/10.1007/s40799-020-00374-9>
- [24] N. K. Fritz, R. Kopp, A. K. Nason, X. Ni, J. Lee, I. Y. Stein, E. Kalfon-Cohen, I. Sinclair, S. M. Spearing, P. P. Camanho, and B. L. Wardle, "New interlaminar features and void distributions in advanced aerospace-grade composites revealed via automated algorithms using micro-computed tomography," *Composites Science and Technology*, vol. 193, no. September 2019, p. 108132, 2020. [Online]. Available: <https://doi.org/10.1016/j.compscitech.2020.108132>
- [25] Y. Wang, M. J. Emerson, K. Conradsen, A. B. Dahl, V. A. Dahl, E. Maire, and P. J. Withers, "Evolution of Fibre Deflection Leading to Kink-band Formation in Unidirectional Glass Fibre/Epoxy Composite Under Axial Compression," *Composites Science and Technology*, vol. 213, p. 108929, 2021. [Online]. Available: <https://doi.org/10.1016/j.compscitech.2021.108929>
- [26] T. Fast, A. E. Scott, H. A. Bale, and B. N. Cox, "Topological and Euclidean metrics reveal spatially nonuniform structure in the entanglement of stochastic fiber bundles," *Journal of Materials Science*, vol. 50, no. 6, pp. 2370–2398, 2015. [Online]. Available: <https://doi.org/10.1007/s10853-014-8766-2>

- [27] T. Vicsek, A. Czirak, E. Ben-Jacob, I. Cohen, and O. Shochet, "Novel type of phase transition in a system of self-driven particles," *Physical Review Letters*, vol. 75, no. 6, pp. 1226–1229, 1995. [Online]. Available: <https://doi.org/10.1103/PhysRevLett.75.1226>
- [28] T. Vicsek and A. Zafeiris, "Collective motion," *Physics Reports*, vol. 517, no. 3-4, pp. 71–140, 2010. [Online]. Available: <https://doi.org/10.1016/j.physrep.2012.03.004>
- [29] W. Song, C. Zhang, and Z. Wang, "Investigation of the microstructural characteristics and the tensile strength of silkworm cocoons using X-ray micro computed tomography," *Materials and Design*, vol. 199, p. 109436, 2021. [Online]. Available: <https://doi.org/10.1016/j.matdes.2020.109436>
- [30] F. LeBel, A. E. Fanaei, É. Ruiz, and F. Trochu, "Experimental Characterization by Fluorescence of Capillary Flows in the Fiber Tows of Engineering Fabrics," *Open Journal of Inorganic Non-metallic Materials*, vol. 02, no. 03, pp. 25–45, 2012. [Online]. Available: <https://doi.org/10.4236/ojinm.2012.23004>
- [31] N.-j. Jan, B. L. Brazile, D. Hu, G. Grube, J. Wallace, A. Gogola, and I. A. Sigal, "Crimp around the globe ; patterns of collagen crimp across the corneoscleral shell," *Experimental Eye Research*, vol. 172, no. April, pp. 159–170, 2018. [Online]. Available: <https://doi.org/10.1016/j.exer.2018.04.003>
- [32] W. Szmyt, C. Guerra-Núñez, C. Dransfeld, and I. Utke, "Solving the inverse Knudsen problem: Gas diffusion in random fibrous media," *Journal of Membrane Science*, vol. 620, no. August 2020, 2021. [Online]. Available: <https://doi.org/10.1016/j.memsci.2020.118728>
- [33] E. Méhes and T. Vicsek, "Collective motion of cells: From experiments to models," *Integrative Biology*, vol. 6, no. 9, pp. 831–854, 2014. [Online]. Available: <https://doi.org/10.1039/c4ib00115j>
- [34] G. K. Taylor, M. S. Triantafyllou, and C. Tropea, *Animal locomotion*, C. Taylor, G.K., Triantafyllou M. S., Tropea, Ed. Springer, 2010.
- [35] M. Nagy, Z. Ákos, D. Biro, and T. Vicsek, "Hierarchical group dynamics in pigeon flocks," *Nature*, vol. 464, no. 7290, pp. 890–893, 2010. [Online]. Available: <https://doi.org/10.1038/nature08891>
- [36] H. R. Jessel, L. Aharoni, S. Efroni, and I. Bachelet, "A modeling algorithm for exploring the architecture and construction of bird nests," *Scientific Reports*, vol. 9, no. 1, pp. 1–9, 2019. [Online]. Available: <https://doi.org/10.1038/s41598-019-51478-1>
- [37] J. Vigiúí, P. Latil, L. Orgéas, P. Dumont, S. R. du Roscoat, J.-F. Bloch, C. Marulier, and O. Guiraud, "Finding fibres and their contacts within 3d images of disordered fibrous media," *Composites Science and Technology*, vol. 89, pp. 202–210, 2013. [Online]. Available: <https://doi.org/10.1016/j.compscitech.2013.09.023>
- [38] J. Srisuriyachot, J. Bénézech, G. Couégnat, S. A. McNair, T. Maierhofer, R. Butler, and A. J. Lunt, "Synchrotron micro-ct in kink-band formation of ud-cfrp laminates with

- microdefects,” *Composites Part B: Engineering*, vol. 266, p. 111038, 2023. [Online]. Available: <https://doi.org/10.1016/j.compositesb.2023.111038>
- [39] S. Boztepe, P. Šimáček, K. Labastie, M. Chevalier, P. Sandre, J.-M. Des, and S. G. Advani, “Effect of the initial resin distribution in partially impregnated thermoplastic prepregs on consolidation,” *Composites Science and Technology*, vol. 225, p. 109488, 2022. [Online]. Available: <https://doi.org/10.1016/j.compscitech.2022.109488>.
- [40] O. Ferguson, S. Skovsgaard, H. Jensen, and L. Mikkelsen, “Compressive strength prediction of carbon fiber-reinforced pultruded profiles including realistic volumetric fiber orientations,” *European Journal of Mechanics - A/Solids*, vol. 104, Supplement, p. 105011, 2024. [Online]. Available: <https://doi.org/10.1016/j.euromechsol.2023.105011>
- [41] S. Gomasasca, D. Peeters, B. Atli-Veltin, and C. Dransfeld, “Characterising microstructural organisation in unidirectional composites,” *Composites Science and Technology*, vol. 215, no. July, p. 109030, 2021. [Online]. Available: <https://doi.org/10.1016/j.compscitech.2021.109030>
- [42] J. Jhavar, R. G. Morris, U. R. Amith-Kumar, M. Danny Raj, T. Rogers, H. Rajendran, and V. Guttal, “Noise-induced schooling of fish,” *Nature Physics*, vol. 16, no. 4, pp. 488–493, 2020. [Online]. Available: <http://dx.doi.org/10.1038/s41567-020-0787-y>
- [43] P. J. Creveling, W. W. Whitacre, and M. W. Czabaj, “A fiber-segmentation algorithm for composites imaged using X-ray microtomography : Development and validation,” *Composites Part A*, vol. 126, no. August, p. 105606, 2019. [Online]. Available: <https://doi.org/10.1016/j.compositesa.2019.105606>
- [44] J. Schindelin, I. Arganda-Carreras, E. Frise, V. Kaynig, M. Longair, T. Pietzsch, S. Preibisch, C. Rueden, S. Saalfeld, B. Schmid, J. Y. Tinevez, D. J. White, V. Hartenstein, K. Eliceiri, P. Tomancak, and A. Cardona, “Fiji: An open-source platform for biological-image analysis,” *Nature Methods*, vol. 9, no. 7, pp. 676–682, 2012. [Online]. Available: <https://doi.org/10.1038/nmeth.2019>
- [45] D. G. Lowe, “Distinctive image features from scale-invariant keypoints,” *International Journal of Computer Vision*, vol. 60, no. 2, pp. 91–110, 2004. [Online]. Available: <https://doi.org/10.1023/B:VISI.0000029664.99615.94>
- [46] I. Arganda-Carreras, V. Kaynig, C. Rueden, K. W. Eliceiri, J. Schindelin, A. Cardona, and H. S. Seung, “Trainable Weka Segmentation: A machine learning tool for microscopy pixel classification,” *Bioinformatics*, vol. 33, no. 15, pp. 2424–2426, 2017. [Online]. Available: <https://doi.org/10.1093/bioinformatics/btx180>
- [47] J. Y. Tinevez, N. Perry, J. Schindelin, G. M. Hoopes, G. D. Reynolds, E. Laplantine, S. Y. Bednarek, S. L. Shorte, and K. W. Eliceiri, “TrackMate: An open and extensible platform for single-particle tracking,” *Methods*, vol. 115, pp. 80–90, 2017. [Online]. Available: <http://dx.doi.org/10.1016/j.ymeth.2016.09.016>
- [48] N. Chenouard, I. Smal, F. De Chaumont, M. Maška, I. F. Sbalzarini, Y. Gong, J. Cardinale, C. Carthel, S. Coraluppi, M. Winter, A. R. Cohen, W. J. Godinez, K. Rohr,



- Y. Kalaidzidis, L. Liang, J. Duncan, H. Shen, Y. Xu, K. E. Magnusson, J. Jaldén, H. M. Blau, P. Paul-Gilloteaux, P. Roudot, C. Kervrann, F. Waharte, J. Y. Tinevez, S. L. Shorte, J. Willemse, K. Celler, G. P. Van Wezel, H. W. Dan, Y. S. Tsai, C. O. De Solórzano, J. C. Olivo-Marin, and E. Meijering, "Objective comparison of particle tracking methods," *Nature Methods*, vol. 11, no. 3, pp. 281–289, 2014. [Online]. Available: <https://doi.org/10.1038/nmeth.2808>
- [49] J. Mandle, R.J., Goodby, "Order Parameters, Orientational Distribution Functions and Heliconical Tilt Angles of Oligomeric Liquid Crystals," *Phys. Chem.*, vol. 21, pp. 6839–6843, 2019. [Online]. Available: <https://doi.org/10.1039/C9CP00736A>
- [50] L. Burtseva, F. Werner, B. V. Salas, A. Pestryakov, R. Romero, and V. Petranovskii, "Modeling of the material structure using Voronoi diagrams and tessellation methods," *Technical Report*, no. January, pp. 1–11, 2015. [Online]. Available: <https://doi.org/10.13140/2.1.2418.4648>
- [51] J. Maksimcuka, A. Obata, W. W. Sampson, R. Blanc, C. Gao, P. J. Withers, O. Tsigkou, T. Kasuga, P. D. Lee, and G. Poologasundarampillai, "X-ray tomographic imaging of tensile deformation modes of electrospun biodegradable polyester fibers," *Frontiers in Materials*, vol. 4, no. December, pp. 1–11, 2017. [Online]. Available: <https://doi.org/10.3389/fmats.2017.00043>
- [52] M. S. Irfan, V. R. MacHavaram, R. S. Mahendran, N. Shotton-Gale, C. F. Wait, M. A. Paget, M. Hudson, and G. F. Fernando, "Lateral spreading of a fiber bundle via mechanical means," *Journal of Composite Materials*, vol. 46, no. 3, pp. 311–330, 2012. [Online]. Available: <https://doi.org/10.1177/0021998311424624>
- [53] J. Studer, C. Dransfeld, J. Jauregui Cano, A. Keller, M. Wink, K. Masania, and B. Fiedler, "Effect of fabric architecture, compaction and permeability on through thickness thermoplastic melt impregnation," *Composites Part A: Applied Science and Manufacturing*, vol. 122, no. April, pp. 45–53, 2019. [Online]. Available: <https://doi.org/10.1016/j.compositesa.2019.04.008>
- [54] K. K. Ho, S. R. Shamsuddin, S. Riaz, S. Lamorinere, M. Q. Tran, A. Javaid, and A. Bismarck, "Wet impregnation as route to unidirectional carbon fibre reinforced thermoplastic composites manufacturing," *Plastics, Rubber and Composites*, vol. 40, no. 2, pp. 100–107, 2011. [Online]. Available: <https://doi.org/10.1179/174328911X12988622801098>
- [55] W. Wang, Y. Dai, C. Zhang, X. Gao, and M. Zhao, "Micromechanical Modeling of Fiber-Reinforced Composites with Statistically Equivalent Random Fiber Distribution," *Materials*, vol. 9, no. 8, pp. 1–14, 2016. [Online]. Available: <https://doi.org/10.3390/ma9080624>
- [56] L. Varandas, G. Catalanotti, A. Melro, R. Tavares, and B. Falzon, "Micromechanical modelling of the longitudinal compressive and tensile failure of unidirectional composites: The effect of fibre misalignment introduced via a stochastic process," *International Journal of Solids and Structures*, vol. 203, pp. 157–176, 2020. [Online]. Available: <https://doi.org/10.1016/j.ijsolstr.2020.07.022>



- [57] O. Çelik, D. Peeters, C. Dransfeld, and J. Teuwen, "Intimate contact development during laser assisted fiber placement: Microstructure and effect of process parameters," *Composites Part A: Applied Science and Manufacturing*, vol. 134, p. 105888, 2020. [Online]. Available: <https://doi.org/10.1016/j.compositesa.2020.105888>
- [58] S. Gomasasca, D. Peeters, T. Slange, G. Ratouit, B. Atli-Veltin, and C. Dransfeld, "Characterising pore networks and their interrelation with the fibre architecture in unidirectional composites," *Composites Part A: Applied Science and Manufacturing*, vol. 190, p. 108669, 2025. [Online]. Available: <https://doi.org/10.1016/j.compositesa.2024.108669>
- [59] A. Schlothauer, G. A. Pappas, and P. Ermanni, "Thin-ply thermoplastic composites: From weak to robust transverse performance through microstructural and morphological tuning," *Composites Part B: Engineering*, vol. 261, p. 110764, 2023. [Online]. Available: <https://doi.org/10.1016/j.compositesb.2023.110764>
- [60] L. Amedewovo, L. Orgéas, B. de Parscau du Plessix, N. Lefevre, A. Levy, and S. L. Corre, "Deconsolidation of carbon fiber-reinforced pekk laminates: 3d real-time in situ observation with synchrotron x-ray microtomography," *Composites Part A: Applied Science and Manufacturing*, vol. 177, p. 107917, 2024. [Online]. Available: <https://doi.org/10.1016/j.compositesa.2023.107917>
- [61] S. Gomasasca, D. M. J. Peeters, B. Atli-Veltin, C. A. Dransfeld, and H. Luinge, "The role of matrix boundary in the microstructure of unidirectional composites," *Proceedings of the 20th European Conference on Composite Materials - Composites Meet Sustainability*, vol. 3, pp. 636–643, 2022. [Online]. Available: [https://doi.org/10.5075/epfl-298799\\_978-2-9701614-0-0](https://doi.org/10.5075/epfl-298799_978-2-9701614-0-0)
- [62] M. Mehdikhani, L. Gorbatikh, I. Verpoest, and S. V. Lomov, "Voids in fiber-reinforced polymer composites: A review on their formation, characteristics, and effects on mechanical performance," *Journal of Composite Materials*, vol. 53(12), pp. 1579–1669, 2019. [Online]. Available: <https://doi.org/10.1177/0021998318772152>
- [63] M. Mehdikhani, I. Straumit, L. Gorbatikh, and S. V. Lomov, "Detailed characterization of voids in multidirectional carbon fiber/epoxy composite laminates using X-ray micro-computed tomography," *Composites Part A: Applied Science and Manufacturing*, vol. 125, p. 105532, 2019. [Online]. Available: <https://doi.org/10.1016/j.compositesa.2019.105532>
- [64] S. Gomasasca, D. Peeters, B. Atli-Veltin, and C. Dransfeld, "X-ray computed tomography of a unidirectional composite tape with microporosity features," 2024. [Online]. Available: <https://doi.org/10.4121/b877fe30-d07f-4936-af8d-06fb78c54566>
- [65] M. Alves, Y. Li, and S. Pimenta, "Spatial variability and characteristic length-scales of strain fields in tow-based discontinuous composites: Characterisation and modelling," *Composites Part B: Engineering*, vol. 262, no. April, p. 110789, 2023. [Online]. Available: <https://doi.org/10.1016/j.compositesb.2023.110789>

- [66] M. P. Sutcliffe, S. L. Lemanski, and A. E. Scott, "Measurement of fibre waviness in industrial composite components," *Composites Science and Technology*, vol. 72, no. 16, pp. 2016–2023, 2012. [Online]. Available: <http://dx.doi.org/10.1016/j.compscitech.2012.09.001>
- [67] M. B. Hisham, S. N. Yaakob, R. A. Raof, A. B. Nazren, and N. M. Embedded, "Template Matching using Sum of Squared Difference and Normalized Cross Correlation," *2015 IEEE Student Conference on Research and Development, SCORED 2015*, pp. 100–104, 2015.
- [68] D. R. Bull, *Coding Moving Pictures: Motion Prediction*. Academic Press, 2014. [Online]. Available: <https://doi.org/10.1016/b978-0-12-405906-1.00008-8>
- [69] J. Blarr, S. Klinder, W. Liebig, K. Inal, L. Kärger, and K. Weidenmann, "Deep convolutional generative adversarial network for generation of computed tomography images of discontinuously carbon fiber reinforced polymer microstructures," *Sci Rep*, vol. 14, p. 9641, 2024. [Online]. Available: <https://doi.org/10.1038/s41598-024-59252-8>
- [70] R. Arquier, H. Sabatier, I. Iliopoulos, G. Régnier, and G. Miquelard-Garnier, "Role of the inter-ply microstructure in the consolidation quality of high-performance thermoplastic composites," *Polymer Composites*, vol. 45, pp. 1218–1227, 2024. [Online]. Available: <https://doi.org/10.1002/pc.27847>
- [71] J. R. Wood and M. G. Bader, "Void control for polymer-matrix composites (1): Theoretical and experimental methods for determining the growth and collapse of gas bubbles," *Composites Manufacturing*, vol. 5, pp. 139–147, 1994. [Online]. Available: [https://doi.org/10.1016/0956-7143\(94\)90023-X](https://doi.org/10.1016/0956-7143(94)90023-X)
- [72] J. Vilà, F. Sket, F. Wilde, G. Requena, C. González, and J. LLorca, "An in situ investigation of microscopic infusion and void transport during vacuum-assisted infiltration by means of x-ray computed tomography," *Composites Science and Technology*, vol. 119, pp. 12–19, 2015. [Online]. Available: <https://doi.org/10.1016/j.compscitech.2015.09.016>
- [73] P. Latil, L. Orgéas, C. Geindreau, P. Dumont, and S. R. du Roscoat, "Towards the 3d in situ characterisation of deformation micro-mechanisms within a compressed bundle of fibres," *Composites Science and Technology*, vol. 71, pp. 480–488, 2011. [Online]. Available: <https://doi.org/10.1016/j.compscitech.2010.12.023>
- [74] S. Hosseini, A. den Otter, J. Zevenbergen, B. Atli-Veltin, and C. Dransfeld, "Methodology for the identification of hydrogen gas permeation path in damaged laminates," *Proceedings of the 20th European Conference on Composite Materials - Composites Meet Sustainability*, vol. 5, pp. 306–313, 2022. [Online]. Available: [https://doi.org/10.5075/epfl-298799\\_978-2-9701614-0-0](https://doi.org/10.5075/epfl-298799_978-2-9701614-0-0)
- [75] Y. M. Buser, W. J. Grouve, E. Krämer, and R. Akkerman, "Electrical Conductivity Characterisation of Stochastic Zigzag Paths in Unidirectional C/PAEK," *Proceedings of the 23th International Conference on Composite Materials (ICCM23)*, vol. 27, 2023.

- [76] L. Appel, A. Kerber, B. Abbas, S. Jeschke, and T. Gries, "Determination of interactions between bar spreading process parameters and spreading quality for the development of an automated quality control of spread high modulus fiber tows," *Proceedings of the 17th European Conference on Composite Materials, ECCM17, 26-30th June 2016, Munich, Germany, organized by TUM, Institute for Carbon Composites*, vol. 5 - Manufacturing Technologies, 2016.
- [77] Q. Yi, P. Wilcox, and R. Hughes, "Modelling and evaluation of carbon fibre composite structures using high-frequency eddy current imaging," *Composites Part B: Engineering*, vol. 248, p. 110343, 2023. [Online]. Available: <https://doi.org/10.1016/j.compositesb.2022.110343>
- [78] R. M. Auenhammer, A. Prajapati, K. Kalasho, L. P. Mikkelsen, P. J. Withers, L. E. Asp, and R. Gutkin, "Fibre orientation distribution function mapping for short fibre polymer composite components from low resolution/large volume x-ray computed tomography," *Composites Part B: Engineering*, vol. 275, p. 111313, 2024. [Online]. Available: <https://doi.org/10.1016/j.compositesb.2024.111313>
- [79] R. Auenhammer, J. Kim, C. Oddy, L. P. Mikkelsen, F. Marone, M. Stampanoni, and L. E. Asp, "X-ray scattering tensor tomography based finite element modelling of heterogeneous materials," *npj Comput Mater*, vol. 10, 2024. [Online]. Available: <https://doi.org/10.1038/s41524-024-01234-5>
- [80] H. Yu, K. Potter, and M. Wisnom, "A novel manufacturing method for aligned discontinuous fibre composites (High Performance-Discontinuous Fibre method)," *Composites Part A: Applied Science and Manufacturing*, vol. 65, pp. 175–185, 2014. [Online]. Available: <https://doi.org/10.1016/j.compositesa.2014.06.005>
- [81] T. Laurencin, L. Orgéas, P. Dumont, S. R. du Roscoat, P. Laure, S. L. Corre, L. Silva, R. Mokso, and M. Terrien, "3d real-time and in situ characterisation of fibre kinematics in dilute non-newtonian fibre suspensions during confined and lubricated compression flow," *Composites Science and Technology*, vol. 134, pp. 258–266, 2016. [Online]. Available: <https://doi.org/10.1016/j.compscitech.2016.09.004>
- [82] F. Sosa-Rey, Y. Abderrafai, A. D. Lewis, D. Therriault, N. Piccirelli, and M. Lévesque, "OpenFiberSeg: Open-source segmentation of individual fibers and porosity in tomographic scans of additively manufactured short fiber reinforced composites," *Composites Science and Technology*, vol. 226, p. 109497, 2022. [Online]. Available: <https://doi.org/10.1016/j.compscitech.2022.109497>
- [83] S. Gomasasca, S. Hossein, R. Tao, B. Boos, C. Queck, D. Peeters, B. Atli-veltin, M. Gurka, and C. Dransfeld, "Assessment of the variability of unidirectional prepreps at multiple scales," *e-Journal of Nondestructive Testing*, vol. 30, no. 2, pp. 4–7, 2025. [Online]. Available: <https://doi.org/10.58286/30713>
- [84] M. J. Schey, T. Beke, L. Appel, S. Zabler, S. Shah, J. Hu, F. Liu, M. Maiaru, and S. Stapleton, "Identification and quantification of 3d fiber clusters in fiber-reinforced composite materials," *JOM*, vol. 73, pp. 2129–2142, 2021. [Online]. Available: <https://doi.org/10.1007/s11837-021-04703-0>

- [85] M. Schey, T. Beke, K. Owens, A. George, E. Pineda, and S. Stapleton, "Effects of debulking on the fiber microstructure and void distribution in carbon fiber reinforced plastics," *Composites Part A*, vol. 165, p. 107364, 2023. [Online]. Available: <https://doi.org/10.1016/j.compositesa.2022.107364>
- [86] K. Nelms, P. Paul, A. Wowogno, Y. Chen, B. Lukic, A. Rack, N. Chandarana, and P. Withers, "Effect of fibre orientation on compression micromechanics in cfrp investigated by computed tomography," *Twenty-Third International Conference On Composite Materials (ICCM23). Queen's University Belfast, University Road, Belfast, Northern Ireland, BT7 1NN*, 12 p., 2023.
- [87] C. Xie, Y. Meng, J. Chen, Z. Zhao, J. Wang, J. Jiang, and Y. Li, "Interaction of multiple micro-defects on the strength and failure mechanism of UD composites by computational micromechanics," *Composite Structures*, vol. 349–350, p. 118492, 2024. [Online]. Available: <https://doi.org/10.1016/j.compstruct.2024.118492>
- [88] N. Liu and P. Chen, "A three-dimensional failure criterion model considering the effects of fiber misalignment on longitudinal tensile failure," *Composites Science and Technology*, vol. 247, p. 110424, 2024. [Online]. Available: <https://doi.org/10.1016/j.compscitech.2023.110424>.
- [89] D. Legland, I. Arganda-Carreras, P. Andrey, and MorphoLibJ, "MorphoLibJ: integrated library and plugins for mathematical morphology with ImageJ," *Bioinformatics*, vol. 22, p. 3532–3534, 2016. [Online]. Available: <https://doi.org/10.1093/bioinformatics/btw413>
- [90] N. Jeppesen, V. A. Dahl, A. N. Christensen, A. B. Dahl, and L. P. Mikkelsen, "Characterization of the fiber orientations in non-crimp glass fiber reinforced composites using structure tensor," *IOP Conf. Series: Materials Science and Engineering*, vol. 492, p. 012037, 2020. [Online]. Available: <https://doi.org/10.1088/1757-899X/942/1/012037>
- [91] N. Jeppesen, V. A. Dahl, A. N. Christensen, A. B. Dahl, and L. Mikkelsen, "Characterization of the Fiber Orientations in Non-Crimp Glass Fiber Reinforced Composites using Structure Tensor," *Zenodo*, 2020. [Online]. Available: <http://dx.doi.org/10.5281/zenodo.3877522>
- [92] I. Straumit, S. V. Lomov, and M. Wevers, "Quantification of the internal structure and automatic generation of voxel models of textile composites from X-ray computed tomography data," *Composites Part A: Applied Science and Manufacturing*, vol. 69, pp. 150–158, 2015. [Online]. Available: <https://doi.org/10.1016/j.compositesa.2014.11.016>.
- [93] M. Weigert and U. Schmidt, "Nuclei instance segmentation and classification in histopathology images with stardist," in *The IEEE International Symposium on Biomedical Imaging Challenges (ISBIC)*, 2022.
- [94] L. Mou, Y. Zhao, H. Fu, Y. Liu, J. Cheng, Y. Zheng, P. Su, J. Yang, L. Chen, A. F. Frangi, M. Akiba, and J. Liu, "Cs2-net: Deep learning segmentation of curvilinear

- structures in medical imaging,” *Medical Image Analysis*, vol. 67, p. 101874, 2021. [Online]. Available: <https://doi.org/10.1016/j.media.2020.101874>
- [95] Y. Peng, L. Pan, P. Luan, H. Tu, and X. Li, “Curvilinear object segmentation in medical images based on odos filter and deep learning network,” *Applied Intelligence*, vol. 53, p. 23470–23481, 2023. [Online]. Available: <https://doi.org/10.48550/arXiv.2301.07475>
- [96] S. Upadhyay, A. G. Smith, D. Vandepitte, S. V. Lomov, Y. Swolfs, and M. Mehdikhani, “Deep-learning versus greyscale segmentation of voids in x-ray computed tomography images of filament-wound composites,” *Composites Part A: Applied Science and Manufacturing*, vol. 177, p. 107937, 2024. [Online]. Available: <https://doi.org/10.1016/j.compositesa.2023.107937>
- [97] S. M. Emtiaz, M. Pitto, P. Šimáček, and S. G. Advani, “Role of fiber clustering and resin bleeding on voids and evolution of fiber volume fraction for additively manufactured continuous carbon fiber thermoset composites with dual-cure resins,” *Composites Part A: Applied Science and Manufacturing*, vol. 189, p. 108601, 2025. [Online]. Available: <https://www.sciencedirect.com/science/article/pii/S1359835X24005992>
- [98] R. Guo, J. Stubbe, Y. Zhang, C. M. Schlepütz, C. R. Gomez, M. Mehdikhani, C. Breite, Y. Swolfs, and P. Villanueva-Perez, “Deep-learning image enhancement and fibre segmentation from time-resolved computed tomography of fibre-reinforced composites,” *Composites Science and Technology*, vol. 244, 2023. [Online]. Available: <https://doi.org/10.1016/j.compscitech.2023.110278>
- [99] R. Karamov, C. Breite, S. V. Lomov, I. Sergeichev, and Y. Swolfs, “Super-resolution processing of synchrotron ct images for automated fibre break analysis of unidirectional composites,” *Polymers*, vol. 15, no. 9, p. 2206, 2023. [Online]. Available: <https://doi.org/10.3390/polym15092206>
- [100] L. Zweifel, J. Kupski, C. Dransfeld, B. Caglar, S. Baz, D. Cessario, G. T. Gresser, and C. Brauner, “Multiscale characterisation of staple carbon fibre-reinforced polymers,” *J. Compos. Sci.*, vol. 7, no. 11, p. 465, 2023. [Online]. Available: <https://doi.org/10.3390/jcs7110465>
- [101] N. Katuin, “Process Optimization of Ultrasonic Tacking of Unidirectional Tapes,” *TU Delft MSc thesis repository*, 2020.
- [102] O. Yuksel, B. Caglar, G. Broggi, V. Michaud, R. Akkerman, and I. Baran, “Saturated transverse permeability of unidirectional rovings for pultrusion: The effect of microstructural evolution through compaction,” *Polymer Composites*, vol. 45, no. 7, pp. 5935–5952, 2024. [Online]. Available: <https://doi.org/10.1002/pc.28171>
- [103] T. Zheng, F. Jia, Z. Wang, Z. Chen, F. Guo, and L. Guo, “Statistical characteristics of realistic fiber misalignments of unidirectional composites: Fitting distributions and scanning length effects,” *Thin-Walled Structures*, vol. 206, p. 112621, 2025. [Online]. Available: <https://doi.org/10.1016/j.tws.2024.112621>

- [104] I. Cleasby, E. Wakefield, B. Morrissey *et al.*, “Using time-series similarity measures to compare animal movement trajectories in ecology,” *Behavioral Ecology and Sociobiology*, vol. 73, p. 151, 2019. [Online]. Available: <https://doi.org/10.1007/s00265-019-2761-1>
- [105] C. Houriet, V. Damodaran, C. Mascolo, S. Gantenbein, D. Peeters, and K. Masania, “3d printing of flow-inspired anisotropic patterns with liquid crystalline polymers,” *Advanced Materials*, vol. 36, p. 2307444, 2024. [Online]. Available: <https://doi.org/10.1002/adma.202307444>
- [106] A. C. Jones, C. H. Arns, A. P. Sheppard, D. W. Hutmacher, B. K. Milthorpe, and M. A. Knackstedt, “Assessment of bone ingrowth into porous biomaterials using micro-ct,” *Biomaterials*, vol. 28, pp. 2491–2504, 2007. [Online]. Available: <https://doi.org/10.1016/j.biomaterials.2007.01.046>
- [107] L. Holzer, P. Marmet, M. Fingerle, A. Wiegmann, M. Neumann, and V. Schmidt, *Tortuosity and Microstructure Effects in Porous Media: Classical Theories, Empirical Data and Modern Methods*, ser. Springer Series in Materials Science. Springer, 2023, vol. 333. [Online]. Available: <https://doi.org/10.1007/978-3-031-30477-4>
- [108] M. F. Lagadec, R. Zahn, S. Müller, and V. Wood, “Topological and network analysis of lithium ion battery components: the importance of pore space connectivity for cell operation,” *Energy Environmental Science*, vol. 11, pp. 3194–3200, 2018. [Online]. Available: <https://doi.org/10.1039/C8EE00875B>
- [109] H. Alatrash and F. Velledits, “Comparing petrophysical properties and pore network characteristics of carbonate reservoir rocks using micro x-ray tomography imaging and microfacies analyses,” *International Journal of Geomath*, vol. 15, no. 1, 2024. [Online]. Available: <https://doi.org/10.1007/s13137-023-00243-8>
- [110] V. Lisitsa, Y. Bazaikin, and T. Khachkova, “Computational topology-based characterization of pore space changes due to chemical dissolution of rocks,” *Applied Mathematical Modelling*, vol. 88, pp. 21–37, 2020.
- [111] X. Li and S. McMains, “A voronoi diagram approach for detecting defects in 3d printed fiber-reinforced polymers from microscope images,” *Computational Visual Media*, vol. 9, pp. 41–56, 2023. [Online]. Available: <https://doi.org/10.1007/s41095-021-0265-1>
- [112] R. Abbott, A. Nishimwe, H. Wiputra *et al.*, “A super-resolution algorithm to fuse orthogonal ct volumes using orthofusion,” *Scientific Reports*, vol. 15, p. 1382, 2025. [Online]. Available: <https://doi.org/10.1038/s41598-025-85516-y>
- [113] A. Awenlimobor, N. Sayah, and D. E. Smith, “Micro-void nucleation at fiber-tips within the microstructure of additively manufactured polymer composites bead,” *Composites Part A: Applied Science and Manufacturing*, vol. 190, p. 108629, 2025. [Online]. Available: <https://doi.org/10.1016/j.compositesa.2024.108629>
- [114] R. Guo, M. Alves, M. Mehdikhani, C. Breite, and Y. Swolfs, “Synthesising realistic 2d microstructures of unidirectional fibre-reinforced composites with a generative



- adversarial network,” *Composites Science and Technology*, vol. 250, 2024. [Online]. Available: <https://doi.org/10.1016/j.compscitech.2024.110539>
- [115] S. Fliegner, M. Luke, and P. Gumbsch, “3d microstructure modeling of long fiber reinforced thermoplastics,” *Composites Science and Technology*, vol. 104, pp. 136–145, 2014. [Online]. Available: <https://doi.org/10.1016/j.compscitech.2014.09.009>
- [116] H. Tang, H. Chen, Q. Sun, Z. Chen, and W. Yan, “Experimental and computational analysis of structure-property relationship in carbon fiber reinforced polymer composites fabricated by selective laser sintering,” *Composites Part B: Engineering*, vol. 204, p. 108499, 2021. [Online]. Available: <https://doi.org/10.1016/j.compositesb.2020.108499>
- [117] B. A. Lawson, C. Drovandi, P. Burrage, A. Bueno-Orovio, R. W. dos Santos, B. Rodriguez, K. Mengersen, and K. Burrage, “Perlin noise generation of physiologically realistic cardiac fibrosis,” *Medical Image Analysis*, vol. 98, p. 103240, 2024. [Online]. Available: <https://doi.org/10.1016/j.media.2024.103240>
- [118] P. Seibert, A. Raßloff, K. Kalina, M. Ambati, and M. Kästner, “Microstructure characterization and reconstruction in python: Mcrpy,” *Integrating Materials and Manufacturing Innovation*, vol. 11, pp. 450–466, 2022. [Online]. Available: <https://doi.org/10.1007/s40192-022-00273-4>
- [119] P. Seibert, A. Raßloff, K. Kalina, A. Safi, P. Reck, D. Peterseim, B. Klusemann, and M. Kästner, “On the relevance of descriptor fidelity in microstructure reconstruction,” *PAMM*, vol. 23, 2023, first published: 15 September 2023. [Online]. Available: <https://doi.org/10.1002/pamm.202300116>
- [120] P. Seibert, A. Raßloff, K. A. Kalina, J. Gussone, K. Bugelnig, M. Diehl, and M. Kästner, “Two-stage 2d-to-3d reconstruction of realistic microstructures: Implementation and numerical validation by effective properties,” *Computer Methods in Applied Mechanics and Engineering*, vol. 412, p. 116098, 2023. [Online]. Available: <https://doi.org/10.1016/j.cma.2023.116098>
- [121] P. Seibert, A. Raßloff, K. Kalina, and M. Kästner, “Fast descriptor-based 2d and 3d microstructure reconstruction using the portilla–simoncelli algorithm,” *Engineering with Computers*, vol. 41, p. 589–607, 2024, published: 22 July 2024. [Online]. Available: <https://doi.org/10.1007/s00366-024-02026-7>
- [122] V. Blümer, C. Soyarslan, and T. van den Boogaard, “Generative reconstruction of 3d volume elements for ti-6al-4v basketweave microstructure by optimization of cnn-based microstructural descriptors,” *arXiv preprint arXiv:2403.09609*, 2024, submitted on 14 Mar 2024. [Online]. Available: <https://doi.org/10.48550/arXiv.2403.09609>





# ACKNOWLEDGMENTS

The past PhD years have been a journey with a mix of challenges, learning, and unexpected turns. COVID arriving just as I was starting out added an extra layer of complexity to an already daring undertaking. And yet, despite the many surprises along the way, I'm grateful to have been surrounded by colleagues, mentors, and friends who I could share this time in shared support, time, and care.

My first thanks go to my supervisors.

Clemens, thank you for showing up with optimism and creativity, for thinking broadly, and for spotting connections where others might not. Daniël, thank you for your kind and steady guidance, and for always keeping the bigger picture in focus. And Bilim, last but by no means least, thank you for your sharp insights and thoughtful questions that pushed me to think more deeply.

Each of you has supported me in your own way, and together you formed a support system I could rely on. Thank you for your trust, your patience, and for being there during the tougher moments, with grace and good humour. I feel both proud and grateful to continue as your colleague after this chapter ends.

To the colleagues in and outside TU Delft with whom I've had the pleasure to collaborate, a heartfelt thank you. It's been a joy to build things together and learn from one another. To the IVW team in Kaiserslautern – Benedikt Boos, Christoph Queck, Julia Jungbluth and Martin Gurka – thank you for the many years of smooth and fruitful collaboration and insightful scientific discussions. We look forward to the continuation of this journey. To Alexios Argyropoulos and Veronique Michaud through their work at EPFL, it was a pleasure to work together. Our collaboration was not only productive, but also genuinely enjoyable, and I look back on it with warmth and appreciation. To Hans Luinge, Tjitse Slange and Guillaume Rataouit through their work at Toray, thank you for your support at different stages of the project. I hope the insights we gathered will help develop further this very interesting field of study. To Rob Langelaan at Naturalis Biodiversity Centre, a warm thanks for the care and time invested in the scans used for Chapters 2 and 3. To Ran, Amin, Onur and Baris C. on the TUDelft side, thank you for your support and joint efforts across different projects, it was a pleasure to work together.

And to the many others who contributed to the project in different ways, you're very much part of this too.

The entire Aerospace Structures and Materials department deserves recognition in this section. While I may not be able to name everyone I would like to acknowledge, here are a few important mentions.

To the PAAM group members not yet mentioned: Shailee, Maissailoun, Diwakar, Devi, Andrey, Emma, Jonas, Ishank, Mohamad, Ujala, Chizoba, Xuejiao, Antonia and more –

thank you for the sense of community and collaboration. Glad to be part of this team, and looking forward to more team-building events and potlucks!

To the many officemates who came and went, each of you left a mark. Special thanks to Ashish, Alvaro, Ehshan, Zhiyuan, Nan T., and Camila for the chats, the kindness, and the humour. Thank you for the many scientific (and non-scientific) conversations; you helped make our office a genuinely lovely place to be.

To the more senior colleagues not yet mentioned who stepped in as informal mentors, thank you. In particular to John-Alan, Roger, Baris K., Arjen, Nan Y., Rinze, Roeland, Andrei, Sergio, Calvin, Irene, Julie, Santiago, and Sybrand and many more, your encouragement and advice helped more than you probably realise. A warm mention must also go to our DASML and SAMXL colleagues, with a particular mention to Chantal, Alexander, Bas, Sharon, Victor, Dave, Berthil, and Abhas; thank you for the insightful conversations and help. A thanks also goes to our ICT staff, always ready to help, and in particular to Denise for her kind presence. To our brilliant secretaries Shanta, Tess, Gemma and Mylene, thank you for making things run smoothly to have a nice environment in the department, and always lending a listening ear when needed.

To all my current and past day-to-day colleagues not yet mentioned, thank you for being a source of strength, laughter, and solidarity (and for the many shared cakes in the coffee corner!). In particular a mention to Mariana S. C., Davide, Huub, Rose, Giovanna, Natalia, Benjamin, Javier, Mary, Carolina, Muhamad, Deniz, Caroline, Stratos, Morteza, Sasan, Wenjie, Clement, Guillaume, Francisco, Amalia, Dimitris, Avyadish, Charline, Mirko, Jimmy, Thanos, Tinashe, JingJing, Miisa, Riccardo and the old NovAM crew Satya, Mariana L. C., Anton, Hugo, Vincent, Tadhg, Cleo, Amber, Wouter P., Wouter W., Arijana, Paul – the list could go longer - you helped make the daily work-life something to look forward to.

To Eva, a special thank you. Your steady support, belief in me, and presence through thick and thin, from the virtual coffees during lockdown to quiet check-ins and big life moments, have really meant the world. Thank you for walking this road with me and being such a great friend.

To Andreea, Niels, and Katharina, thank you for your warmth, honesty, and encouragement through the years. I'm glad we are still in touch even after you moved out of Delft, your presence has made a lasting difference.

To my chosen family here, thank you. Simone, Barbara, Davide, Enrico, Kamila (the greatest PhD thesis cover designer), Valerio and little Adam, thank you for being there in countless ways, through celebrations and tough times. Your presence has supported me in probably more ways than can be put into words.

To Chiara and Giancarlo, thank you for your lasting friendship across borders and years. I am glad we continue to share life's milestones together, even from afar.

*A mamma e papà, grazie per il vostro sostegno in questo (lungo) percorso e per aver sempre*

*creduto in me, fin da piccola. La vostra fiducia mi ha aiutata a ritrovarla in me stessa, nei momenti più difficili.*

*Grazie per avermi sempre incoraggiata a trovare la mia strada. Se oggi celebriamo questo traguardo, è anche merito vostro.*

A little piece of this PhD belongs to each and everyone of you.  
Thank you.

*Silvia  
Delft, September 2025*



# CURRICULUM VITÆ

## **Silvia GOMARASCA**

Silvia Gomasasca was born in Italy, and obtained her BSc degree in Aerospace Engineering at the University of Padua (Padua, Italy) in 2015. She then moved to the Netherlands for her MSc studies at the Aerospace Engineering faculty of Delft University of Technology which she completed in 2018 with the Novel Aerospace Materials group, working on the study of local polymer dynamics via laser speckle imaging.

After a period of research work at Deakin University (Geelong, Australia), in 2020 she joined as a PhD candidate the Aerospace Manufacturing Technology group at Delft University of Technology. The focus of her project was on the three-dimensional microstructural characterisation of unidirectional composites at a single-fibre level via X-Ray Computed Tomography.



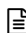
# LIST OF PUBLICATIONS

## JOURNAL ARTICLES

1. **S. Gomasasca**, D. M. J. Peeters, B. Atli-Veltin, C. A. Dransfeld, 'Characterising Microstructural Organisation in Unidirectional Composites', *Composites Science and Technology* (2021)
2. **S. Gomasasca**, D. M. J. Peeters, B. Atli-Veltin, T. Slange, G. Rataouit, C. A. Dransfeld, 'Characterising pore networks and their interrelation with the fibre architecture in unidirectional composites', *Composites Part A* (2024)

## CONFERENCE PROCEEDINGS

1. **S. Gomasasca**, D. M. J. Peeters, B. Atli-Veltin, C. A. Dransfeld, H. Luinge, 'The role of matrix boundary in the microstructure of unidirectional composites', *Proceedings of the 20th European Conference on Composite Materials: Composites Meet Sustainability* (2022)
2. A. Argyropoulos, B. Caglar, **S. Gomasasca**, T. Ricard, V. Michaud, 'Development and characterization of hybrid thin-ply composite materials', *Proceedings of the 20th European Conference on Composite Materials* (2022)
3. O. Yuksel, R. Hartley, G. Broggi, V. Maes, **S. Gomasasca**, T. Baumard, A.L. Reun, C. Dransfeld, B. Caglar, 'Microstructural Analysis Of Unidirectional Composites: A Comparison Of Data Reduction Schemes', *Proceedings of the 21st European Conference on Composite Materials* (2024)
4. **S. Gomasasca**, A. S. Hossein, R., Tao, B., Boos, C., Queck, D., Peeters, B., Atli-veltin, M., Gurka, C., Dransfeld, 'Assessment of the variability of unidirectional prepregs at multiple scales', *14th Conference on Industrial Computed Tomography (iCT)* (2025)

 Included in this thesis.





# Propositions

accompanying the dissertation


## DECONVOLUTING MICROSTRUCTURAL FEATURES IN UNIDIRECTIONAL COMPOSITES

by

**Silvia GOMARASCA**

-  1. Accurate segmentation of relevant features of interest is still a fundamental bottleneck in image analysis.
-  2. A multi-scale approach to manufacturing unidirectional prepreg tapes will only be adopted by industry if research proves it to be cost-effective.
-  3. X-ray computed tomography will never replace optical microscopy in material characterisation.
-  4. Methods for analysing temporally correlated complex systems in nature can offer valuable insights into studying synthetically designed spatially correlated structures.
- 5. A team with diverse views can easily simplify complex problems as much as complexify simple solutions.
- 6. Diversity and inclusion actions should not focus on labels, but rather on addressing individual needs while fostering common ground.
- 7. A University can claim collaboration as a core value when collaborative work becomes a requirement of its PhD trajectories.
- 8. PhD candidates must be trained so that society can rely on their judgment, not only on their academic performance.
- 9. An independent researcher is not necessarily a successful researcher, and vice versa.
- 10. Recognising similarities between different fields creates the greatest potential for innovation.

These propositions are regarded as opposable and defendable, and have been approved as such by the promotor prof. C. A. Dransfeld, dr. D. Peeters and dr. B. Atli-Veltin.

 Pertains to this dissertation.



